A STUDY OF LIQUID DISPERSIONS IN A SPRAY DRYING TOWER

by

CHRISTOPHER JOHN ASHTON

A Thesis submitted to
The University of Aston in Birmingham
for the Degree of
Doctor of Philosophy

Department of Chemical Engineering
University of Aston in Birmingham

March 1980

CONTENTS

ACKNOWLEDGEMENTS

The author is indebted to and wishes to record his gratitude to the following people.

Professor G.V. Jeffreys for his valued guidance and personal interest throughout this work.

Dr. C.J. Mumford for his helpful advice.

Mrs A. Mellings for her expertise in the photographic department.

Summary

Studies of Liquid Dispersion in a Spray Drying Tower

CHRISTOPHER JOHN ASHTON Ph.D. 1979

A study has been undertaken of drop formation from swirl nozzles as encountered in spray drying operations.

Four swirl nozzles of different sizes and geometry have been studied experimentally and theoretically in order to characterise the nozzle and establish a model that could predict drop size as a function of throughput, pressure drop and the physical properties of the slurry.

The mechanism of drop formation was observed using high speed cine and flash photography. The drop size was estimated from photographs using a Zeiss particle size analyser and the results were confirmed by a Knollenburg particle size analyser.

A mathematical model has been developed which is an extension of Taylor's model for conical swirl chambers but which is more generally applicable irrespective of the geometry and the agreement between the experimental discharge velocities and drop sizes, and those predicted were very good.

Key Words

Swirl nozzles
Sheet Breakup
Drop formation
Atomisation

INTRODUCTION

Spray drying has applications in many industries, from the delicate processing conditions in food and pharamaceutical manufacture to the high tonnage outputs within such heavy chemical industries as mineral ores and clays. Spray drying is the transformation of a pumpable fluid feed, either a solution, slurry or paste into a particulate dried product in a single drying process. The feed is atomised and contacted with hot air and rapid evaporation occurs due to the extensive surface area provided by the spray. A dry product is formed which is then recovered from the drying medium.

Atomisation is most commonly achieved by either rotary or pressure nozzle atomisers, the selection of which for any given operation being dependent on the particle size distribution in the final product. Typical values of the mean size of the dried product varies between 70-110 microns for rotary atomisers and 180-250 microns for pressure nozzles. The quality and nature of the final product is dependent on the wet droplet size, since this parameter controls the heat and mass transfer rates during evaporation. A knowledge of the droplet sizes produced by an atomiser is therefore important but in spite of much published data by many workers, the mechanism of atomisation is

still a controversial subject. Much work has been reported on the atomisation characteristics of Newtonian fluids but these are seldom encountered, particularly in the food industry. This work was initiated to study the atomisation of slurries and several chalk slurry formulations were selected. The main object of this work was to provide further insight into the mechanism by which the sheet of slurry emitted from a swirl spray pressure nozzle disintegrates into droplets, and also to compare this with water.

Chapter 1

Spray Drying Fundamentals

1.1 Methods of atomising liquids

1.2 Spray-air contact

1.3 Drying of droplets

1.1 Methods of Atomising Liquids

The performance of a spray dryer is critically dependent upon the drop size distribution of the spray, since heat and mass transfer rates and drying times are dependent on the droplet size. Thus the ideal requirement for an atomiser is to produce homogenous sprays. Such sprays have not yet been obtained at industrial feed rates, although certain types of atomiser are capable of producing this type of spray when operating with liquids of specific characteristics at low feed rates.

Most of the atomisers commonly employed in chemical engineering were designed for simple low viscosity Newtonian liquids. However when handling slurries or pastes of anamolous properties there is a great deterioration in performance with consequent affect on product quality. Thus selection of the optimum atomiser depends on the specific functions required for a given application.

Whilst there is a multitude of individual atomisers, most fall within a few basic types summarised in Table (1.1), and are classified according to the source of energy employed.

The most effective way of utilising energy imparted to a liquid is to arrange that the liquid mass has a large specific surface before it breaks down into drops. Thus the primary function of an atomiser is to transpose bulk liquid into thin liquid sheets.

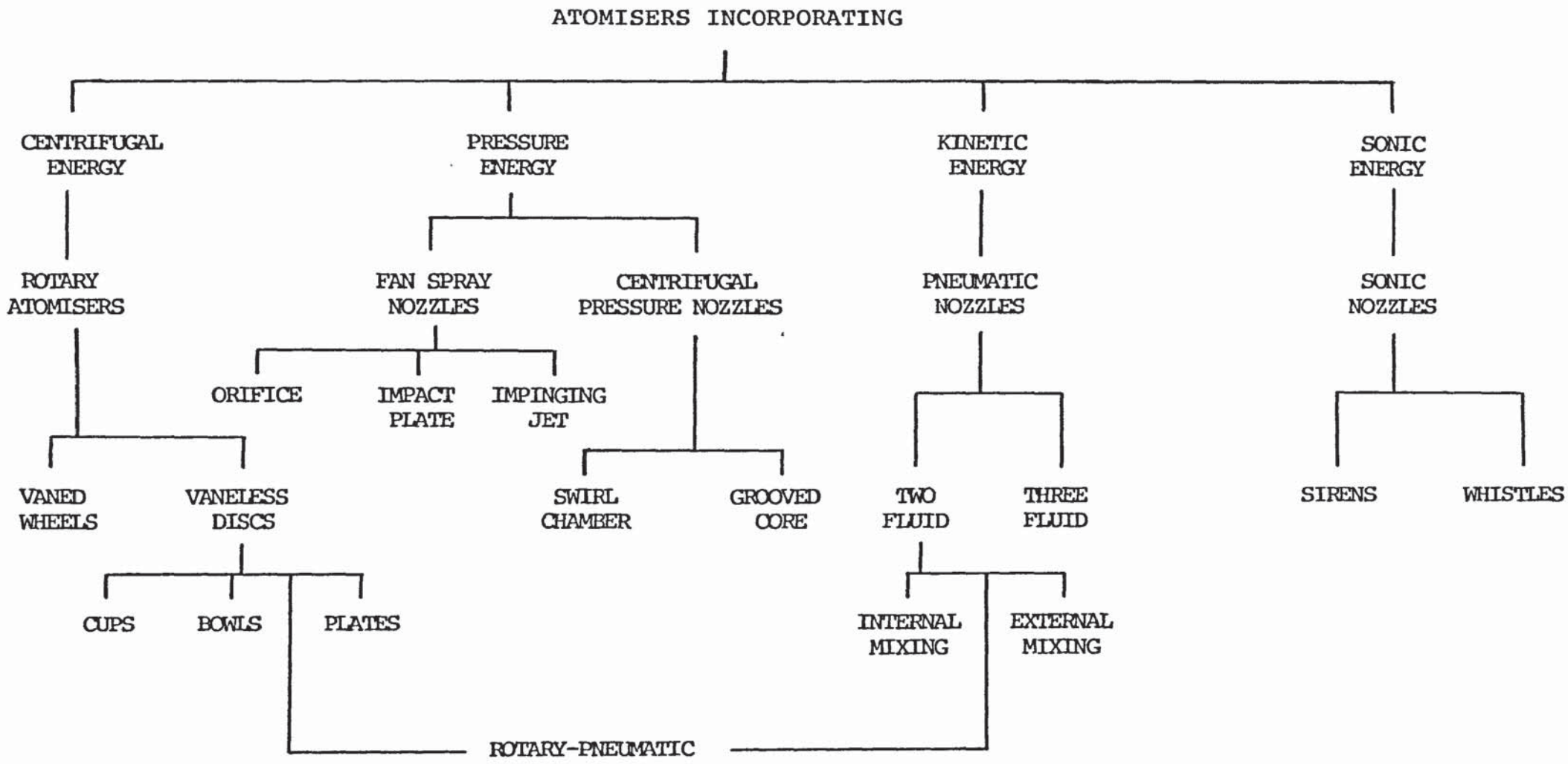

TABLE 1.1. CLASSIFICATION OF ATOMISERS

Rotary Atomisation

In rotary atomisation the feed liquid is centrifugally accelerated to high velocity before being discharged. Of the several types of rotary atomiser, the spinning disc is probably most widely used, and is capable of handling thick slurries or suspensions at high feed rates.

Liquid fed under gravity or low pressure to the centre of the disc is accelerated towards the edge across a smooth surface or through vanes or slots. At high peripheral speeds liquid is discharged as individual droplets, or as ligaments or a film that subsequently disintegrates into droplets depending upon operating conditions, liquid properties, and atomiser design.

Smooth flat vaneless discs are rarely used in spray drying operations due to the severe slippage which occurs between the feed liquid and the disc at high speeds. Slippage is prevented by confining the liquid to the surface of a vane thus attaining the maximum possible release velocity. Slippage is alternatively reduced by feeding liquid onto the lower surface of a disc shaped as an inverted plate bowl or cup. The liquid film is held against the disc surface by centrifugal action. Both techniques are used to handle large feed rates although the vaned designs (atomiser wheel) produce finer sprays. Another advantage of the rotary

atomiser is the flexible operation because feed rate and disc speed are independent. Masters (1) has reviewed the effects of these variables upon the type of atomisation and effect upon drop size.

Pneumatic Nozzle Atomisation

Pneumatic nozzle atomisation involves impacting liquid bulk with high velocity gas. The mechanism of atomisation is one of high velocity gas creating high frictional forces over liquid surfaces causing liquid disintegration into spray droplets. These conditions are generated by either expansion of the air to very high velocities or by directing the air flow on unstable thin liquid sheets formed by rotating the liquid in the nozzle. Liquid break-up is effective in that sprays of low mean drop size can be formed.

For low feed rates, rotation of the liquid within the nozzle is not required. However when the required feed rate is high the liquid must be pre-filmed. Various design techniques are available to produce optimum conditions for contacting air and liquid. In all cases the liquid is pre-filmed in the feed nozzle orifice. The various designs are

1) Internal mixing - air/liquid contact within nozzle head.

2) External mixing - air/liquid contact outside the nozzle head.

3) Three-Fluid nozzle - combined internal and external mixing by using two air flows within the nozzle head.

4) Pneumatic Cup atomiser - air/liquid contact at the rim of a rotating nozzle head.

Internal mixing designs achieve high energy transfer although the independent control of both liquid and air streams offered by external mixing types afford greater control of atomisation.

The combined mixing nozzle is used with high viscosity liquids where the advantages of being able to handle difficult liquids offset the low nozzle efficiencies.

The pneumatic cup atomiser is used for high viscosity liquids or to obtain very fine sprays from low viscous liquids. The pre-filming of liquid at the rotating nozzle edge provides a uniform liquid sheet for contact with the air flow.

As with other atomisers, pneumatic atomisers produce finer droplets when the energy input per unit quantity of liquid is increased. This is achieved by increasing the air/liquid mass ratio. The effect of operating variables on pneumatic atomisation has been studied by several workers, notably Kim and Marshall (2) and Nukiyama and Tanasawa (3).

Pressure Atomisers

In a pressure atomiser, liquid is forced under pressure through an orifice and the form of the resulting liquid sheet can be controlled by varying the direction of flow towards the orifice. By this method, conical and flat spray sheets can be produced.

a) Formation of Fan Spray Sheets

In the single orifice fan spray nozzle, two streams of liquid are made to impinge behind an orifice and a sheet is formed in a plane perpendicular to the plane of the streams. Oval or rectangular orifices may be employed but the former type is more popular. Dombrowski et al. (4) have studied both drop sizes and modes of sheet disintegration from these sprays. Their findings indicate that the extent of the sheet is controlled at the boundary by the equilibrium between the momentum along the streamlines and the contraction of the edges as a result of surface tension. Depending on the orifice configuration, the spray angle can vary from a straight stream up to more than 100^{o}. Fan spray nozzles produce narrow elliptical patterns that are suitable for many coating operations. They are often used in spray guns and multiple nozzles.

The principle of operation of the impinging jet nozzle resembles that of the fan spray with the exception that two or more independent jets are caused

to impinge in the atmosphere. The principal advantage of this atomiser is the isolation of different liquids until they impinge outside the nozzles. However, high stream velocities and wide impingement angles are necessary in order to approach a spray quality obtainable from other nozzle types.

With deflector atomisers, liquid is discharged through a circular orifice and is made to strike a curved deflector plate. The spray is deflected up to 75° from the nozzle axis. Relatively coarse sprays are produced, particularly at low pressures.

b) The Formation of Conical Sheets

When liquid is caused to flow through a narrow divergent annular orifice a conical sheet of liquid is produced where the liquid is flowing in radial lines. The angle of the cone and the thickness of the sheet can be controlled by the divergence of the spreading surface and the width of the annulus. For small throughputs this method is not favourable because of difficulties in manufacturing an accurate annulus. Conical sheets, however, are normally produced by swirl spray pressure nozzles. This type of nozzle may be used to produce:

(i) Hollow cone sprays - in which the spray drops are concentrated in the periphery of the cone, leaving the centre of the cone virtually free of spray, particularly near the nozzle orifice. In low throughput

nozzles of capacities less than 50 litres per hour, the hollow characteristic rapidly merges to the full cone state as the drops are extracted by air induced into the spray cone.

(ii) Full cone sprays - in which the whole volume of the spray cone is filled with an almost evenly distributed mass of spray drops. Spray (cone) angles may vary between 30^{o} and 120^{o}, the finest atomisation generally at low capacities, high pressures and wide spray angles.

The mechanics of flow through swirl spray atomisers and the droplet sizes produced will be discussed in detail in Chapter 3.

1.2 Spray-Air Contact

The manner in which sprayed droplets are contacted by the drying air bears an important relation to the evaporation rate of the spray, the optimum residence time of droplets in a hot atmosphere and the extent of wall deposit formation. The properties of the dried produce are thus influenced to a large extent. The hot air/spray contact depends upon the position of the atomiser relative to the air inlet ports, and co-current, counter-current and mixed flow arrangements have been developed and operated. Experience has shown that counter flow operation offers better performance in most spray drying processes, decreasing wall impingement of produce and enabling coarser sprays to be dried per given chamber size. Whatever the mode of atomisation, each droplet in the resulting spray is ejected at a velocity greatly in excess of the air velocities within the chamber. However, direct penetration is limited to short distances from the atomiser, due to friction drag. The droplets become influenced by the surrounding air flow and movement is governed by the design of air dispersed. Any attempt to calculate chamber dimensions is dependent on droplet path data and rate of drying.

Droplet travel from the time of injection to the point of contact with the chamber wall has been studied by various workers. From nozzle atomisers in non-rotary air flow the motion has been considered in either one or two dimensions, and from rotary atomisers where the air

flow is rotating, three dimensional motion is considered. In a theoretical study of droplet motion certain simplifying assumptions are usually made. These include:

a) heat transfer between droplet and air is by forced convection.

b) the spray consists of homogenous, spherical droplets.

c) the chance of droplet break-up or coalescence is disregarded.

d) rotating air flow is considered as a forced vortex.

The work of Lapple and Shepherd (5) who solved the dynamic equations for spherical particles undergoing no mass transfer in a uniform flow field is often cited. Indeed Masters (6) in a study of rotating disc atomisation applied these equations and the equations of heat and mass transfer of Ranz and Marshall (18) to indicate the three dimensional motion of a drop with regard to wall impingement. However no solutions were given for rotating fields because of the complexity of gas flow patterns in the spray drier, although a critical drop diameter was found which affected the extent of wall impingement. Their results agreed with those of Friedman et al. (8) who studied the characteristics of drops produced by low speed disc atomisers. A relation was proposed which assessed the variations in trajectories when altering atomisation conditions.

Bailey et al. (9) predicted the motion of petroleum

droplets undergoing evaporative mass transfer in rotating hot surroundings. However, only the two dimensional case was considered and a simple gas velocity distribution was assumed.

Droplet movement during deceleration is normally very small and the droplet path of travel can be considered to be that of the air flow pattern in the chamber. For disc atomisation in large diameter chambers local affects around the atomiser are negligible. However for small diameter chambers, Gluckert (10) has shown that air movement due to the atomiser becomes the controlling factor in the trajectory path.

Droplet residence times have been studied by Katta and Gauvin (11) who developed models to predict the three dimensional motion of drops in a pilot plant spray drier and showed that the droplet motion depended on both the atomising device and the air flow pattern within the chamber.

Chaloud et al. (12) obtained velocity profiles in a drying chamber operating with no spray and noted the presence of a core of air with a high rotational velocity rising through the centre of the tower. In a later study by Paris et al. (13) of a counter current operation with a spray, a model was developed for the air flow distribution. This however was achieved by deconvolution of residence time distribution data, using an analogue simulation. In their model the bulk flow was represented by two stirred tanks in parallel with a plug flow bypass,

which reflected the rapidly ascending central core surrounded by an annular zone of intense turbulence reported by Chaloud. In addition they also noted that when the tower was loaded, a highly turbulent region was formed around the atomiser, and a significant amount of "backflow" was observed in the central portion of the tower.

Gauvin et al. (14) identified a "nozzle" cone and a "free extrainment" zone in the spray dryers they studied, and the presence of such zones must be considered in the analysis of residence times in spray drying towers.

Ade-John and Jeffreys (15) from flow visualisation studies and residence time distributions in a counter current pilot plant spray dryer, identified the volumes of the various drying zones. The overall flow pattern was simulated through a combination of well defined flows such as completely mixed well-stirred tank reactor zones, plug flow zones and by-pass zones. They identified a thin by-pass layer around the walls of the tower present in all experimental conditions. Their smoke pulse experiments also identified three other zones; a well-mixed section at the air entry region, a well-mixed section enclosing the spray nozzle and a plug flow zone connecting them. The changes in volume of these zones with respect to air flow and tower dimensions were correlated by a dimensional analysis.

Thus from this type of work a better estimate of droplet residence time can be obtained which is important in spray dryer design. It is desirable to know the influence of entrained air on droplet motion from nozzles as relative velocity between droplets and the air is an important factor in evaluating moisture evaporation rates. Air entrainment maintains the droplet velocity at a level significantly greater than the droplet terminal velocity over time periods where the majority of evaporation takes place. Thus faster droplet trajectories to the wall are encountered with a trajectory time less than that for complete evaporation so resulting in wall deposits.

A model developed by Benatt (16) predicts the mass flows of entrained air for centrifugal pressure nozzles.

1.3 Drying of Droplets

In spray drying, the liquid forms a disperse phase in the gaseous medium and the drying process involves evaporation from the surfaces of drops. Because of the variation of drop size and distribution in a spray dryer, it is necessary to discuss evaporation with regard to single drops and then estimate the effect of mutual interaction.

Drying Mechanism in General

Evaporation of liquid from a droplet involves simultaneous heat and mass transfer. Heat is transferred by convection from the drying medium (normally air) and is converted into latent heat during evaporation. A number of theories describe this transport mechanism; those which have gained general recognition include the diffusion, capillary and evaporation-condensation theories.

Under constant evironmental conditions the drying process can be divided into a constant rate and one or two falling rate periods. The bulk of moisture within the drop is removed in the constant rate period. The drop surface is maintained at a saturated level by transport of liquid from the drop interior. The vaporised moisture is transported through a boundary layer which surrounds each droplet and it is assumed that the resistance to transport occurs across this

layer. As the moisture level within the droplet decreases, a point is reached whereby transport of liquid to the drop surface cannot maintain surface saturation and the drying rate falls. Internal moisture flow then becomes the controlling factor, diffusion and capillarity being regarded as the more significant mechanisms.

Pure Liquid Droplets

For a spherical particle moving in a fluid, it can be expected from dimensional analysis that for heat and mass transfer:

$$Nu = Nu\ (Re, Pr) \tag{1.1}$$

$$Sh = Sh\ (Re, Sc) \tag{1.2}$$

where $Re = D.V.\rho_a/\mu_a$ (Reynolds Number) (1.3)

$$Pr = \frac{Cp.\mu_a}{k} \quad \text{(Prandtl Number)} \tag{1.4}$$

$$Sc = \mu_a/\rho_a D_v \quad \text{(Schmidt Number)} \tag{1.5}$$

$$Nu = hc.D/k \quad \text{(Nusselt Number)} \tag{1.6}$$

$$Sh = Kg.D/D_v \quad \text{(Sherwood Number)} \tag{1.7}$$

Much work has been done to determine the form of these equations. Frossling (17), one of the earliest investigators, derived an expression for the evaporation from drops by considering the solution to the simultaneous equations of continuity and heat and mass balances across the boundary layer. His solution was of the form:

$$Nu = 2.0 + \psi\ Re^{0.5}\ Pr^{0.33} \tag{1.8}$$

$$Sh = 2.0 + \psi\ Re^{0.5}\ Sc^{0.33} \qquad (1.9)$$

For zero relative velocity between the droplet and drying medium, Re = 0 and

$$Nu = Sh = 2.0 \qquad (1.10)$$

Various values have been found experimentally for the constant ψ, but the most widely quoted value is that found by Ranz and Marshall (18) where $\psi = 0.6$.

The above equations are limiting in that any heat transfer to the evaporated moisture is neglected and that the droplet internal structure is assumed stable. Also any distortion of the droplet from its assumed spherical shape will undoubtedly influence heat and mass transfer rates and is not accounted for. Since the boundary layer around the droplet controls the evaporation rate, any reduction in its thickness will tend to increase the evaporation rate. Considerable evaporation has been found to occur during droplet deceleration (19).

Sprays of Pure Liquid Drops

The evaporation characteristics of drops within a spray differ from those of single drops. Although basic theory applies in both cases, any analysis of spray evaporation depends upon defining the spray in terms of a representative mean diameter and size distribution, the relative velocity between droplet and drying air, droplet trajectory, and the droplet population density at any given time.

Dickinson and Marshall (20) made a computational study of the evaporation rates of sprays of pure liquid droplets. The conditions of both negligible and significant relative velocities were considered. Although certain simplifications such as constant drop temperature and ideal counter-current air flow were made, several significant phenomena were observed. A reduction in air temperature occurs as the spray evaporates with a consequent reduction in evaporation rate. Sprays with a wide drop size distribution evaporate initially more rapidly due to the small drops which evaporate at higher rates. However the overall rate is reduced since large droplets evaporate more slowly. Consequently the drop size distribution will change with time, an initial increase in the mean diameter preceeding an overall decrease until completion of evaporation. At high spray velocities the droplets were found to travel greater distances to achieve the same degree of evaporation. The influence of relative velocity on evaporation rates was found to be more significant at higher initial velocities and higher drying temperatures. At higher initial velocities the relative error in neglecting droplet velocity was greatest for the smaller drop sizes in the spray distribution. Small drops evaporated virtually instantaneously and a large proportion of the overall evaporation was accomplished in the period of droplet deceleration.

Bose and Pei (19) studied the evaporation of pure water droplets in a co-current nozzle drier. They confirmed the importance of the relative velocity in determination of evaporation rates, and the large errors which occurred by equating relative velocities to terminal velocities in the evaporation analysis. Pham and Keey (21) investigated the transition period or jet zone of the spray as it emerges from the nozzle. Temperature, velocity and concentration profiles were simplified to enable prediction of evaporation within this zone. They conclude that severe errors would occur if the jet dynamics were not taken into consideration.

Drops Containing Solids

In the presence of dissolved solids the vapour pressure of the solvent is lowered and the surface temperature of the drop rises above the wet bulb temperature. Initially a free liquid interface exists between the gas stream and the solution being dried, and evaporation proceeds as for a pure solvent. When the solution is concentrated beyond saturation, a crust forms to separate the gas and liquid interface, and a particle with a core of saturated solution results. Once the crust has formed, the heat and mass transport paths are different and the Colburn analogy no longer applies. This is confirmed by the ruptures and cracks present in many spray dried particles. Here the rate

of drying is probably so great that jets of steam issue from the pores prior to fragmentation of the particles. If the crust does not fracture, the water vapour formed will pass through the pores in the crust by diffusion and then by convection back into the gas stream.

It is therefore unlikely that correlations of the rate of mass transfer during the drying of drops based on the existence of a continuous liquid-gas interface would apply to the drying of drops of slurries.

Charlesworth and Marshall (22) studied the drying of single stationary drops containing dissolved solids and illustrated shape and composition changes that spray dried droplets can undergo. Different phenomena were observed depending whether the drying air temperature was above or below the boiling point of the droplets.

Ranz and Marshall initiated the study of crust formation and their work was later extended by Duffie and Marshall (23). Their models were based on transient mass and heat balances, and mass transfer by molecular diffusion.

Audu and Jeffreys (24) studied the drying of droplets of particulate slurries by observing single drops which were suspended and rotated in a wind tunnel, thus simulating more closely the conditions in the vicinity of a drop in a spray dryer, and forming crusts of uniform thickness. A value for ψ for pure water drops was obtained which differed from that by Ranz and

Marshall (18) and was found to vary with air temperature. This parameter itself was varied over a much wider range than that by previous workers. A further correlation was proposed for mass transfer, the coefficient ψ being temperature dependent:

$$Sh = 2.0 + 0.44 \left(\frac{Ta-Tp}{293}\right)^{0.008} . Re^{0.5} Sc^{0.33} \qquad (1.11)$$

For drops of slurries, the overall mass transfer coefficient was found to decrease with increase in drop size and drying temperature. For small drops the crust coefficient of mass transfer was found to control the drying process, expressed by:

$$kc = \frac{D_v . P_o^{1.5}}{C_T} \qquad (1.12)$$

where P_o = porosity

C_T = crust thickness

Thus from equations 1.11 and 1.12 estimates for the overall mass transfer coefficient can be obtained for use in the design of spray drying equipment.

Sprays of Drops Containing Solids

Theoretical considerations of heat and mass transfer in single drops will apply to sprays. However, the extent of vapour pressure lowering will depend on droplet size and thus the onset of crust formation will not appear simultaneously throughout the spray distribution.

Dlouhy and Gauvin (25) studied the evaporation of sprays containing dissolved solids and employed a step-wise method in calculating the total spray evaporation time. Baltas and Gauvin (26) employed a computational study but considered only a simple system of spray movement at terminal velocity in the free fall zone of a single nozzle dryer. They indicated that the difficulties in accurate prediction of spray evaporation to be due to the lack of representative data regarding air flow, temperature gradients and chamber shape. Duffie and Marshall (23) studied the effect of air temperature, feed concentration and feed temperature on the bulk density of spray dried coffee extract, but they present data which is inconclusive. Crosby and Marshall (27) attempted to relate wet drop sizes to the final dried particle size but found their results dependent on the type of material being spray dried. The dried particle properties could be varied within a limited range by control of operating parameters. The dried particle size however, was found to rarely exceed that of the wet spray.

Chapter 2

Mechanism of Atomisation

2.1 Liquid Sheet Disintegration

2.2 Liquid Jet Disintegration

2.1 Liquid Sheet Disintegration

The fundamental principle of the disintegration of a liquid consists in increasing its surface area until it becomes unstable and disintegrates. Dombrowski and Fraser (28) established three modes of disintegration for spray sheets, and classified them as "rim", "wave" and "perforated sheet". Because of surface tension, the free edge of any sheet contracts into a thick rim and "rim" disintegration occurs as it breaks up by instabilities analogous to those of free jets. In the case of a fan spray sheet, liquid threads are pulled out from the rim during contraction which rapidly disintegrate into a stream of drops. For a spinning disc or cup, the free edge of liquid formed at the rim can be controlled by the liquid flow rate together with rotational speed. At very low flowrates discrete drops are formed producing a near mono-disperse spray, whilst at higher flowrates long jets are formed which break down into a string of drops of much smaller size. With further increase of flowrate a sheet is formed which extends from the edge until a position of equilibrium is achieved. Threads are formed irregularly resulting in a wide spectrum of drop sizes.

In "perforated sheet" disintegration, small holes appear in the sheet as it advances into the atmosphere. They rapidly grow in size until the thickening rims of adjacent holes coalesce to form threads of varying diameter which break down into drops.

Disintegration also occurs through the superimposition of a wave motion on the sheet. Sheets of liquid corresponding to half or full wavelengths are torn off and tend to draw up under the action of surface tension but may suffer disintegration by air action or liquid turbulence before a regular network of threads can be formed.

Wave disturbances are the most likely cause of break-up and Fraser et al. (29) found that random centres of disturbance travelling from the orifice eventually break the sheet. A sheet of liquid moving through a gaseous atmosphere is subject to sinuous and dilational wave instabilities. Sinuous waves were found to predominate (30) for the laminar sheet produced from a fan spray nozzle at air densities below 2 kg/m^3. Above 6 kg/m^3 the sheet extent rapidly diminishes and dilational waves predominate. At low ambient densities the waves disappear and the mode of disintegration is dependent on nozzle design. Where re-circulation is allowed to exist, drops impinge on the sheet and cause "perforated sheet" disintegration. Where drops are drawn out of the spray zone "rim" disintegration propegates.

For turbulent flow at high velocities wave disintegration predominates. However at low velocities local depressions in the surface perforate the sheet

at thin regions before aerodynamic waves have grown to a sufficient amplitude. In vacuum, turbulent sheets always disintegrate through perforations.

Colbourn and Heath (31) have shown that conical sheets from swirl spray nozzles in vacuum also disintegrate by tears and perforations. Taylor (32) suggested that this mode of disintegration is caused by flow disturbances produced by waves in the air core.

Clark and Dombrowski (33) studied the effect of the surrounding gas temperature on flat sheets of water. Below 300°C sinuous waves disintegrate the sheet whilst above this temperature high frequency dilational waves and localised disturbances are superimposed on the sheet, and disintegration occurs by both waves and perforations, the contribution of the latter predominating with increasing temperature. This type of disintegration mechanism is claimed to be due to charged particles present in the gas. Measured drop sizes were found to depend upon the nature of the disintegrating process.

The analytical procedure for determining the conditions for aerodynamic wave instability is to analyse the amplitude growth rate of a small periodic disturbance given by

$$q/q_o = e^{\beta t} \qquad (2.1)$$

where q is the amplitude of the disturbance

q_o is the initial amplitude of disturbance

β is the growth rate

t is time

When β is real and positive then the disturbance will grow. If β is not real, the sheet is stable.

Weber (34) has shown that for liquid jets, q^*/q_o has a constant value of e^{12}, (where q^* is the amplitude at break-up). Fraser et al. (35) have found it has a similar value for sheets of water. Briffa and Dombrowski (36) showed the value to vary with surface tension. Squire (37) analysed sinuous waves by considering a two dimensional inviscid sheet of finite thickness. He applied the classical methods set out by Lamb (38) and obtained the wavelength of the disintegrating disturbance by differentiating the growth rate equation to yield

$$\lambda opt = 4\pi\sigma/\rho_a Vs^2 \qquad (2.2)$$

for the condition $\eta h < 0.25$ and when $We > 1$.

A similar study was presented by Hagerty and Shea (39) who explained the appearance of sinuous waves on the grounds that under normal operating conditions the wavelength is relatively large compared with the sheet thickness and that their growth rates are consequently greater than those of the alternative dilated forms. Dombrowski and Hooper (30) applied the solution obtained for a parallel sided sheet to the practical case of an attenuating sheet. The effect of ambient air density was the subject of their investigation. A similar expression to Squire for λopt was obtained, differing

only in the magnitude of the constant. Results for the higher ambient densities would only correlate if dilational waves were assumed to predominate.

Wave instability on alternating viscous sheets has been analysed by Dombrowski and Johns (40). In contrast to earlier work the wave growth rate was found to be dependent on both the wave number and sheet thickness. An expression was derived which related drop size to the liquid properties and wave growth rate, but results only compared favourably after the introduction of a further correlation coefficient.

Dombrowski proposed a model for liquid sheet disintegration, whereby waves grow on the surface of the sheet until at a critical amplitude the most rapidly growing wave is detached in the form of a ribbon half a wavelength wide. This rapidly contracts into an unstable ligament which subsequently breaks down into drops. The latter mechanism is considered analogous to the disintegration of liquid jets. The droplet itself may disintegrate further on contact with the ambient gas medium. Gordon (41) studied the disintegration of a drop falling through a high velocity gas and from a mathematical model predicted a critical drop diameter below which size all drops were stable at that velocity.

$$D_{cr} = 16\sigma/\rho_a V^2 \qquad (2.3)$$

Gordon's model also gives the disintegration time for the drop.

Several workers have studied wave growth on flat sheets of inviscid liquids surrounded by an inviscid atmosphere, as exemplified by the work of Squire and Hagerty and Shea who used linearised equations. Clark and Dombrowski (42) extended the analysis to second order terms by a method of successive approximation, although this work was again based on parallel sided flat sheets. All the above authors produce dispersion relations and solve them on the assumption that waves grow with time, although this, in fact, has not been confirmed experimentally. Crapper et al. (43), in a photographic study on Kelvin-Helmholtz or aerodynamic waves on thin liquid sheets, found wave growth to be dependent on sheet velocity and distance from the orifice. Crapper, Dombrowski and Pyott (44) tried to achieve better predictions for wave growth by applying a large amplitude theory based on the formation of vortices in each wave trough, and on the assumption of a parallel sided flat sheet.

Crapper, Dombrowski and Jepson (45) used a linearised analysis to investigate wave growth on flat sheets of Newtonian and non-Newtonian liquids by the inclusion of a complex viscosity term. Gas viscosity was also taken into account and considered to be an important parameter. For the conditions where the wavelength is large compared with sheet thickness it has been demonstrated that liquid viscosity has no effect on the initial wave growth of sinuous waves. This theory also predicts no maximum

growth rate, in contradiction to the inviscid theory. Weihs (46) presented an analysis of the stability of thin, viscous, attenuating sheets. He obtained an analytical solution for unstable waves in the form of a function of parameters thus:

$$\varepsilon = \frac{\gamma\eta^2}{2}(\rho.h)^{\frac{1}{2}}\left[-1 \pm \left(\frac{1+8\ (\rho a.\eta.V_s^{\,2} - \sigma\eta^2)}{\gamma^2\eta^4\rho.h}\right)^{\frac{1}{2}}\right] \quad (2.4)$$

where ε is a temporal amplification factor

γ is the kinematic viscosity of the sheet

η is the wavenumber

h is the sheet thickness

V_s is the sheet velocity

He plotted the wavenumber for which ε attained its largest real positive value against velocity and found that for any finite viscosity, there would be a different wave of maximum instability which was also a function of distance from the nozzle orifice. The only case of a single wave of maximum instability is obtained when the sheet is inviscid, and

$$\eta_m - \frac{\rho a.V_s^{\,2}}{2\sigma}$$

which is identical to the result obtained by Squire. However, when solving Weih's solution with data from this study, wavenumbers were obtained which were of the same order as those predicted by Squires linearized theory.

Effect of Liquid Properties on Disintegration Mechanism

Dombrowski and Munday (47) illustrate the effect of surface tension and viscosity on the formation of sheets from fan spray nozzles. For Newtonian fluids an increase in viscosity leads to greater sheet stability whilst for an increase in surface tension wave motion is inhibited and a form of rim disintegration occurs.

For non-Newtonian fluids, Garner (48) demonstrated that for visco-elastic gels which are in semi-solid form at no applied shear, the intermediate ligaments may persist without finally breaking down into drops. Dombrowski et al. (49) studied the disintegration of a series of aluminium soap petroleum gels after they had been sprayed through single hole fan spray nozzles. The flow characteristics of the gels were characterized by their Gardner consistency; defined by the weight in grams placed on a piston to produce a given rate of fall through the liquid. At low consistencies, the life of the ligaments increases with increasing consistency whilst at 2g Gardner beads are formed on them. At much higher levels the ligaments break into shreds. Courshee (50) compared the disintegration of sheets of water and dilute aqueous gels, and found that the effect of the gel was to reduce the proportion of satellite droplets formed.

The effect of a surface active agent is complex. If wetting agents are added to hard waters, a perforated sheet is produced to an extent depending on the wetting agent concentration. As the concentration is increased the perforations occur at points closer to the orifice. The change in disintegration mechanism is also accompanied by an increase in drop size (47).

Dombrowski and Fraser (28) investigated the atomisation characteristics of slurries and emulsions. They found that in low concentrations, wettable particles had no effect on disintegration mechanisms, even if the particle diameter exceeded the sheet thickness. At higher concentrations, using Fullers earth slurries, wave disintegration was found to give way to a mechanism of disintegration closer to the orifice by tears and holes. Droplet sizes were not measured, although photographs indicated that they increased with concentration.

For emulsions of oil and water, oil globules were found to rupture the sheet when reaching a critical size.

2.2 Liquid Jet Disintegration

The problem of describing jet disintegration has been the subject of theoretical and experimental investigations since about 1833, commencing with the work reported by Savart (51). The first of the theoretical analyses were those of Rayleigh (52) who

employed the method of small disturbances to predict the collapse of an inviscid liquid jet issuing at a low velocity. This method assumes that an arbitrary small disturbance, q, is imposed upon the surface of the liquid jet; the equation for q being of the form:-

$$q = q_o \, e^{\beta t} \cos \left(\eta \frac{x}{a}\right) \qquad (2.5)$$

where q_o is the initial amplitude of disturbance.

β is the time rate of growth of the amplitude.

η is the wave number of disturbance.

x is the axial distance.

a is initial radius of jet.

From the assumption that disturbances of all wave lengths λ, defined by:-

$$\lambda = 2\pi a/\eta \qquad (2.6)$$

act randomly with the same initial amplitude q_o, it follows that the disturbance which grows most rapidly will cause the jet to break up. Rayleigh considered the capillary force to be of major importance and determined the potential energy of the unstable configuration as:

$$\text{P.E.} = - \sigma \left(\frac{\pi q^2}{2a}\right)(1 - \eta^2) \qquad (2.7)$$

The kinetic energy was then found from the hydraulic velocity potential associated with rotionally symmetrical flow. The resulting equation for the time rate of

growth of the disturbance then became:

$$\beta^2 = \frac{\sigma}{\rho.a^3} F(\eta) \qquad (2.8)$$

where $F(\eta)$ is a complex function of wave number based on Bessel function. By re-writing equation 2.8 in terms of a dimensionless variable, γ

where $\gamma = \mu \left(\frac{\rho.a^3}{\sigma}\right)^{0.5}$;

setting the derivative of γ^2 with respect to η equal to zero will result in an equation involving only η. From equations 2.6 and 2.8 the wavelength of the most rapidly growing disturbance was determined as:-

$$\lambda = 4.508 \times 2a \qquad (2.9)$$

Rayleigh's analysis thus predicts a disintegration wavelength which depends only upon the radius of the jet and is independent of the other physical properties of either the liquid jet or the surrounding medium into which it is injected. The size of the drops formed were found from a mass balance and on the assumption that one drop is formed per disintegration wavelength i.e.

$$D = 1.89 \times 2a \qquad (2.10)$$

Duffie and Marshall (23) in a study of varicose break-up observed jets of liquids which gave drop sizes as

predicted by equation 2.10 although each drop was accompanied by a satellite drop.

Castleman (53) investigated the atomisation of a jet of water by the shattering effect of a blast of air by taking high speed photographs. He concluded that the process occurred in two stages; firstly the formation of ligaments and secondly the collapse of those ligaments to form droplets. The Rayleigh analysis was applied to the second stage and predicted results agreeing well with experimental data.

Although Rayleigh's original analysis ignored viscous forces it correlates very well with experimental results obtained from liquids of low viscosity. In a later analysis Rayleigh (54) investigated the stability of a viscous jet under the action of surface tension. The complicated nature of his final equation made it of doubtful value, although the effect of increased viscosity was shown to increase the wavelength of the fastest growing disturbance. Weber (34) considered the same problem as Rayleigh but was able to solve his equation for γ by expanding the coefficients of this equation in series and showing them to be constant for conditions where $\eta < 1$. From an analysis of his simplified equation Weber obtained the wavelength of the most rapidly growing disturbance as:

$$\lambda = 2\pi a \left[2\left(\frac{3We}{Re} + 1\right)\right]^{0.5} \qquad (2.11)$$

Thus for inviscid liquids $\lambda = 4.44 \times 2a$, agreeing well with the results from Rayleigh's analysis. The final form for the break up length of viscous jets became:

$$\frac{L}{d} = \text{Log}_e \left(\frac{a}{q_o}\right) \left[(We)^{0.5} + \frac{3We}{Re} \right] \qquad (2.12)$$

The Stability Curve

If the experimentally determined break-up length of a jet is plotted against the average exit velocity, a curve similar to that shown in Figure 2.1 is obtained. Point B represents a critical velocity of minor significance where the jet changes from drip flow to jet flow. The region BC sometimes termed the laminar linear position, is well understood and is where the theory of Rayleigh and Weber applies. Smith and Moss (55) plotted L/d versus $We^{0.5}$ for several systems and obtained a straight line which passed through the origin. The value for the constant $\log_e (a/q_o)$ was found to be 13 whilst Weber obtained a value of 12 from the data of Haenlein (56). Similar behaviour has been observed by Tyler and Richardson (57). Grant and Middleman (58) working on jets of glycerol/water solutions, reported an average value of 13.4 but pointed out that $\text{Log}_e (a/q_o)$ is more appropriately represented by the correlation:

$$\log_e (a/q_o) = -2.66 \ln Oh + 7.68 \qquad (2.13)$$

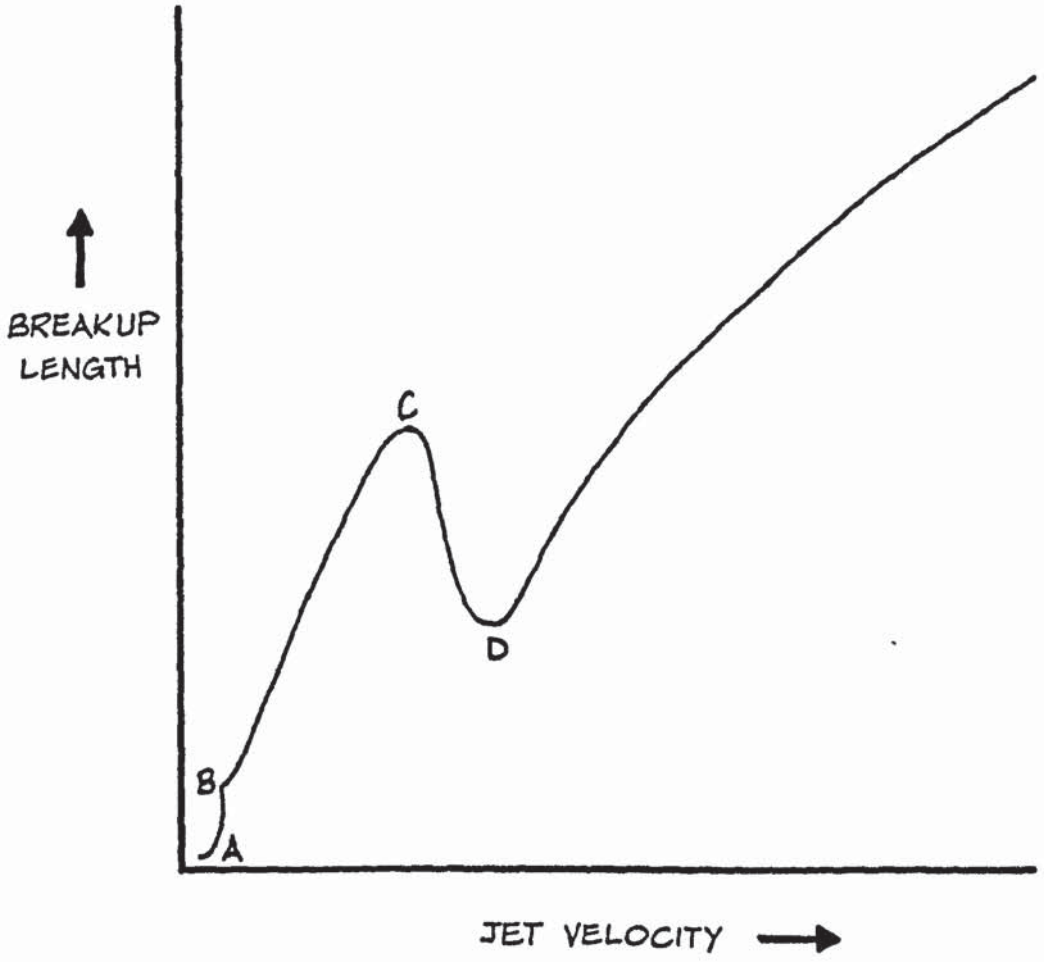

Figure 2.1. Jet Stability Curve.

where $Oh = \mu/(\rho.d.\sigma)^{0.5}$

Phinney (59) assumed that the amplification rate given by Weber's theory was correct and treated the initial disturbance level as a variable. Using the data of various workers he plotted values of $\log_e (a/q_o)$ versus the Reynolds number of the flow through the nozzle. For each curve a critical Re was obtained which marked an increase in the exit disturbance level.

At some point in the stability curve, the linear theory fails and there is a peak (point C). Haenlein (56) observed that at C the disintegration mechanism began to change from symmetrical drop break-up to transverse wave break-up. Weber, guided by these experimental observations, developed relations to describe jet stability taking into account the loading effect of the ambient gaseous atmosphere. The theory predicted that wind loading tended to propagate both axisymmetrical and transverse disturbances, resulting in break-up into drops in the former and wave segments in the latter. The application of the theory showed that it was correct in so far as it predicted a maximum in the jet stability curve. However, quantitative agreement of the theory with Haenlein's experimentally determined critical point (C) was not achieved. A calculation by Levich (60), on the other hand, shows that jet disintegration times associated with the growth of symmetrical or transverse disturbances are approximately the same, thus contradicting Weber's theoretical prediction.

Grant and Middleman modified Weber's characteristic expression for the disturbance growth rate to predict the entire break-up curve for a laminar jet. However, subsequent testing of the modified theory at pressures other than atmospheric proved unsuccessful. Other workers (61) attribute the critical point to turbulence in the jet. Another factor which influences the position of the critical point is the ambient atmosphere. Phinney (62) examined the effect of ambient density and a theory was developed which considered the initial disturbance level as constant. The theory improved upon that of Weber by including the factor "We_a" where $We_a = dV^2\rho_a/\sigma$. A good correlation was obtained by plotting λ against We_a.

Fenn and Middleman (63) also indicated a certain dependency of the position of the critical point on the ambient atmosphere. However for values of We_a less than 5.3, air pressure was found to have no effect on stability. Ambient viscosity through the effect of shear stresses acting on the jet surface was found to give rise to the critical point.

It is probable that some of the discrepancies associated with jet stability studies arise from the choice of nozzle employed. Many workers have used long tubes to promote a fully developed velocity profile within the jet. At the nozzle exit, a velocity profile relaxation mechanism will occur which may add to the

existing de-stabilizing force of surface tension. Smith and Moss, in a comparison of their results with those of Savart (which showed no peak in the stability curve) believed that the different results could be ascribed to difference in the emergent velocity profiles. Rupe (64) observed that high velocity laminar jets may actually be more unstable and break-up in an extremely violent fashion much sooner than fully developed turbulent jet. He attributed this behaviour to the decay of the fully developed laminar profile. This "bursting break-up" was explained by Hooper (65). Evidently, jets with fully developed turbulent profiles on exit are only weakly susceptible to profile relaxation effects, though turbulence may be the deciding factor regarding stability in such cases. However, the most stable jets are laminar with flat profiles and for such jets in vacuo, varicose instability should persist indefinitely. In a gaseous atmosphere however, varicose instability should eventually give way to Helmholtz instability.

Stability of Turbulent Jets

Beyond point D on the stability curve, turbulence apparently stabilizes the jet, but the actual break-up time decreases with increasing velocity. Grant and Middleman (58) developed an empirical correlation for break-up data of turbulent jets issuing from long smooth tubes:

$$L/d = 8.51\ (We)^{0.32} \qquad (2.14)$$

Phinney (66) extended his plots of λ vs Re to turbulent Reynolds numbers, and obtained two constant disturbance level plateaus, the lower of which being inferred to an increase in the exit disturbance level for turbulent jets. He also attempted to separately analyse the effects of the ambient atmosphere and initial disturbance levels using the data of Chen and Davis and others. The main outcome of this work was to establish the advantages of an electrical technique for detecting the break-up point of turbulent jets.

The shape of the stability curve as the jet velocity is increased indefinitely is uncertain. Some workers postulate that L/d continually increases with increasing V (67). The possibility of another maximum in the stability curve has been commented upon (68). Phinney (66) suggests that stripping of the surface layer from the jet due to relative motion with the ambient atmosphere, might dominate the break-up process at high exit speeds, thereby influencing the shape of the break-up curve.

Atomisation of Liquid Jets

Early work by Lee and Spencer (69) suggested, from an extensive photographic investigation into the jet disintegration process, that jet stream turbulence

was of little importance in providing disintegration energy; though its presence would accelerate the process. An atomisation mechanism was proposed whereby ligaments of liquid are drawn out from the jet, become detached and subsequently disperse into droplets. The action of the ambient atmosphere is generally accepted as the main influence on atomisation.

The most commonly quoted criterion for classifying jet disintegration is due to Ohnesorge (70), who determined the relative importance of inertial, gravitational, surface tension and viscous forces, but did not specify the type of nozzle employed. The result of the analysis suggested that the method of jet break-up could be classified into three regions on a graph of Ohnesorge number versus Reynolds number (Figure 2.2). The areas are where:

(a) The jet breaks up into large uniform drops (Rayleigh type break up).

(b) The jet breaks up into waves producing a wide size distribution of drops.

(c) Secondary atomisation occurs, in which the action of aerodynamic forces are involved.

Miesse (71) translated the boundary between regions II and III to the right (indicated by dotted line in Figure 2.2) so that his data fell into the appropriate areas. Whilst Figure 2.2 may be used as a guideline, McCarthy (72) reported jets which exhibited the complete

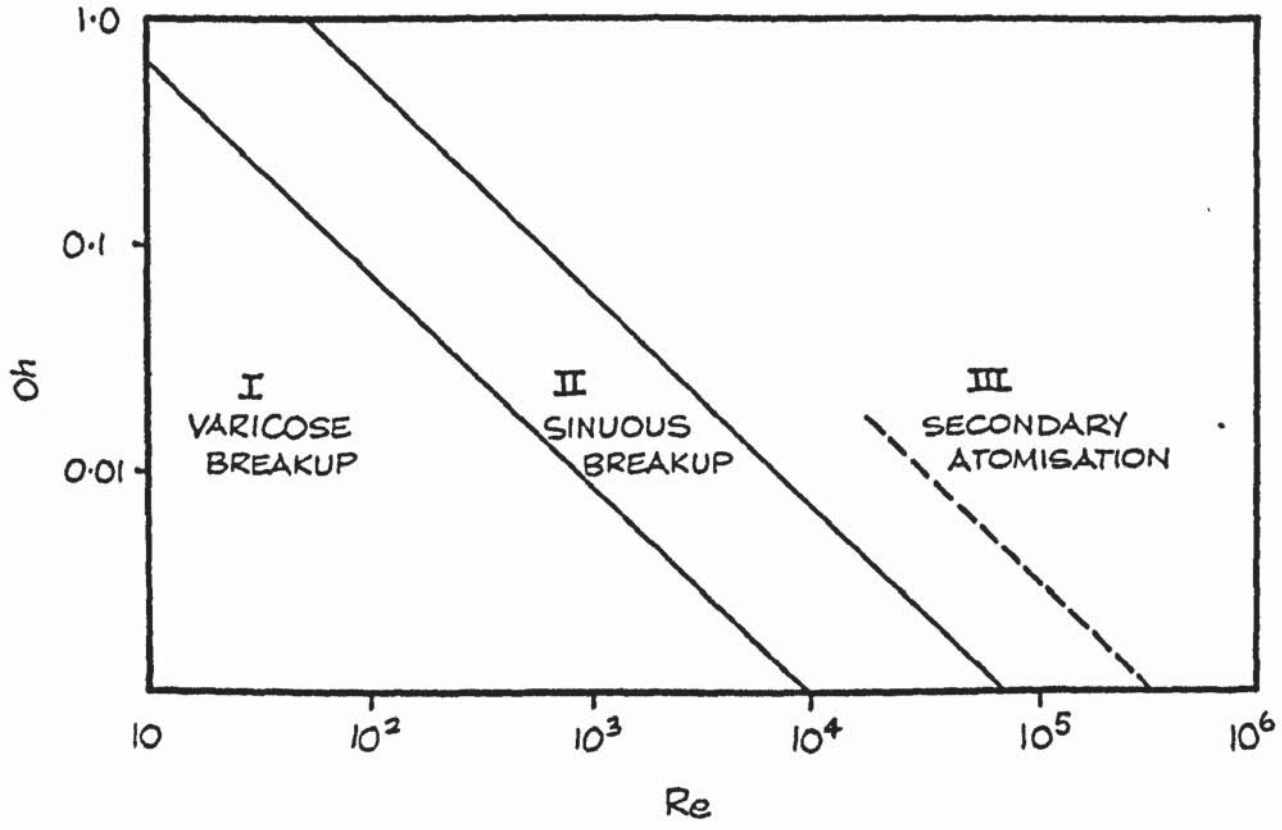

Figure 2.2. The Ohnesorge Chart.

spectrum of disintegration mechanisms though all were represented by the same point on Ohnesorge's graph.

Sakai et al. (73) investigated experimentally the transitional conditions from a wavy jet to a spray jet disintegration mechanism. Their results were expressed in an empirical dimensionless form which related Reynolds and Weber numbers to the discharge coefficients of orifices. They also noted that relatively coarse droplets were formed from ligament disintegration whilst much finer droplets were formed on transition to the spray disintegration mechanism. Thus from their proposed empirical formula they hoped to clarify jet nozzle design procedures for spray operations requiring coarse or fine particles.

The major theoretical investigations into jet stability have been provided by Rayleigh and Weber, who from a linearised analysis assumed that the amplitude of the disturbance to be relatively small compared with the jet diameter. These linear theories predict that a jet subjected to capillary and inertial forces would break up into uniform sized drops, with one drop formed per disturbance wavelength. The form of the disturbed jet surface is assumed to be an amplifying sinusoidal curve. When compared to the practical case, however, the shape of the jet is not sinusoidal, and in addition, satellite droplets are present between the major drops; not predicted by linear theory.

Linear theory predicts that the wavelength of the fastest growing disturbance is 4.51d, whilst experimental work is only in approximate agreement. Generally experimental values for the coefficient tend to be rather higher than the linearised prediction. Wang (74) in a non-linear analysis of jet disintegration showed that the wavelength of the most unstable disturbance to be a function of the magnitude of the initial disturbance, which explains to some extent the reported variations in wavelength.

From imposed acoustic oscillations on a jet, Donnelly (75) showed the growth rate to be constant and in satisfactory agreement with Rayleigh's linearised theory, even at the point where the surface shape deviates from sinusoidal. This suggests that jet disintegration is not markedly affected by non-linear effects.

The non-uniformity of droplet sizes has been suggested (76) to be a result of secondary waves on the neck between adjacent wave crests and have been observed experimentally by Rutland (77). Rutland also showed that a mono size drop distribution would only occur if the main droplet and satellite droplet were of equal volume. This was achieved practically by imposing disturbances of wave number between 0.35 and 0.5.

This technique of imposed oscillations is thus a

means for controlling drop sizes and is illustrated by Roth and Porterfield (78).

Non-Newtonian Jets

Goldin et al. (79) examined the stability of laminar jets of non-Newtonian fluids by means of a linearised stability analysis. It was shown that for those fluids with no finite yield stress, the growth rate of disturbances is always larger than for Newtonian fluids possessing the same zero shear viscosity. Fluids having a finite yield stress were found to lead to a completely stable jet. One basic shortcoming in this theory is the assumption that the proportion of the fluid leaving the nozzle are those of the fluid in its equilibrium state. The fluid in the nozzle is however, highly stressed and a relaxation time must be accounted for. In addition the gel structure of a highly viscous liquid is destroyed under high shear rates and will take a finite time to reform. In a later paper (80) Goldin investigated the break-up of capillary jets of various viscous non-Newtonian fluids. Inelastic liquids with strongly shear dependent viscosities were found to exhibit similar instabilities compared with those of a Newtonian fluid possessing a viscosity corresponding to the average viscosity inside the capillary. These instabilities were found to be related to the

reformation time of the liquid structure. Elastic fluids with strong normal forces having similar shear viscosities were found to be stable.

Kroesser and Middleman (81) extended Weber's theory for the Newtonian jet to a linear viscelastic vluid. The theory predicted that viscoelastic jets have shorter break-up lengths at constant We and Oh. The elasticity number $(\tau\mu_o/\rho.d^2)$

where τ is the relaxation time.

μ_o is the zero shear viscosity.

was found to be a key parameter. Experimental data of samples of P.I.B. in tetralin confirmed the reduced stability of viscoelastic jets. Their theory failed to account for the effect of normal stresses within the capillary. Experimental results did indicate a certain dependency of break-up length upon tube length which may have been associated with a normal stress effect.

Gordon et al. (82) studied the instability of various solutions of Carbupol and of Separan in water under the influence of externally controlled disturbances. The entire work however, related to laminar jets not affected by interactions with the surrounding air. Jets of a 0.1% carbopol solution showed a break-up pattern similar to that of water. On jets of 0.1% Separan no sinusoidal wave formation was observed and a ligament-droplet configuration formed from the outset.

On the less elastic 0.05% Separan jets an initial region of exponential sinusoidal wave growth was observed which later transformed into the ligament-droplet configuration. In this initial region the growth rates are similar to those of a Newtonian fluid of the same zero shear viscosity. In addition the ligaments that form on jets of Separan were found to undergo a stretching motion which accounted in part for their unusual stability.

Chapter 3

Atomisation by Swirl Spray Nozzles

3 Atomisation by Swirl Spray Nozzles

The principle of the pressure nozzle is the conversion of pressure energy within the liquid bulk into kinetic energy of thin moving liquid sheets. A conical sheet is produced because the liquid is made to emerge from an orifice with a tangential or swirling velocity resulting from its path through one or more tangential or helical passages inside the nozzle. In such swirl spray nozzles the rotational velocity is sufficiently high to cause the formation of an air core throughout the length of the nozzle and the internal design of the centrifugal pressure nozzle is critical and the important dimensions are shown in the schematic diagram, Figure 3.1. The methods of imparting the rotary motion within the nozzle include use of spiral grooved inserts, inclined slotted inserts, swirl inserts, or simple use of tangential entry. The nozzles used in this work had swirl inserts and the construction of the nozzle is shown in Figure 3.2.

The form of the conical sheet depends upon the working pressure and its shape passes through a number of stages as the pressure is increased. At low pressures the liquid emerges as a thin twisted jet. With increased pressure the jet opens to form a 'tulip' and as the pressure is further increased the 'tulip' opens up to form a hollow cone with curving sides. These sides straighten up with increasing pressure. The fully

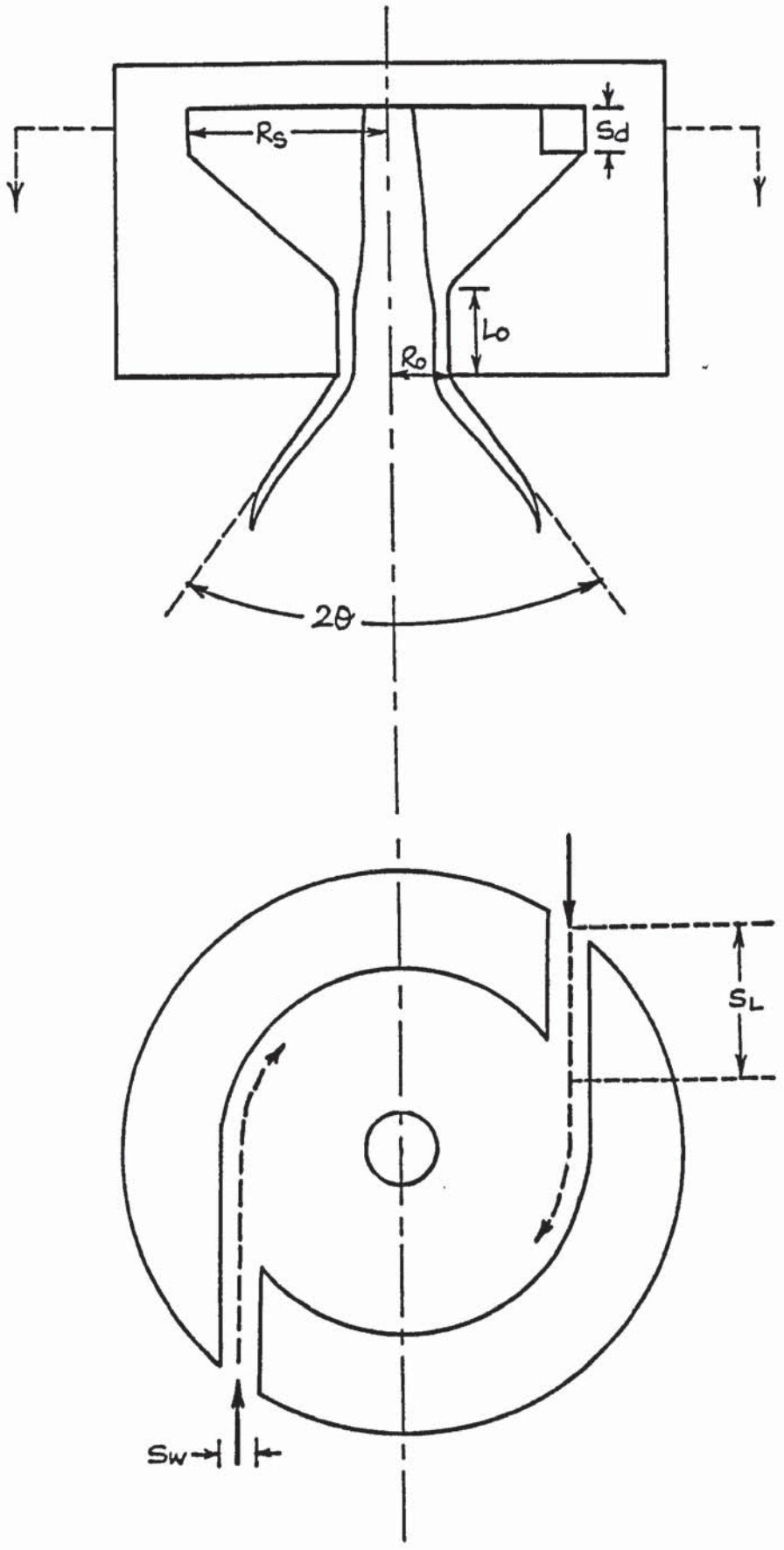

Figure 3.1. Schematic Diagram of a Swirl Nozzle.

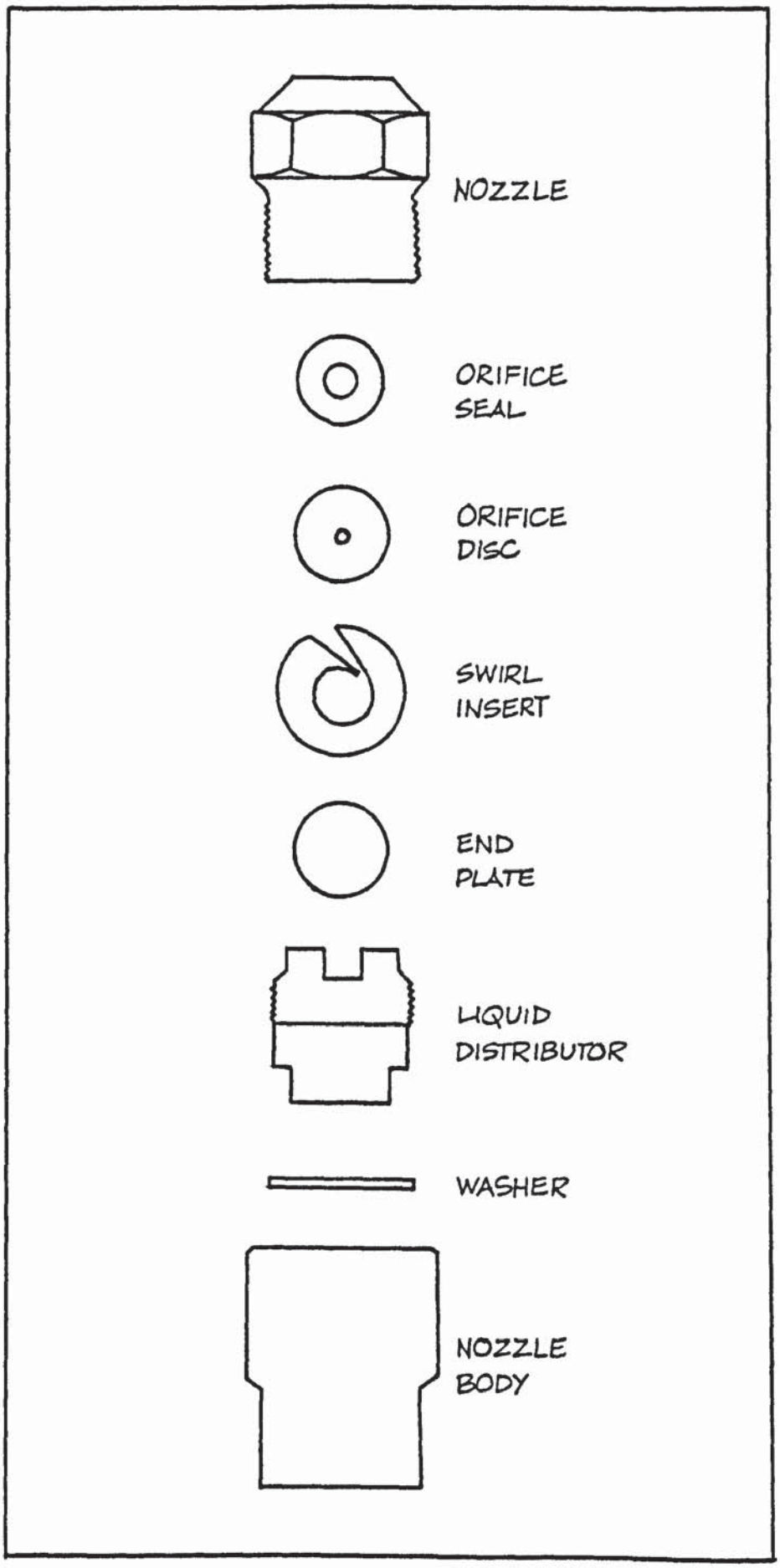

Figure 3.2. Construction of a Delavan SDX Swirl Nozzle.

developed cone has been shown by Tanasawa (83) to occur when Re > 2800; where Re is defined:

$$Re = \frac{V_I R_s \rho}{\mu}$$

The hydrodynamics of flow through swirl spray nozzles has been considered by many workers. Marshall (84) considered a fluid flowing in two concentric streamlines a distance dr apart. Then for a differential element of surface area dA, radius of curvature r and point tangential velocity v_θ the elemental mass = $\rho dr dA$ and the radial acceleration = v_θ^2/r.

A force balance in a radial direction yields on simplification

$$\frac{dP}{dr} = \frac{\rho}{g} \frac{v_\theta^2}{r} \qquad (3.1)$$

Equation (3.1) gives a general expression of the pressure gradient for liquid flowing along a curved path, and the exact variation of pressure with radius can only be defined where the relationship between v_θ and r is known. These relationships describe the flow pattern within the atomiser but the literature usually describes complete solutions of this problem for the two extremes; either

1) Free-vortex flow, which corresponds to a liquid of zero viscosity, or

2) Forced vortex flow, which is the limiting condition resulting from viscous drag within the atomiser.

In practise, an atomiser will operate somewhere between these extremes.

In free vortex flow therefore, there is no dissipation of energy by viscous forces and the total pressure energy is convertedinto kinetic energy. The tangential velocity can be derived from the expression for the torque which gives a change in angular momentum:

$$F_A.r = \frac{d}{dt} (mv_\theta r)$$

where F_A = force applied.

From the definition of free vortex, the liquid flows in a curved path with no applied torque so that

$$\frac{d}{dt} (mv_\theta r) = 0 \qquad (3.2)$$

thus $v_\theta.r$ = constant = Ω (3.3)

In order to satisfy equation (3.3), v_θ tends to infinity at the nozzle axis where r = 0. This condition cannot be fulfilled and instead the liquid flowing through the nozzle cavitates and an air core is formed.

Many workers have attempted to predict the throughput characteristics of swirl atomisers, usually by following the method of Novikov (85), who assumed free vortex flow. From the conservation of angular

momentum he obtained

$$v_\theta r = v_{\theta_o} R_o = v_{\theta I} R_I \qquad (3.4)$$

where I and o denote the inlet and outlet of the nozzle respectively.

The Bernouilli equation for the energy balance was written as

$$\frac{\Delta P}{\rho} + \frac{\Delta v_\theta^2}{2g} + \frac{\Delta v_z^2}{2g} + \frac{\Delta v_r^2}{2g} = 0 \qquad (3.5)$$

The axial velocity was related to the radius of the air core (r_{ac}) by the equation of continuity, thus:

$$\pi R_I^2 v_{\theta I} = \pi (R_o^2 - r_{ac}^2)\, V_z \qquad (3.6)$$

Novikov used the hypothesis of Ambrovitch (86) that the air core radius is constant:

$$\frac{\partial Q}{\partial r_{ac}} = 0 \qquad (3.7)$$

and solved equations (3.3), (3.4), (3.5), (3.6) and (3.7) to yield

$$Q = C_D \pi R_o^2 \left(\frac{2gP}{\rho}\right)^{0.5} \qquad (3.8)$$

where C_D = the discharge coefficient, defined as the ratio of the actual liquid throughput to that theoretically possible under ideal conditions, and by equation (3.9) as

$$C_D = \frac{\alpha(1-\alpha)^{0.5}}{(1-\alpha + \alpha^2 A^2)^{0.5}} \qquad (3.9)$$

where $A = \frac{R_o R_s}{R_I^2}$ (3.10)

and $\alpha = 1 - \frac{r_{ac}^2}{R_o^2}$ (3.11)

α is thus the ratio of the available flow area to the total orifice area. Both A and α are dimensionless parameters which depend on the geometry of the nozzle and are related by:

$$A = \frac{1 - \alpha}{(\frac{\alpha^3}{2})^{0.5}} \quad (3.12)$$

Doumas and Laster (87) calculated discharge coefficients from their data and found them to be in poor agreement with values obtained from equation (3.8). However a good correlation was obtained by modifying equation (3.10) using the dimensionless quantity $(\frac{R_o}{R_s - R_I})^{0.5}$. They suggested that this experimental modification is needed to allow for the effect of frictional drag at the nozzle surfaces and between various liquid layers. Harvey and Hermandorfer (88) attempted to describe the actual vortex within a swirl chamber as a combination of a free and forced vortex. They defined the cone angle 2θ by analogy with an expression for free vortex flow as

$$2\theta = 2 \tan^{-1} (\frac{CL}{M}) \quad (3.13)$$

where M = ratio of total inlet to outlet orifice area $\frac{R_I^2}{R_o^2}$

L = ratio of chamber to outlet orifice radius = $= \frac{R_s}{R_o}$

C = a parameter = $\frac{C\ d_o . C_h}{C_{dI}}$

Cd_o, C_{dI} are the discharge coefficients for the outlet and inlet orifices, and were assumed equal to one. C_h is the hollow cone discharge coefficient. Since equation 3.13 is based on frictionless flow, this method does not significantly improve upon the simple vortex theory.

The discrepancies reported between theoretical and experimental discharge coefficients were explained to some extent by Taylor (89), who applied boundary layer theory to the flow. He considered that viscous drag at the surface of the swirl chamber retards the rotating liquid which is unable to remain in a circular path against the radial pressure gradient balancing the centrifugal motion. Consequently a current is set up directed towards the orifice through a surface boundary layer.

Taylor deduced the following expressions for boundary layer thickness, δ.

$$\frac{\delta}{R_o} = \frac{\delta_1}{R_D} \left(\frac{\nu}{\sin\alpha}\right)^{0.5} \tag{3.14}$$

and

$$\delta_1 = \frac{\delta}{R_o} \left(\frac{\Omega'}{\nu \sin\alpha}\right) \tag{3.15}$$

where R_o = outlet orifice radius

R_D = r/R_3, a dimensionless distance from the swirl chamber apex to any point in the chamber cone.

r = distance along cone from apex to swirl chamber inlet.

The circulation constant Ω is defined by equation (3.3) but Taylor modified this to account for frictional drag and defined Ω' as:

$$\Omega' = C_D \frac{R_o^2}{R_I} U_T R_s \tag{3.16}$$

where U_T is a velocity equivalent to the total pressure head H

$$= \left(\frac{2gH}{\rho_L}\right)^{0.5} \tag{3.17}$$

Taylor assumed a free vortex flow and a negligible axial velocity component in order to derive an expression for the boundary layer thickness due to rotational flow. He obtained a functional relationship between δ_1 and R_D enabling values of δ to be calculated.

On the basis of these assumptions he showed that

a large proportion of the total flow through the orifice was via the boundary layer, even for low viscosity liquids. Hodgkinson (90) has also shown that part of the flow through the orifice may also be derived from a boundary layer surrounding the air core.

McIrvine (91) presented a comparison of the values of boundary layer thickness predicted by Taylor's theory and experimental values of film thickness obtained in a study of air cores by high speed photography. However his results indicated that the boundary layer thickness comprised a substantial part of the film thickness when spraying high viscosity liquids.

Dombrowski and Hasson (92) from theories based on the work of Taylor (93) showed that the discharge coefficient and cone angle were directly related to the nozzle parameter

$$\Delta^1 = \frac{A_s}{d_o d_m}$$

where A_s = area of inlet swirl channel

d_m = mean diameter of inlet vortex in swirl chamber

d_o = orifice diameter.

Deviation from ideal flow conditions were corrected in terms of the ratio of orifice length to diameter, correlated against a correction factor F_1. This factor is combined with the nozzle parameter and the ratio $(d_m/d_o)^{0.5}$ to form a modified parameter:

$$F_1\left[\left(\frac{A_s}{d_o d_m}\right)\left(\frac{d_m}{d_o}\right)^{0.5}\right]^{0.67}$$

The relationship between cone angle, discharge coefficient and the modified parameter are given in the source reference.

The disintegration of the liquid sheet will be controlled to some extent by the properties the liquid possesses as it issues from the orifice. Joyce (94) stressed the importance of the ratio of orifice length to diameter, (L_o/d_o). As this ratio was increased for fixed d_o, the resultant spray had properties identical to that of the spray formed at low pressures for a shorter length. Most workers have tried to compare their theoretical analyses of flow patterns within a swirl chamber with experimental results using the cone angle of the emergent sheet. The point velocity of any liquid particle is the resultant of its tangential and axial velocity, and will vary across the sheet thickness. The resultant cone angle is related to the vector sum of these local velocities and thus an expression must be derived to represent this average effect.

If the path of one liquid element is considered the expression for θ can be derived by simple geometry as:

$$\tan \theta = \frac{V_T}{V_A}$$

where V_T and V_A are the tangential and axial velocities at the orifice. The calculated or measured cone angle is often used as a criterion in comparing the fineness of atomisation for different nozzles operating under identical conditions; the largest cone angle usually representing the smallest drop sizes.

Representation of Sprays

The droplet sizes which are produced by atomisation are not uniform but cover a range of sizes. Most researchers and nozzle manufacturers frequently report a single parameter as an indication of droplet size usually the volume surface mean diameter, D_{32}. However, a single parameter does not adequately define the complete droplet size distribution. One means of describing the size distribution is via a plot of drop diameter versus the cumulative volume percentage undersize, but this method is not ideal for calculating the various mean diameters associated with a distribution. A more convenient method is to represent the size distribution as a continuous function by mathematical distribution equations. Table 3.1 lists the droplet size distribution functions which have been considered most frequently.

Rosin and Rammler (95) developed the following empirical equation to describe a range of powdered coal sizes

Table 3.1. Droplet Size Distribution Functions

Type	Equation
Normal	$\frac{d(N)}{d(D)} = \frac{1}{S_N\sqrt{(2\pi)}} \exp -\left[\frac{(D-\overline{D})^2}{2S_N^2}\right]$
Log-Normal	$\frac{d(N)}{d(D)} = \frac{1}{D.S_G\sqrt{(2\pi)}} \exp -\left[\frac{(\text{Log } D-\text{Log } D_{GM})^2}{2S_G^2}\right]$
Square-Root Normal	$\frac{d(N)}{d(D)} = \frac{1}{2\sqrt{(2\pi.D.S_G)}} \exp -\left[\frac{(\sqrt{D}-\sqrt{D_{GM}})^2}{2S_G^2}\right]$
Upper Limit	$\frac{d(N)}{d(D)} = \frac{1}{D.S_G\sqrt{(2\pi)}} \exp -\left[\frac{\text{Log}((D_{MAX}-D)/D_{GM})^2}{2S_G^2}\right]$

where D is droplet size

$\overline{D}$ is the mean diameter

d(N) is number of droplets in size increment

S_N is the number standard deviation

D_{GM} is the geometric mean size

S_G is the geometric standard deviation

$$R = \exp\ (-b\ D^n) \qquad (3.19)$$

where R is the fraction greater than size D, by weight or volume, b, n, are parameters of the distribution. Equation 3.19 is expressed in terms of number frequency of drop sizes by use of 3.20, the general equation for conversion of volume frequency to number frequency:

$$\frac{d(N)}{d(D)} = \frac{6}{\pi D^3}\ \frac{d(V)}{d(D)} \qquad (3.20)$$

This yields the Rosin-Rammler equation in terms of numbers as

$$\frac{d(N)}{d(D)} = \frac{6b}{\pi}\ n\ D^{(n-4)}\ \exp\ (-b\ D^n) \qquad (3.21)$$

Mugele and Evans (96) studied the application of this distribution to spray droplets and found it to be unreliable for calculating mean diameters. However, certain automatic drop size analysers use this distribution equation to represent data.

Nukiyama and Tanasawa (3) developed an empirical equation describing the drop size distribution obtained from pneumatic atomisers. The equation could be expressed in its most general terms as:

$$\frac{d(N)}{d(D)} = a\ D^m\ \exp\ (-b\ D^n) \qquad (3.22)$$

and fitted their results with values of m = 2 and n = 1.

The Rosin-Rammler expression (3.21) is thus a special form of this general equation with m = n-4. Nearly all empirical expressions that have this

exponential form have been found to be special cases of (3.22). Mugele and Evans found that the Nukiyama-Tanasawa equation gave a good fit to droplet size data, but in some cases led to certain mean diameters that were larger than any values observed experimentally.

The majority of data on drop distributions have been correlated using the basic statistical concept of a normal (Gaussian) distribution. However, experimental data has not been found to fit this distribution exactly, in particular from pressure atomisers where the drop sizes are skewed towards the lower end of the size range. Various workers have suggested modifications to the normal distribution. Kottler (97) developed the log normal distribution for sprays by assuming that the droplet size is the result of a large number of small impulses, the effects of which are proportional to the size of the drop. This distribution has been found applicable to represent sprays from rotary atomisers (1).

The square root normal distribution was developed by Tate and Marshall (98) in fitting their data on drop sizes produced by centrifugal pressure nozzles of the grooved core type. It is similar in form to the log normal distribution in that log D is replaced by $\sqrt{D}$. However, the accuracy of various mean diameters calculated from this distribution was not reported. Dombrowski (99) has also found the square root normal distribution to fit data from swirl spray nozzles.

Mugele and Evans developed the log normal distribution to include a stable maximum drop size so permitting greater flexibility in fitting experimental data. The upper limit distribution places practical limits on the minimum and maximum droplet size whereas the log normal distribution permits extremely large droplets with low frequency of occurrence. Nelson and Stevens (100) compared the normal, square root and upper limit distributions using data obtained from centrifugal pressure nozzles. More recently, Goering and Smith (101) applied the upper limit distribution and found it to fit size distributions from a wide variety of spray nozzles. Various mean diameters could also be calculated from this equation.

Although a drop size distribution completely defining a spray system is helpful to fully analyse its properties, it is also convenient to express the drop spectrum in the form of an average or mean diameter. The type of mean diameter calculated, depends upon its particular field of applications. Those in common use have been generalised in one expression, written as:

$$\bar{D}_{qp} = \left(\frac{\Sigma ND^q}{\Sigma ND^p}\right)^{\frac{1}{q-p}} \qquad (3.23)$$

where q and p have values according to Table 3.2.

Although the literature on atomisation is quite extensive, the prediction of drop size from the

Table 3.2

Mean Diameters, $\overline{D}$ from Equation 3.23

p	q	Common Name of Mean Diameter	Application
0	1	Linear	Comparisons, evaporation
0	2	Surface	Absorption
0	3	Volume	Flow through porous beds
1	2	Surface Diameter	Adsorption
1	3	Volume Diameter	Molecular diffusion
2	3	Sauter, volume surface	Mass transfer
3	4	De Brouckere	Combustion

properties of the liquid and atomiser is still very uncertain, many of the reported equations being specific to one set of conditions. The major investigations have led to a number of empirical formulae relating mean drop size to the operating variables. The complex process of drop formation from a flat (inviscid) sheet of the type formed by spray nozzles, subjected to aerodynamic sinuous waves, has been idealized by Dombrowski and Hooper (30) as in Figure 3.3. This shows that the waves on the sheet continue to grow until the crests are blown out into half wavelengths which rapidly contract into ligaments which in turn break up into drops.

The volume of liquid per unit width in a half wavelength of sheet is

$$\frac{\lambda opt}{2} h^* = \frac{\pi d_L^2}{4} \qquad (3.24)$$

where h* is the sheet thickness.

thus $d_L = 0.8\ (\lambda opt\ h^*)^{0.5}$ (3.25)

The ligaments were then assumed to disintegrate by varicose break-up in accordance with Rayleigh's theory and thus for sinuous waves the drop size is given by:

$$D = 1.50\ (\lambda opt\ h^*)^{0.5} \qquad (3.26)$$

However for high atmospheric air density, dilational waves were found to predominate and the sheet breaks up into whole wavelengths and the drop size is given by:

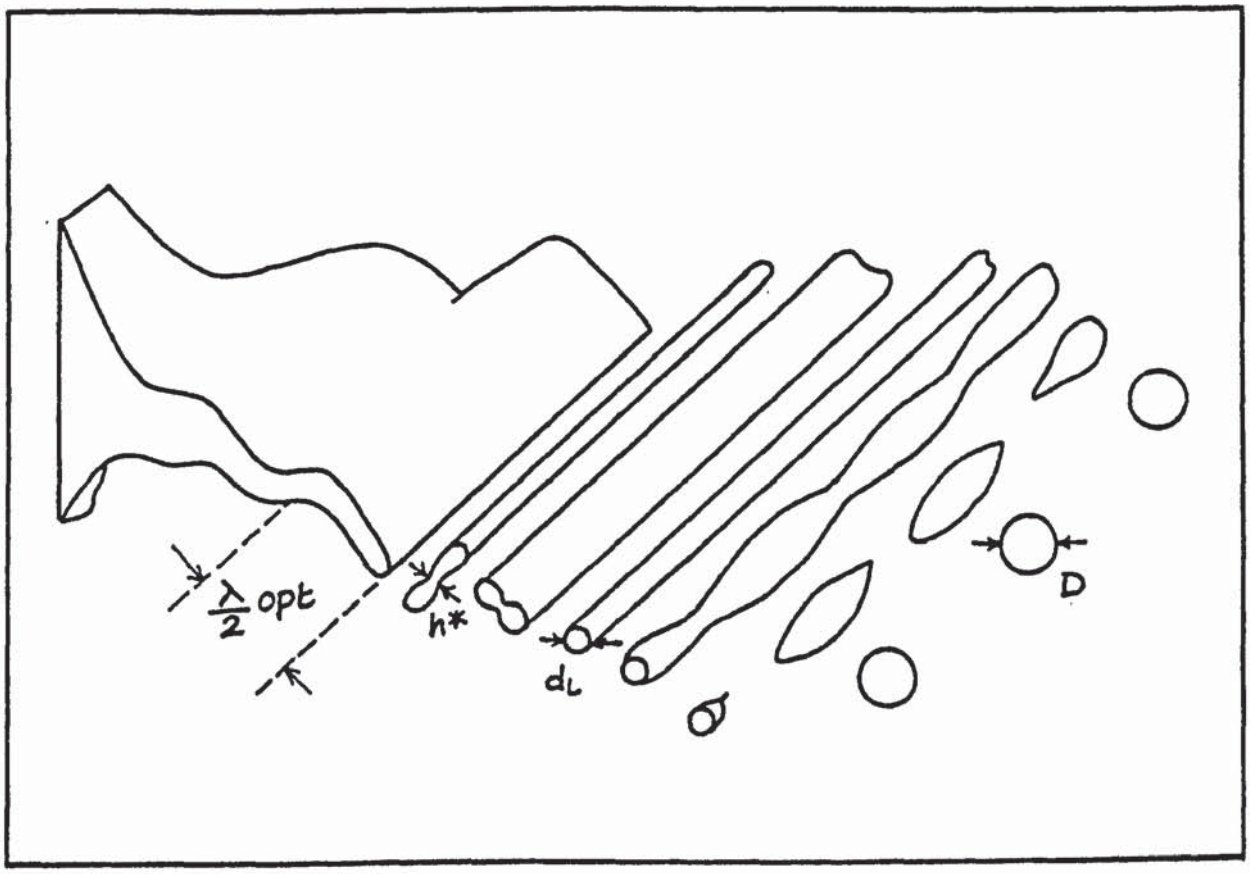

Figure 3.3. Sheet Breakup after Dombrowski.

$$D = 2.12\ (\lambda_{opt}\ h^*)^{0.5} \qquad (3.27)$$

A theoretical analysis was presented for the various regimes of break-up, and from the expression for the sheet velocity given by;

$$V_s = 8.4\ C_D\ (2g\ \frac{\Delta P}{\rho_L})^{0.5} \qquad (3.28)$$

an equation was derived which predicted the drop size for the normal practical case, i.e. where the sheet is broken up by waves of small wave number when $nh < 0.25$.

$$D = \text{const}\ (\frac{K_o.\sigma}{C_D^{\,2}\Delta P})^{0.33}\ (\frac{\rho_L}{\rho_g})^{0.16} \qquad (3.29)$$

Equation (3.29) shows that the drop size is a direct function of the surface tension and liquid density, and an inverse function of the atomising pressure and the air density.

In a study of the break-up of flat viscous liquid sheets, Dombrowski and Johns (40) derived a theoretical expression for the drop size, which correlated well with experimental results.

$$D = (\frac{3\pi}{\sqrt{2}})^{0.33}\ d_L \left[\ 1 + (\frac{3\mu}{(\rho_L \sigma d_L)^{\frac{1}{2}}})\right]^{0.16} \qquad (3.30)$$

where the ligament diameter, d_L is given by

$$d_L = 0.96\left(\frac{K_o^{\,2}\sigma^2}{\rho\ U^4}\right)^{0.16}\left[\ 1+2.6\mu\left(\frac{K_o\rho_g^{\,4}U^7}{72\rho_L^{\,2}\sigma^5}\right)^{0.33}\right]^{0.2} \qquad (3.31)$$

In principle, the analytical methods used for fan spray sheets can be applied to the conical sheets produced by swirl spray nozzles. Dombrowski (99) re-arranged equation (3.29) in terms of the sheet velocity, V_s, to give

$$D = C_1 \left(\frac{\sigma K_T}{V_s^2}\right)^{0.33} \left(\frac{\rho_L}{\rho_g}\right)^{0.16} \qquad (3.32)$$

where k_T is the sheet thickness parameter given by

$$k_T = hr \qquad (3.33)$$

By continuity, the flowrate at any point r along the conical sheet is given by:

$$Q = 2\pi rh\ V_s \sin\theta \qquad (3.34)$$

Hence combining (3.32), (3.33) and (3.34) an expression for the drop size from conical sheets was obtained as

$$D = \frac{C_2\ Q^{0.33}}{V_s\ (\sin\theta)^{0.33}} \qquad (3.35)$$

In practise however, the drop size was found independent of the cone angle and results were correlated by regression analysis in terms of throughput and atomising pressure (equation 3.58). Most workers have based their results on empirical correlations, a number of which are listed in Table 3.3. Many of the correlations apply specifically to one design of nozzle and atomising liquid, and these are described where applicable.

The effect of operating variables on droplet size can be generalised to a certain extent. For instance most workers have found that drop sizes are increased with increase in flowrate within the range of a particular nozzle and also with an increase in orifice diameter, other nozzle parameters being held constant. An increase in the spray angle tends to reduce drop size. Droplet size decreases with increasing atomising pressure and for most purposes varies with $(P^{-0.5})$ over a limited range. An increase in liquid viscosity is generally found to increase drop sizes and the relation $(\mu^{0.2})$ is a typical illustration. This trend may be misleading in that other operating variables are also affected by viscosity, in particular sheet velocity.

Energy imparted to the fluid has to overcome both viscous and surface tension forces and hence liquids of high surface tension become more difficult to atomise resulting in larger drop sizes. Within the range of liquids normally atomised, surface tension variability is usually quite small so that the effects of surface tension changes on droplet size are less significant than for change in viscosity. The equations of Turner and Moulton are unique in placing surface tension of greater significance than viscosity, (see Table 3.3, equations 3.49, 3.50), which

may be misleading since over the range of viscosity investigated (less than 3cP) influence would be minimal.

Some workers have expressed drop size in terms of a flow number (FN) where

$$FN = \frac{Q}{P^{0.5}} \qquad (3.36)$$

According to Fraser (102), FN may also be obtained directly from the relation

$$FN = 293\ C_D\ A_o \qquad (3.37)$$

where A_o is the orifice area in cm^2.

Darnell, however, in contrast to other workers, found drop size independent of flow number (see equation 3.46 in Table 3.3). Tate and Marshall (equation 3.48) predicted nozzle performance in terms of the axial and tangential velocity components of the liquid sheet at the orifice. Thus details of film thickness are required before their equation can be applied, and this information can be obtained either by experimental work or through the work of Doumas and Laster.

The work of Nelson and Stevens using grooved core nozzles necessitated two separate correlations for the organic liquid and water data. Their results support the square root normal size distribution, in agreement with the results of Tate and Marshall. The velocity term used in defining the Re and We numbers is based

on the average axial velocity through the liquid film thickness at the orifice. This quantity, together with the spray cone angle was obtained from the work of Darnell. Wang and Tien (111) used the data of Nelson and Stevens together with their own results to obtain a more general correlation for grooved core nozzles (equation 3.59). This work is of significance in that non-Newtonian liquids were also selected for study. Wang and Tien extended the analyses of Taylor (89) to non-Newtonian fluids by replacing the viscosity term in the Navier Stokes equation with a shear stress-shear rate relation for power law fluids and were able to estimate the boundary layer thickness (δ) at the orifice. They then correlated values of δ for both Newtonian and non-Newtonian fluids against the mean drop size, thus:

$$Y = 0.671X - 0.433 \qquad (3.38)$$

where $Y = \log_{10} (\delta)$

and $$X = \log_{10}\left[(D_{v50})\ R_e^{-0.436}\ W_e^{0.258}\ A^{-0.339} \right]$$

where A is the ratio of the orifice area to the total flow area of the grooved slots. Non-Newtonian behaviour was characterized by the apparent viscosity of the fluid at a shear rate of 2.0×10^5 sec^{-1}; a value based on the ratio V_z/h, where V_z is the axial velocity based on the film thickness at the orifice.

Dombrowski (99) in a study of drop size characteristics when spraying water through various nozzles, found the mean drop sizes independent of nozzle design, and were simply correlated against flowrate and atomising pressure (equation 3.58). In a later study (112), Dombrowski atomised a range of oils and found that drop sizes were inversely related to pressure and directly to viscosity in confirmation with the generally accepted findings. However when he plotted mean drop size against ejection velocity, drop size was found to be independent of viscosity. Thus the viscosity dependency of drop size shown in equation (3.60) is derived essentially from the effect of viscous forces within the nozzle upon the sheet velocity.

Dombrowski also studied the flow pattern within a perspex model of a spray nozzle and found that the high viscosity liquid produced the most disturbed air core. The non-dependence of drop size on viscosity for a given sheet velocity was therefore assumed to be due to the viscous forces opposing breakdown of the sheet being offset by the greater disturbances imparted to the sheet from the swirl chamber.

El-Awady (113) attempted to resolve the conflicting results of the effect of viscosity on drop size. He proposed two hypotheses for atomisation, whereby the

droplets separate laterally from liquid sheet or ligament against the forces of either surface tension or viscous shear. A criterion was proposed where the relevance of either tension or shear principles depended upon the value of X, a dimensionless parameter defined by

$$X = \frac{\mu}{\sigma} \left(\frac{P}{\rho_L}\right)^{0.5} \tan\theta \qquad (3.39)$$

Thus viscosity is only of significance when the shear principle applies and $X < 0.25$.

Mani (114) using the data of various workers, attempted to correlate mean drop size against the vortex strength created in the nozzle swirl chamber. No empirical correlation was presented and the data only gave a linear relationship when plotted in semilogarithmic coordinates. The available range of droplet sizes obtained with swirl nozzles is extensive. The width of the distribution is dependent on nozzle dimensions, operating pressure and feed conditions. Simmons (115) presented data on the drop size/volume fraction distribution of sprays observed with a large number of such nozzles of various types using a range of fuel viscosities at a variety of operating conditions. He established a non-dimensional correlation when the drop size was normalised to the mass median diameter, so that the distribution of any given spray could be predicted from either the mass median or Sauter mean diameter.

DROP SIZE CORRELATIONS FOR VARIOUS TYPES OF SWIRL ATOMISER

Author	Equation No.	Equation and Application	Droplet Measuring Technique
Longwell (103)	3.40	$D_{v5o} = \frac{do\, K_L \exp\,(0.75^{\mu/P})}{2 \sin\,(2\theta)\Delta P^{0.375}}$ Fuel oils ; $K_L = 0.72$	Collected in cold alcohol bath and sieved
	3.41	$D_{32} = 157\ (\frac{\sigma}{P})^{0.5} + 597\ (\frac{\mu}{(\sigma\rho_L)^{0.5}})^{0.45}\ (\frac{1000\ Q}{K\ d_o (P/\rho_L)^{0.5}})$	
	3.42	$D_{32}\ \alpha\ \frac{1}{\Delta P^{0.35}}$	Heated substitute liquid solidified at room temperature.
	3.43	$D_{32}\ \alpha\ \frac{\mu^{0.2}}{P}$ ΔP 20-200 psi Q 5-40 gph Paraffin waxes	

Straus (105)	3.44	$\log_{10} D_{32} = 1.808 + \frac{6.94}{\Delta P} + 0.138\ (FN)$ Grooved core swirl insert ΔP 25-100 psi $2\theta = 60^{o}$ FN 0.05 - 2.0 Water	Collection cell
Weinberg (106)	3.45	$D_{32} = 119.2\ (\frac{FN^3\ 0.143}{\Delta P})$ Swirl plate Water $2\theta = 85^{o}$ FN 10-500 ΔP 5-100 psi	Collection cell
Darnell (107)	3.46	$D_{32} = 2400/\ P^{0.5}$	Collection cell
	3.47	$D_{32} = \exp\ (5.45 - 0.0054\ V_{RA})$ Grooved core insert Water FN 0.45-3 ΔP 5-1500 psi	

Tate and Marshall (98)	3.48	$D_{32} = 286\ (d_o + 0.17 \exp\ (\frac{13}{V_A} - 0.0094\ V_T)$ Grooved core insert Water V_T 7-50 ft sec^{-1} V_A 40-150 ft sec^{-1}	Collection cell
Turner and Moulton (108)	3.49	$\overline{D} = 16.56\ d_o^{1.52}\ Q^{-0.444}\ \sigma^{0.713}\ \mu^{0.159}$ Grooved core insert	Molten wax, particles suspended in mineral oil
	3.50	$\overline{D} = 41.4\ d_o^{1.589}\ Q^{-0.537}\ \sigma^{0.594}\ \mu^{0.22}$ Tangential entry $\log \overline{D} = \frac{\Sigma ND^3 \log D}{\Sigma ND^3}$ μ 0.81-2.02 cP ΔP 30-125 psi ρ 1.03-1.08 gcm^{-3} σ 27-37 dynes cm^{-1} Q 1.8-17.2 US gal sec^{-1} (3.49) Q 9-28 US gal sec^{-1} (3.50) napthol and benzoic acid	

Knight (109)	3.51	$D_{32} = \frac{220\ Q^{0.209}\ \nu_L^{0.215}}{P^{0.458}}$ Swirl plate P 0.746 g cm^{-3} ν 2-18.5 cS σ 22 dynes cm^{-1}	Substitute Liquid
Radcliffe (109)	3.52	$D_{32} = \frac{325\ Q^{0.318}}{\Delta P^{0.53}}$ Spill overflow type ΔP 6-125 psi FN 0.5-4.15 Mixtures of kerosene/oil	Stained paper
Tanasawa and Kobayasi (83)	3.53	$D_{32} = \text{const}\ (\frac{\sigma}{\Delta P})^{0.25}$ swirl insert ΔP 150-4400 psi FN 0.15-0.4 ν 0.01-4.05 σ 36-75 d cm^{-1}	Collection cell

Nelson and Stevens (100)	3.54	$Y = \log_{10} \frac{D_{v50}}{do}$ Grooved core insert where $Y = -0.0811\ X^2 + 0.124X - 0.186$ and $X = \log_{10} (R_e^{0.45} W_e^{0.55} (\frac{V_T}{V_A})^{1.2})$ organic liquids ΔP 100-1500 psi	Frozen in liquid nitrogen
	3.55	For water $Y = -0.144X^2 + 0.702X - 1.26$ $X = \log_{10} (R_e^{0.8} W_e^{0.2} (\frac{V_T}{V_A})^{1.2})$	
Kim and Saunders (110)	3.56	$D_{v50} = \frac{7670\ d_o^{0.33}}{V_A^{0.11} V_T^{0.40}}$	Collection cell
Dombrowski and Wolfsohn (99)	3.57	$D_{32} = \frac{3305\ Q^{0.33}}{V_s}$	Sauter light absorption technique
	3.58	$D_{32} = \frac{332\ Q^{0.33}}{P^{0.5}}$ ΔP 50-350 psi Q 1-724 gph Water	

Wang and Tien (111)	3.59	$Y = \log_{10} (\frac{D_{v50}}{d_o})$ where $Y = -0.6X + 1.4$ and $X = \log_{10}(R_e^{0.4} W_e^{0.52} A^{0.30})$ Grooved core insert aqueous polymer solutions, glycerin, water ΔP 100-1800 psi	Freezing in liquid nitrogen
Dombrowski and Tahir (112)	3.60	$D_{32} = 2774 \frac{Q^{0.248} \mu^{0.152}}{\rho^{0.499}}$	Flash photography
	3.61	$D_{32} = 3955 \frac{Q^{0.286}}{(2\theta)^{0.312} V_s^{0.918}}$ Lubricating oils ΔP 50-600 psi	

Chapter 4

Mathematical Model

This chapter is divided into two parts.

4.1 Development of the boundary layer equations and evaluation of the boundary layer thickness within the annulus of fluid discharging from the orifice.

4.2 Calculation of droplet sizes formed by the disintegration of the conical liquid sheet.

4.1 Statement of Simplified Problem

The swirling jet considered here is one in which the liquid enters the swirl chamber tangentially and then passes down a converging channel to emerge through an orifice of radius R_o. During passage a boundary layer is formed at the wall which increases in thickness in a direction towards the exit orifice. Taylor (89) first considered the problem of a swirling fluid passing down a converging core, but he simplified the problem by neglecting the axial component of velocity outside the boundary layer. His solution indicated that a substantial part of the outlet flow passed through the boundary layer. The fluid was assumed to flow under conditions of a free vortex, which implied that the fluid moved in a circular path with no torque applied. Thus the fluid moved with a velocity:

$$V_\theta = \Omega/r \tag{4.1}$$

in circles around the axis, where r is the distance from the axis and Ω is the circulation constant. The above assumption predicts that an air core will form at the orifice axis since equation (4.1) requires an infinite velocity at r = 0, and thus the spinning liquid cavitates. The liquid thus passes through the nozzle orifice as an annular ring. The circulation constant was estimated from the relation:

$$\Omega = \frac{Qr_m}{A_s} \tag{4.2}$$

where Q is the volumetric flowrate

A_s is the area of the inlet to the swirl chamber

r_m is the mean swirl radius at the inlet.

In the following treatment an attempt is made to predict the boundary layer thickness, and the distribution of velocity within it, taking account of the axial velocity component outside the boundary layer. Relationships are developed from the Navier-Stokes equations for Newtonian fluids. This is considered to be justified because the chalk slurries are shear thinning and since extremely large shear rates are encountered within the nozzle, the apparent viscosity under those conditions varies by a negligible amount.

Boundary Layer Equations

The full equations of motion for a Newtonian fluid, in terms of velocity gradients are, in cylindrical c-ordinates:

$$\rho\left(\frac{\partial v_r}{\partial t} + v_r\frac{\partial v_r}{\partial r} + \frac{v_\theta}{r}\frac{\partial v_r}{\partial \theta} - \frac{v\theta^2}{r} + v_z\frac{\partial v_r}{\partial z}\right) = -\frac{\partial P}{\partial r}$$

$$+ \mu\left[\frac{\partial}{\partial r}\left(\frac{1}{r}\frac{\partial}{\partial r}(rv_r)\right) + \frac{1}{r^2}\frac{\partial^2 v_r}{\partial \theta^2} - \frac{2}{r^2}\frac{\partial v_\theta}{\partial \theta} + \frac{\partial^2 v_r}{\partial z^2}\right]$$

$$+ \rho g_r \qquad (4.3)$$

$$\rho\left(\frac{\partial v_\theta}{\partial t} + v_r\frac{\partial v_\theta}{\partial r} + \frac{v_\theta}{r}\frac{\partial v_\theta}{\partial \theta} + \frac{v_r v_\theta}{r} + v_z\frac{\partial v_\theta}{\partial z}\right) = -\frac{1}{r}\frac{\partial P}{\partial \theta}$$

$$+ \mu\left[\frac{\partial}{\partial r}\left(\frac{1}{r}\frac{\partial}{\partial r}(rv_\theta)\right) + \frac{1}{r^2}\frac{\partial^2 v_\theta}{\partial \theta^2} + \frac{2}{r^2}\frac{\partial v_r}{\partial \theta} + \frac{\partial^2 v_\theta}{\partial z^2}\right] + \rho g_\theta$$

(4.4)

$$\rho\left(\frac{\partial v_z}{\partial z} + v_r\frac{\partial v_z}{\partial r} + \frac{v_\theta}{r}\frac{\partial v_z}{\partial \theta} + v_z\frac{\partial v_z}{\partial z}\right) = -\frac{\partial P}{\partial z}$$

$$+ \mu\left[\frac{1}{r}\frac{\partial}{\partial r}\left(\frac{r\partial v_z}{\partial r}\right) + \frac{1}{r^2}\frac{\partial^2 v_z}{\partial \theta^2} + \frac{\partial^2 v_z}{\partial z^2}\right] + \rho g_z \qquad (4.5)$$

The full equation of continuity:

$$\frac{\partial P}{\partial t} + \frac{1}{r}\frac{\partial}{\partial r}(\rho.r.v_r) + \frac{1}{r}\frac{\partial}{\partial \theta}(\rho v_\theta) + \frac{\partial}{\partial z}(\rho v_z) = 0 \qquad (4.6)$$

The co-ordinate system is shown in Figure 4.1.

In applying these equations to a fluid flowing symmetrically around the inside surface of a converging nozzle, it is assumed that:

(1) Steady state conditions exist

(2) The boundary layer is thin and variation in pressure through its thickness may be neglected.

(3) For axial symmetry all derivatives with respect to θ are zero.

(4) v_r is small and derivatives normal to the axis are much larger than derivatives parallel to the axis of the nozzle.

The simplified equations of motion can now be written:

$$v_r\cdot\frac{\partial v_r}{\partial r} - \frac{v_\theta^2}{r} + v_z\frac{\partial v_r}{\partial z} = \nu\left(\frac{\partial^2 v_r}{\partial r^2} + \frac{1}{r}\frac{\partial v_r}{\partial r} - \frac{v_r}{r^2}\right) \qquad (4.7)$$

$$v_r\frac{\partial v_\theta}{\partial r} + v_r\frac{v_\theta}{r} + v_z\frac{\partial v_\theta}{\partial z} = \nu\left(\frac{\partial^2 v_\theta}{\partial r^2} + \frac{1}{r}\frac{\partial v_\theta}{\partial r} - \frac{v_\theta}{r^2}\right) \qquad (4.8)$$

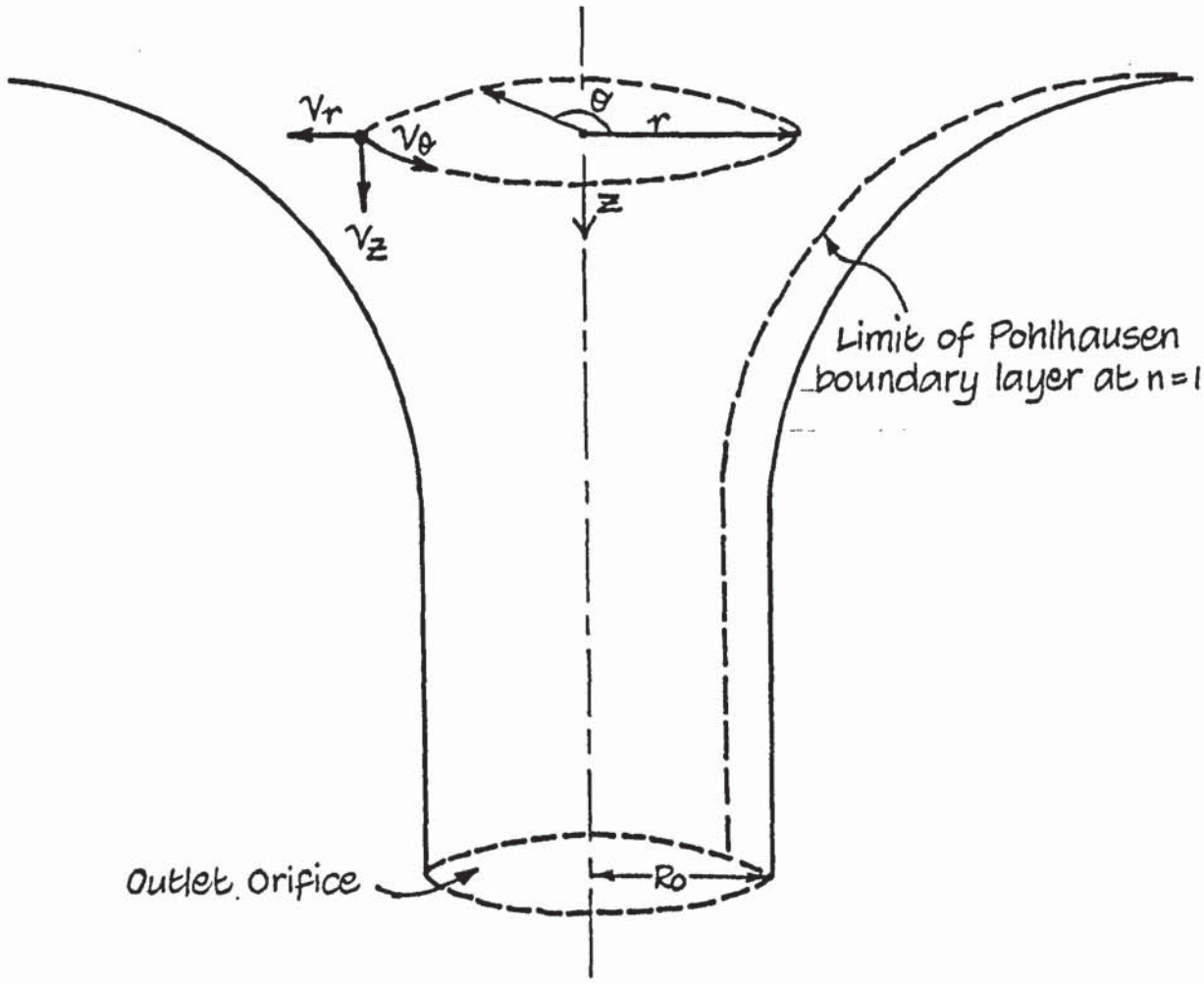

Figure 4.1 The Co-ordinate System.

$$v_r \cdot \frac{\partial v_z}{\partial r} + v_z \cdot \frac{\partial v_z}{\partial z} = - \frac{1}{\rho} \cdot \frac{\partial P}{\partial z} + \nu \left(\frac{1}{r} \cdot \frac{\partial v_z}{\partial r} + \frac{\partial^2 v_z}{\partial r^2} \right) \qquad (4.9)$$

and the equation of continuity

$$\frac{1}{r} \frac{\partial}{\partial r} (r \cdot v_r) + \frac{\partial v_z}{\partial z} = 0 \qquad (4.10)$$

A complete solution of the above equations seems unlikely and therefore Taylor successfully applied the approximate method of Pohlhausen to solve the boundary layer equations defining the flow of a fluid circulating round the inside of a conical surface with straight sides. Pohlhausen's method consists of assuming an arbitrary velocity distribution in the boundary layer which satisfies the boundary conditions at the wall and at the outside edge of the boundary layer.

Boundary Layer Momentum Integral

To obtain these integrals, the equations of motion are integrated through the boundary layer, which is assumed to have a definite thickness δ. Equation (4.7) is discarded since it consists mainly of small terms. Integrating (4.8)

$$\{v_r \cdot v_\theta\} - \int v_\theta \cdot \frac{\partial v_r}{\partial r} \, dr + \int \frac{v_r \cdot v_\theta}{r} \, dr + \int \frac{\partial}{\partial z} (v_\theta \cdot v_z) \, dr$$

$$- \int v_\theta \cdot \frac{\partial v_z}{\partial z} \, dr = \nu \left[\left\{ \frac{\partial v_\theta}{\partial r} \right\} + \left\{ \frac{v_\theta}{r} \right\} \right] \qquad (4.11)$$

By means of (4.10) the fifth term in (4.11) is transformed:

$$\int v_\theta \cdot \frac{\partial v_z}{\partial z}\, dr = -\int v_\theta \cdot \frac{\partial v_r}{\partial r}\, dr - \int \frac{v_r \cdot v_\theta}{r}\, dr$$

Thus (4.11) becomes

$$\{v_r \cdot v_\theta\} + 2\int \frac{v_r \cdot v_\theta}{r}\, dr + \int \frac{\partial}{\partial z}(v_\theta \cdot v_z)\, dr = \nu\left[\{\frac{\partial v_\theta}{\partial r}\} + \{\frac{v_\theta}{r}\}\right] \qquad (4.12)$$

Similarly (4.9) becomes

$$\{v_r \cdot v_z\} + \int \frac{\partial}{\partial z}(v_z^2)\, dr + \int \frac{v_r \cdot v_z}{r}\, dr = -\frac{1}{\rho}\int \frac{\partial P}{\partial z}\, dr + \nu\left[\{\frac{v_z}{r}\} + \{\frac{\partial v_z}{\partial r}\} + \int \frac{v_z}{r^2}\, dr\right] \qquad (4.13)$$

v_r may be eliminated from (4.12) and (4.13) by means of (4.10).

Application of the Pohlhausen Method

It is necessary to assume an arbitrary form for the distribution of velocity through the boundary layer.

Boundary Conditions

$$v_\theta = v_z = 0 \text{ at } r = R$$

$$v_\theta = \frac{\Omega}{R},\ v_z = W,\ \frac{\partial v_\theta}{\partial r} = \frac{\partial v_z}{\partial r} = 0 \text{ at } r = R-\delta$$

The following relations are the most simple power series expressions that satisfies the above boundary conditions.

$$v_z = W\ (2n-n^2) \tag{4.14}$$

where W is the streaming velocity outside the boundary layer and W = W(z) only.

$$v_\theta = \frac{\Omega}{R}\ (2n-n^2) \tag{4.15}$$

$$\text{where } n = \frac{R-r}{\delta} \tag{4.16}$$

so that n varies from 0 to 1.0 through the boundary layer. Two variable quantities, W and δ define the boundary layer at any point, and are functions of z only. They can therefore be determined by using the momentum integrals (4.12) and (4.13). Before applying (4.14) and (4.15), v_r must first be eliminated.

Integrating (4.10)

$$\{r.v_r\} = -\int r\ \frac{\partial v_z}{\partial z}\ dr \tag{4.17}$$

or in terms of n

$$\{(R-n\delta).v_r\} = \delta \int (R-n\delta)\ \frac{\partial v_z}{\partial z}\ dn \tag{4.18}$$

From (4.14)

$$\frac{\partial v_z}{\partial z} = W(2-2n)\ \frac{\partial n}{\partial z} + \frac{dw}{dz}\ (2n-n^2) \tag{4.19}$$

From (4.16)

$$\frac{\partial n}{\partial z} = \frac{1}{\delta}\ \frac{dR}{dz} - \frac{n}{\delta}\ \frac{d\delta}{dz} \tag{4.20}$$

So that (4.18) becomes:

$$\{(R-n\delta)\ v_r\} = \delta \int (R-n\delta) \left[\frac{dw}{dz} (2n-n^2) + W(2-2n)\left(\frac{1}{\delta} \frac{dR}{dz} - \frac{n}{\delta} \frac{d\delta}{dz} \right) \right] dn \qquad (4.21)$$

Integration of (4.21) yields v_r at any point n

$$v_r = \frac{\delta}{R-n\delta}\left[\frac{w}{\delta} \frac{dR}{dz} \left(2Rn-n^2(R+\delta)+\frac{2n^3\delta}{3}\right) - \frac{w}{\delta} \frac{d\delta}{dz}\left(Rn^2-\frac{2n^3}{3}(R+\delta) + \frac{n^4\delta}{2}\right) + \frac{dw}{dz}\left(Rn^2-\frac{n^3}{3}(R+2\delta) + \frac{n^4\delta}{4}\right)\right] \qquad (4.22)$$

Equation (4.13) contains the unknown quantity $\frac{1}{\rho} \int \frac{\partial P}{\partial z} dr$ and a suitable form for the axial pressure gradient must be assumed. Binnie and Hookings (116) developed an expression for the axial streaming velocity in a convergent nozzle and equating this velocity to W in (4.14) eliminates the need for two momentum integrals, since only one variable quantity, δ, remains. Equation (4.13) is therefore discarded and (4.12) used to determine δ. Evaluating each of the terms in (4.12) yields, after some reduction, the first order differential equation:

$$\frac{d\delta}{dz} = \frac{1}{R-\delta/12}\left[-\delta \frac{dR}{dz} - \frac{\delta R}{w} \frac{dw}{dz} + 15\frac{\nu}{w}\left(\frac{R}{\delta} - \frac{1}{2} \right) \right] \qquad (4.23)$$

A more detailed derivation of (4.23) is given in Appendix II.

A solution to (4.23) is obtained numerically by means of the Runge-Kutta 4th order integration technique.

Before applying this method, values for R, dR/dz,

w and dw/dz are required at each incremental value of z, over the length of the nozzle.

Evaluation of R, dR/dz

Consider the section through the converging inside surface of the nozzle represented in Figure 4.2. The surface is cut on an arc of radius r_1, so that it describes a quarter of a circle. Any point on this surface is represented, two dimensionally, by the equations:

$$y = r_1 \sin \phi \tag{4.24}$$

$$r_1 - x = r_1 \cos \phi \tag{4.25}$$

From the relation

$$\sin^2\phi + \cos^2\phi = 1$$

(4.24) and (4.25) may be combined

$$\frac{y^2}{r_1^2} + \frac{1}{r_1^2}(r_1-x)^2 = 1$$

or $$y^2 = r_1^2 - (r_1-x)^2 \tag{4.26}$$

Re-writing (4.26) in terms of the co-ordinate system of Figure 4.1,

$$R = r_1 + R_o - (2r_1.z-z^2)^{0.5} \tag{4.27}$$

So that, at a distance z down the nozzle, the wall radius R is defined. To find the rate of change of R

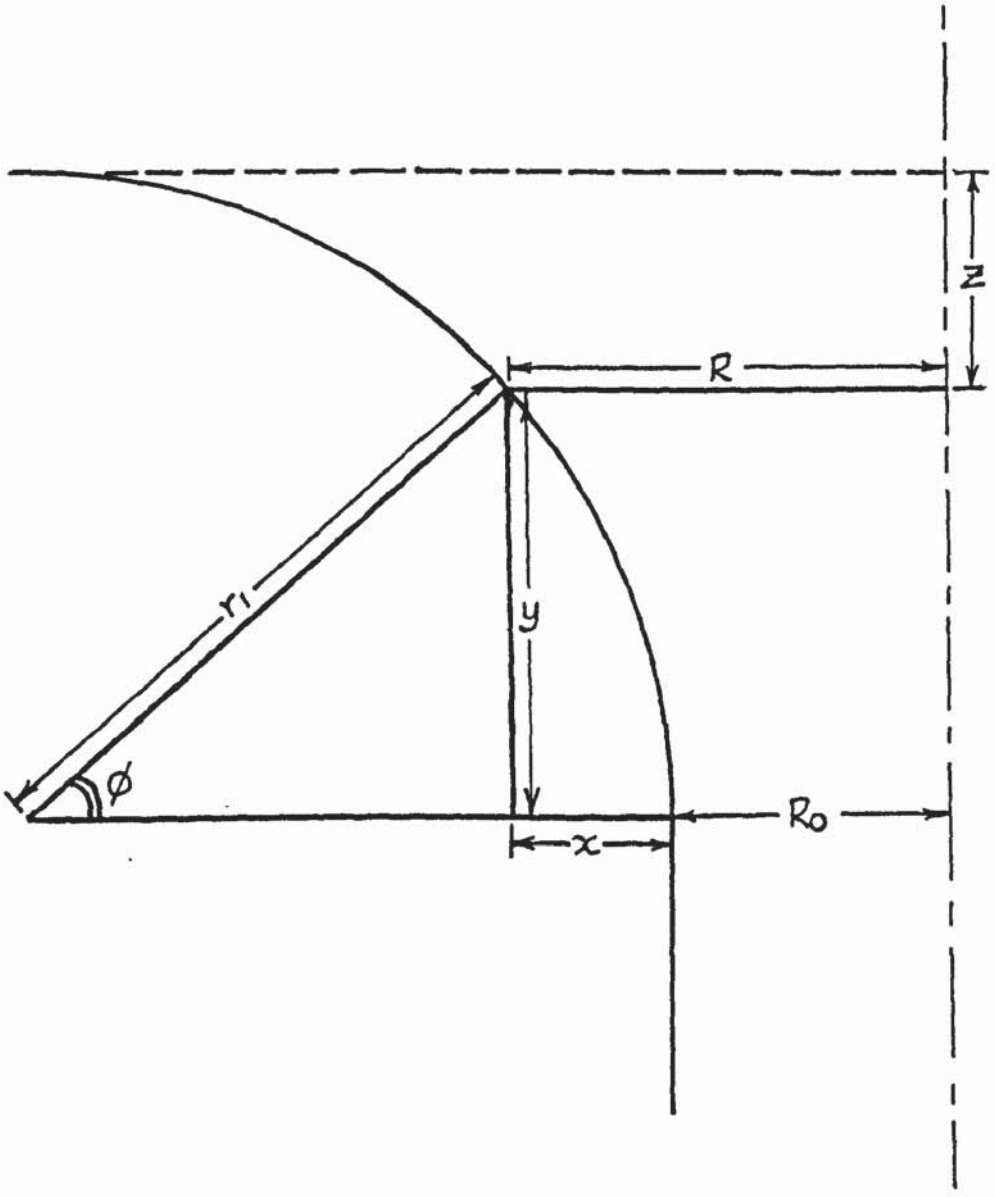

Figure 4.2. Section Through Nozzle.

with z equation (4.27) is differentiated with respect to z, thus

$$\frac{dR}{dz} = \frac{z-r_1}{(2r_1z-z^2)}^{0.5} \qquad (4.28)$$

which satisfies the boundary conditions

$$\frac{dR}{dz} = \infty \text{ at } z = 0, \quad \frac{dR}{dz} = 0 \text{ at } z = r_1$$

Inspection of the actual converging nozzle showed that it terminated in the form of an orifice insert and examination showed that the arc of the curvature did not complete 90^{o} so that, at $z = 0$, $^{dR}/_{dz}$ has a real value. This value was estimated by direct measurement.

Evaluation of W and dw/dz

Binnie and Hookings derived an expression for the discharge Q, of a swirling flow through a converging nozzle. They assumed the radial velocity to be negligible and applied Bernouilli's equation. For frictionless flow it follows that

$$h^1 + \frac{W^2+\Omega^2/r^2}{2g} = H^1 \qquad (4.29)$$

where h^1 and W are the pressure head and downward velocity at radius r, and H^1 is the total pressure head.

The variation of h^1 over the annular cross section was shown to be:

$$h^1 = \frac{\Omega^2}{2g}\left(\frac{1}{r_{AC}^2} - \frac{1}{r^2} \right) \qquad (4.30)$$

where r_{AC} is the radius of the air core.

Combination of (4.29) and (4.30) shows that W has a constant value over the cross section. In terms of the pressure drop, P, this is given by:

$$W = \left(\frac{2P}{\rho} - \frac{\Omega^2}{r_{AC}^2} \right)^{0.5} \qquad (4.31)$$

From a mass balance over the cross section the discharge Q is:

$$Q = \pi(R^2 - r_{AC}^2) \left(\frac{2P}{\rho} - \frac{\Omega^2}{r_{AC}^2}\right)^{0.5} \qquad (4.32)$$

For stability of flow r_{AC} must adjust itself so that the discharge is a maximum, and the condition $\partial Q / \partial r_{AC} = 0$ yields

$$r_{AC}^2 = \frac{\rho}{8P}\left[\Omega^2 + \left(\Omega^4 + 16R^2\Omega^2 \frac{P}{\rho}\right)^{0.5} \right] \qquad (4.33)$$

Applying this relationship over the annulus of the fluid, at any point along the nozzle, shows that the streaming velocity W may be evaluated from a mass balance.

$$W = \frac{Q}{\pi(R^2 - r_{AC}^2)} \qquad (4.34)$$

where R is the distance of the nozzle wall from the axis.

The streaming velocity W is thus evaluated as a function of the axial co-ordinate, z. Since the fluid

is flowing along the curved wall, the direction of flow and hence W is continually changing. W must therefore be resolved in the axial direction before applying it to equation (4.23).

To evaluate the axial velocity gradient, $^{dW}/_{dz}$ which is also required, equations (4.33) and (4.34) are differentiated with respect to z. On elimination of $\frac{dr_{AC}}{dz}$, equation (4.35) is obtained.

$$\frac{dW}{dz} = \frac{-Q}{\pi(R^2-r_{AC}^2)^2}\,2R\,\frac{dR}{dz}\left(1 - \frac{\Omega^2}{(\Omega^4+16R^2\Omega^2\frac{p}{\rho})^{0.5}}\right) \qquad (4.35)$$

A value for r_{AC} is obtained using (4.33)

Having established the forms of R, $\frac{dR}{dz}$, W and $\frac{dW}{dz}$, equation (4.23) is now integrated over the length of the nozzle to obtain the boundary layer thickness at the orifice.

Although (4.23) is a first order differential equation, its solution is not straightforward. The boundary condition $\delta = 0$ at $z = 0$ gives an infinite value for $\frac{d\delta}{dz}$ since δ appears in the denominator. A practical solution is achieved by assuming an extremely small value for δ to initiate the Runge Kutta integration subroutine, and applying similarly sized step lengths. Once initialised the system becomes stable and the step length may be greatly increased after completion of the first 5% of the integration length. The final value of δ proved insensitive to the assumed initial value.

The values used were selected to optimise computer time. This was confirmed by repeating the quadrature starting with different step lengths in the first 5% of the radius.

4.2 Prediction of Drop Sizes

Liquid is discharged from the nozzle in the form of a hollow cone possessing a velocity and direction dependant on the magnitude of the velocity components v_r, v_θ and v_z within the fluid emerging from the outlet orifice. The radial component, v_r is negligible when compared with v_θ and v_z and will therefore be ignored. The trajectory of the sheet is therefore a resultant of the components v_θ and v_z. The predicted semi-cone angle, θ_p, is now defined

$$\theta_p = \tan^{-1}\left(\frac{\overline{v_\theta}}{\overline{v_z}}\right) \tag{4.36}$$

where $\overline{v}$ denotes the mean velocity component averaged over the sheet thickness at the orifice. Each component is calculated from the equation

$$\overline{v} = \frac{\overline{v}_1 A_1 + \overline{v}_2 A_2}{A_1 + A_2} \tag{4.37}$$

The subscripts 1 and 2 refer to the regions inside and outside of the boundary layer respectively. A is the cross-sectional area. The velocity profiles are shown in Figure 4.3. The total flow area, A_1+A_2 is equal to the volumetric flowrate divided by the mean axial velocity.

$$A_T = \frac{Q}{\overline{v}_z} \tag{4.38}$$

The mean axial velocity within the boundary layer is

obtained by integrating (4.14) between the limits n = 0 and n = 1

$$\text{i.e. } \overline{v_{z_1}} = \int_0^1 W\,(2n-n^2)\,dn$$

so that $\overline{v_{z_1}} = \frac{2W}{3}$

Similarly for v_θ

$$\overline{v_{\theta_1}} = \int_0^1 \frac{\Omega}{R}\,(2n-n^2)\,dn$$

so that $\overline{v_{\theta_1}} = \frac{2\Omega}{3R}$

The mean axial velocity outside the boundary layer has already been defined; i.e.

$$\overline{v_{z_2}} = W$$

The boundary layer area, A_1 is defined by

$$A_1 = \pi(2R\delta-\delta^2)$$

and $A_2 = A_T - A_1$

The velocity profile of v_θ outside the boundary layer is that of a free vortex defined above by

$$v_\theta = \frac{\Omega}{r}$$

referring to Figure 4.3, the flow, V, within the element, δr is given by

$$\delta V = 2\pi r\,\delta r.\,V$$

$$\text{or} \quad V = \int_{r_{AC}}^{r_o} 2\pi r\,\frac{\Omega}{r}\,dr$$

so that $V = 2\pi\Omega(r_o - r_{AC})$

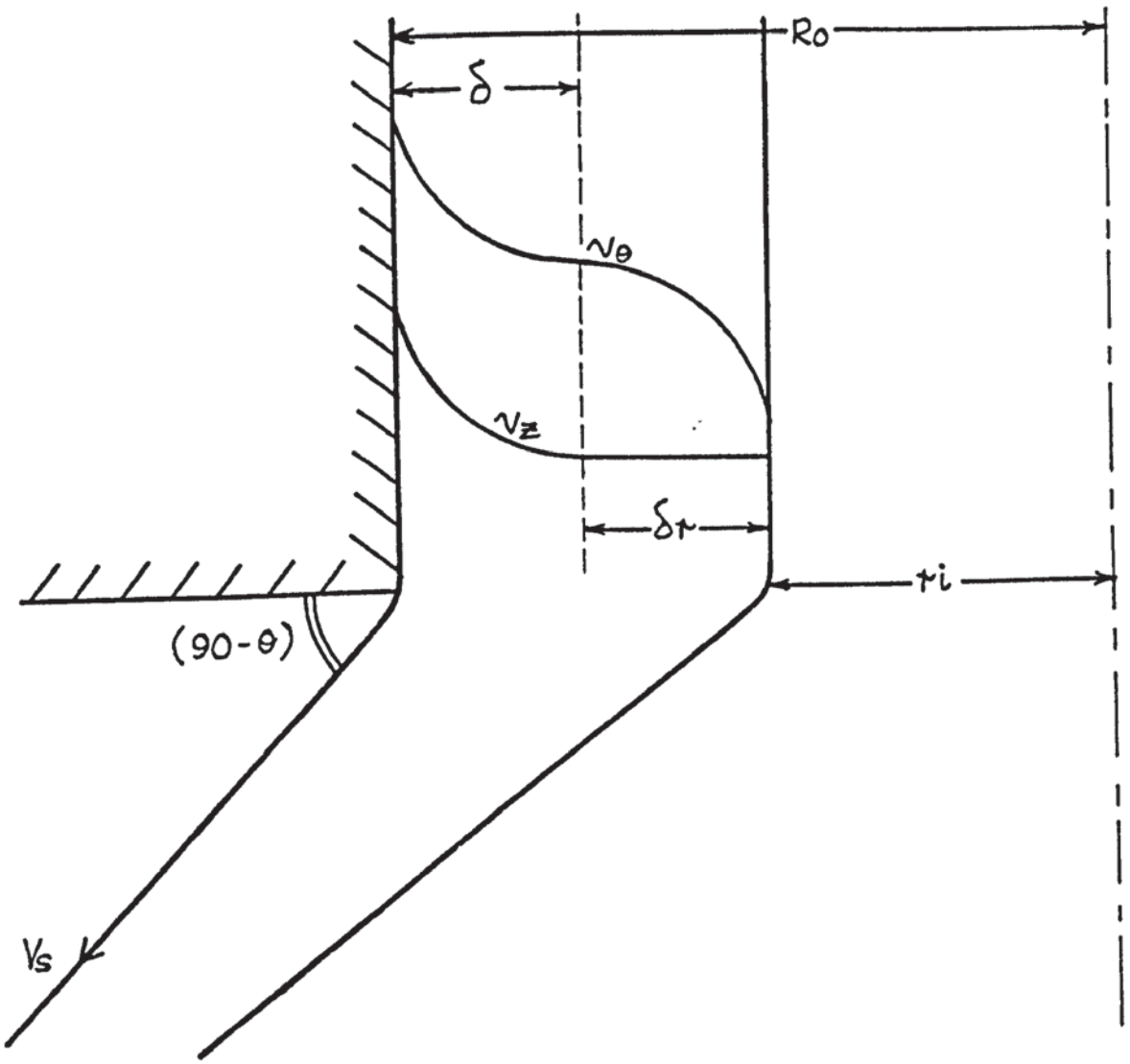

Figure 4.3. The Velocity Configuration at Outlet Orifice.

The mean velocity is thus V divided by the cross-sectional area:

$$\bar{v}_{\theta_2} = \frac{V}{\pi(r_o^2 - r_{AC}^2)}$$

$$\text{or } \bar{v}_{\theta_2} = \frac{2\Omega}{r_o + r_{AC}}$$

$$\text{and } r_o = R_o - \delta$$

$$\text{Now } A_T = \frac{Q}{\bar{V}_z} = \pi(R_o^2 - r_{AC}^2)$$

$$\text{so that } r_{AC} = \left(R_o^2 - \frac{Q}{\pi \bar{V}_z} \right)^{0.5}$$

The mean axial and swirling velocities are obtained by applying equation (4.37) and thus the cone angle is obtained from (4.36). In practise the edges of the conical sheet describe an arc as the cone moves through the ambient atmosphere. Thus at a point only a short distance downstream, the effective cone angle will have been reduced. Measurement of the cone angle could not be made directly at the orifice so that the experimental results will always be less than those predicted by equation (4.36). An empirical correlation for the spray angle is thus favoured. A dimensional analysis performed on those variables considered relative, yields the following analysis.

$$\theta_m = K \left(\frac{d_o \bar{v}_z \rho}{\mu} \right)^a \left(\frac{d_o \bar{v}_z^2 \rho}{\sigma} \right)^b \left(\frac{\Omega}{g} \right)^c \theta_p \qquad (4.39)$$

where d_o is the orifice diameter

g is gravity

and the physical properties of the liquid are:

ρ :- density

σ :- surface tension

μ :- viscosity

The constants in equation (4.39) were evaluated using a regression analysis. A correlation coefficient of 0.91 was obtained and the final form of the spray angle correlation is

$$\theta = 3.235 \left(\frac{d_o \bar{v}_z \rho}{\mu}\right)^{.027} \left(\frac{d_o \bar{v}_z \rho}{\sigma}\right)^{-.05} \left(\frac{\Omega}{g}\right)^{.2} \theta_p^{.872} \qquad (4.40)$$

The fit of the experimental data is illustrated in Figure 4.4. Having calculated the cone angle, the sheet velocity is obtained by resolving the mean axial velocity:

$$V_s = \frac{\bar{V}_z}{\cos\theta} \qquad (4.41)$$

Sheet Disintegration

The conical sheet of liquid discharged from the nozzle must, by the conservation of mass, reduce in thickness since the velocity in the sheet remains constant. Sinusoidal waves grow on the surface and increase in amplitude until they finally cause the sheet to break up. Dombrowski and Johns (40) postulate that the most rapidly growing wave is detached from the

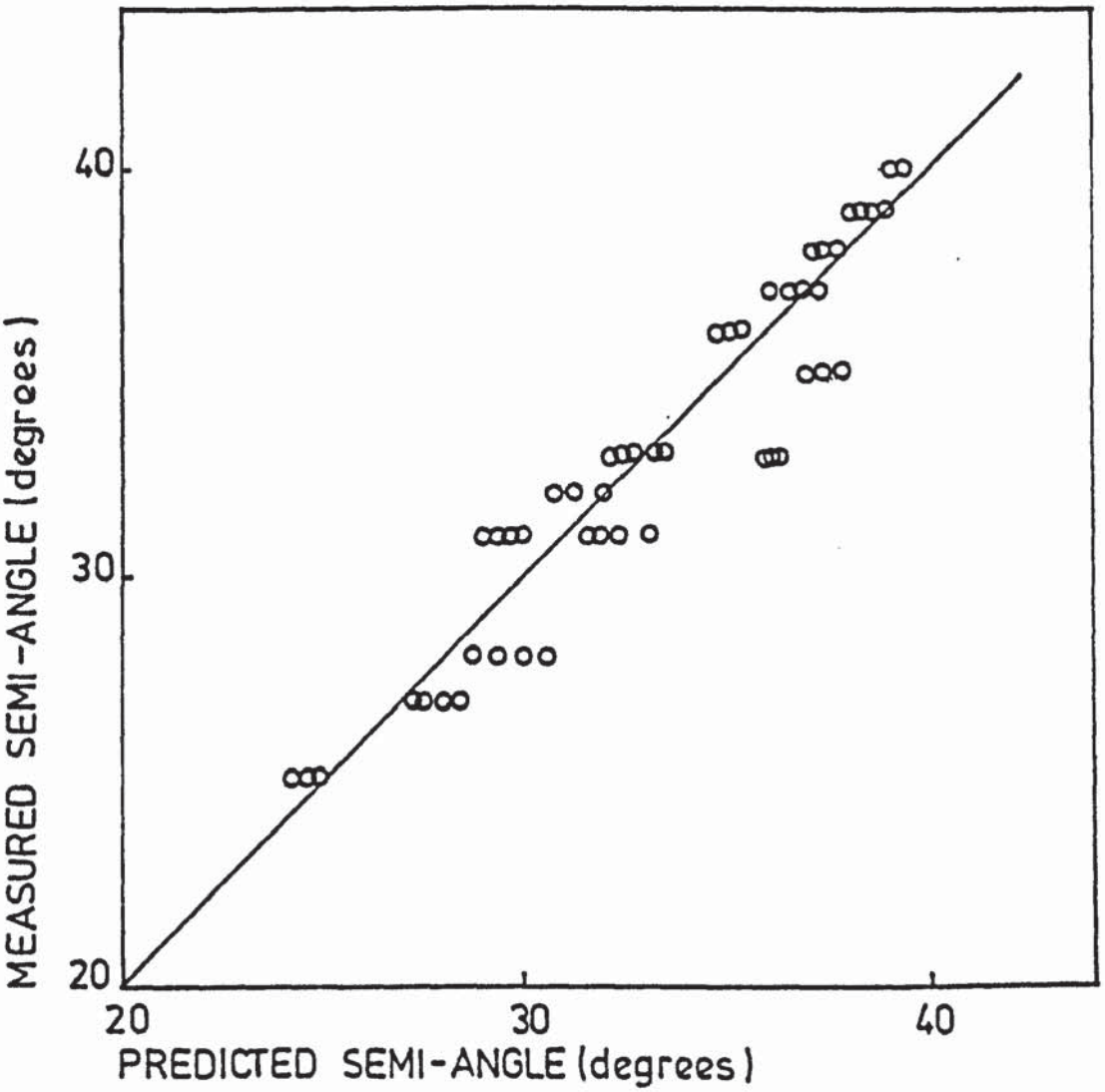

FIGURE 4.4 CORRELATION OF CONE SEMI-ANGLE MEASUREMENTS

sheet in the form of a ribbon half a wavelength wide. This ribbon contracts into an unstable ligament of diameter, d_L, under the action of surface tension and its diameter is calculated from a mass balance.

$$\frac{\pi d_L^2}{4} = h. \frac{\lambda}{2} \qquad (4.42)$$

or $d_L = \left(\frac{4h}{\eta}\right)^{0.5}$ where η is the wave number $= \frac{2\pi}{\lambda}$

h is the sheet thickness at the point of break-up and λ, the wavelength of disintegrating disturbance. The value of λ has been calculated by several workers. Squire (37) assumed the sheet to be inviscid and for constant sheet thickness obtained

$$\lambda = \frac{4\pi\sigma}{\rho_a V_s^2} \qquad (4.43)$$

valid for $\eta h < 0.25$.

where ρ_a is the ambient air density.

A later analysis by Dombrowski and Hooper (30) considered the practical case of an attenuating sheet. A similar equation was obtained, differing only in the magnitude of the constant. This equation however, is only valid when $\eta h > 1.5$ and is in the region where dilational waves predominate.

More recently Weihs (46) analysed the stability of thin viscous sheets, where relationships for unstable waves as a function of fluid viscosity, surface tension,

sheet velocity and distance from the nozzle were obtained. However, when applying data from this study to the model of Weihs, wavelengths very similar to those quoted in Squire's model were obtained. Prediction of ligament diameters in this study are therefore based on the simple inviseid model of Squire.

$$d_L = \frac{8h\sigma}{\rho_a V_s^2} \qquad (4.44)$$

where h is the sheet thickness at the point of disintegration.

This parameter is determined from individual measurements of flowrate, sheet velocity, cone angle and sheet length. Due to large fluctuations in measurements of the sheet length, results for each particular set of conditions were averaged and a correlation proposed. This finding agrees with that reported by Wolfsohn (117).

h is defined;

$$h = \frac{Q}{2\pi V_s \sin\theta . L} \qquad (4.45)$$

where L is the sheet length.

Correlation for Sheet Length

The intact sheet length, L, is considered to be a function of several variable quantities.

V_s - the sheet velocity

d_o - orifice diameter

θ - cone angle (correlated)

P - atomising pressure

ρ - density of fluid

μ - viscosity of fluid

σ - surface tension of fluid

i.e. $L = f(V_s, d_o, \theta, P, \rho, \mu, \theta)$

A dimensional analysis yields

$$\frac{L}{d_o} = K \left(\frac{d_o V_s \rho}{\mu}\right)^a \left(\frac{d_o V_s^2 \rho}{\theta}\right)^b \left(\frac{P}{\rho V_s^2}\right)^c \theta^d \qquad (4.46)$$

Values for the constants K, a, b, c, d were obtained from a regression analysis of 80 sets of data. The final form for the sheet length correlation is,

$$L = 1871.35.\ d_o.\ (Re)^{-0.117}.\ (We)^{-0.449}.\ (D_G)^{-0.934}.\ \theta^{-0.434} \qquad (4.47)$$

where Re is the Reynolds Number based on orifice

We is the Weber Number

and D_G is the other dimensionless group.

A correlation coefficient of 0.9 was obtained. The fit of the data is illustrated in Figure 4.5.

Formation of Drops from Ligaments

Since adopting the inviscid model of Squire, the role of viscosity in the formation of drops from ligaments will be neglected here. Instead the classical theory of Rayleigh will be employed. Briefly, his theory states

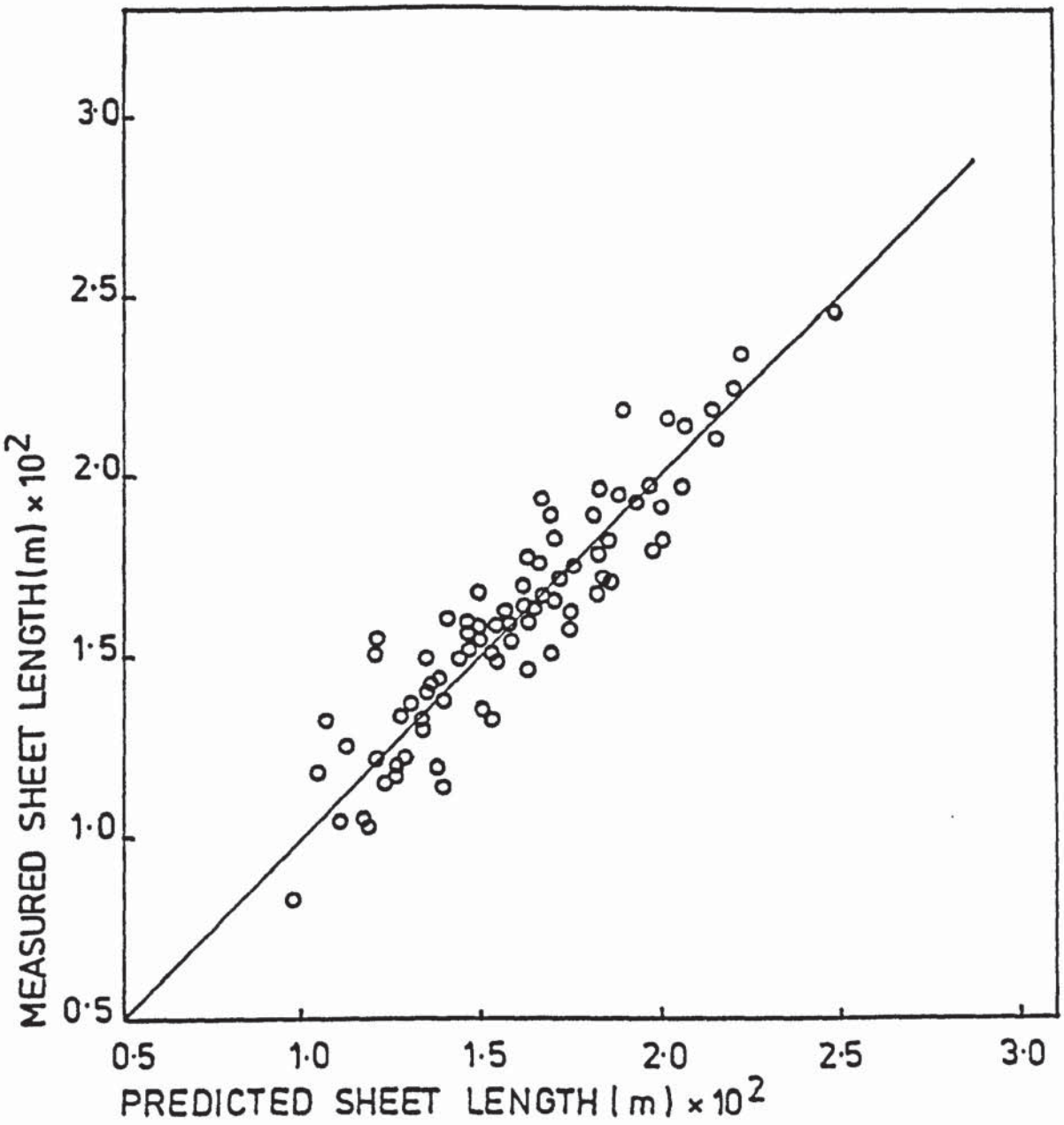

FIGURE 4:5 CORRELATION OF SHEET BREAK-UP LENGTH MEASUREMENTS

that the ligament swells and contracts symmetrically so that for each wavelength formed, one drop is produced although in practise satellite droplets are also formed. His solution for the most rapidly growing disturbance was

$$\lambda = 4.508\ d_L \qquad (4.48)$$

and the size of each droplet is obtained from a mass balance as,

$$D = 1.89\ d_L \qquad (4.49)$$

Ligament collapse captured by flash photography in this work, exhibited the Rayleigh type of break up.

The complete mathematical model is incorporated in one computer program, a listing of which is given in Figure 4.6.

FIGURE 4.6

Computer Program Listing of Mathematical Model

```
10  DIM T(5),N(5)
20  REM OPERATING PARAMETERS
30  REM R2=ORIFICE RADIUS
40  REM Z1=FACTOR FOR CALCULATION OF INITIAL DR/DZ
50  REM A2=AREA OF INLET TO SWIRL CHAMBER
60  REM P1=SLURRY DENSITY
70  REM S=SLURRY VISCOSITY
80  REM S3=SURFACE TENSION (CONSTANT)
90  REM Q=MASS FLOWRATE
100 REM P3=OPERATING PRESSURE
110 REM R5=SWIRL CHAMBER RADIUS
120 REM A=RADIUS OF CURVATURE OF NOZZLE WALL
130 FOR K=1 TO 4
140 READ R2,Z1,A2
150 PRINT "NOZZLE DIA"2*R2
160 FOR J=1 TO 5
170 READ P1,S
180 PRINT "SLURRY"P1
190 S=S/P1
200 FOR I=1 TO 4
210 READ Q,P3
220 P2=3.14159
230 A=.002108
240 R5=.0045
250 S3=.0729
260 Q=Q/P1
270 P3=P3*6895
280 PRINT
290 GOSUB 1290
300 X=X0
310 REM M=CIRCULATION CONSTANT
320 M=R5*Q/A2
330 Z=Z0
340 IF Z>A THEN 420
350 REM
360 REM CALCULATION OF DR/DZ (G1)
370 REM
380 S1=SQR(2*A*Z-Z↑2)
390 R=A+R2-S1
400 G1=(Z-A)/S1
410 GOTO 470
420 R=R2
430 G1=0
440 REM
450 REM CALCULATION OF STREAMING VELOCITY(W) AND DW/DZ (W1)
460 REM
470 N1=SQR(M↑4+16*R↑2*P3/P1*M↑2)
480 N2=P1/(8*P3)*(M↑2+N1)
```

```
490 W=Q/(P2*(R↑2-N2))
500 REM MODIFYING W TO ITS Z COMPONENT
510 W=W*S1/A
520 REM
530 W1=-Q/P2*2*R*G1*(1-M↑2/N1)/(R↑2-N2)↑2
540 REM
550 REM DIFFERENTIAL EQUATION REPRESENTING
560 REM GROWTH OF BOUNDARY LAYER
570 D=1/(R-X/12)*(-X*G1-X*R/W*W1+S/W*(15*R/X-7.5))
580 GOSUB T1 OF 1350,1400,1440,1490
590 IF Z >= F THEN 610
600 GOTO 340
610 PRINT "B/LAYER AT ORIFICE IS"X"M"
620 A1=P2*(R2↑2-(R2-X)↑2)
630 IF A1>3*Q/(2*W) THEN 680
640 GOTO 700
650 REM
660 REM CALCULATION OF MEAN VELOCITY (V1)
670 REM
680 V1=2*W/3
690 GOTO 710
700 V1=Q*W/(Q+W/3*A1)
710 PRINT "% FLOW THRO B/LAYER-"A1*V1/Q*100
720 GOSUB 1010
730 W=V1/COS((T(1))
740 PRINT "SHEET VEL"W
750 N1=2*R2*W/S
760 N2=2*R2*P1*W↑2/S3
770 N3=P3/(P1*W↑2)
780 N4=T(1)
790 REM
800 REM CORRELATION FOR SHEET LENGTH
810 REM
820 L=3743.7*R2/N1↑.117/N2↑.449/N3↑.934/N4↑.434
830 PRINT "PREDICTED SHEET LENGTH"L"M"
840 GOSUB 920
850 NEXT I
860 NEXT J
870 NEXT K
880 REM
890 REM H1=SHEET THICKNESS AT BREAKUP POINT
900 REM N=INSTABILITY NUMBER
910 REM
920 H1=Q/(2*P2*W*L*SIN(T(1)))
930 N=1.206/.1458*W↑2
940 PRINT "CONE ANGLE"T(1)*180/P2
950 REM PREDICTION OF MEAN DROP SIZE (D1)
960 D1=1.89*SQR(4*H1/N)
970 PRINT "PREDICTED DROP SIZE"D1"MICRONS"
980 IF K=4 AND J=4 THEN 1580
990 RETURN
```

```
1000 REM
1010 REM CALCULATION OF CONE ANGLE
1020 REM
1030 REM A1=AREA OF BOUNDARY LAYER
1040 REM A3=AREA OF STREAM OUTSIDE BOUNDARY LAYER
1050 REM R1=RADIUS OF AIR CORE
1060 REM V2=MEAN SWIRLING VELOCITY AT ORIFICE
1070 IF A1 <= Q/V1 THEN 1120
1080 A3=Q/V1-A1
1090 R1=SQR(R2↑2-Q/(P2*V1))
1100 V2=M*V1/Q*(2*A1/(3*R2)+2*A3/(R2-X+R1))
1110 GOTO 1160
1120 V2=2/3*M/R2
1130 REM
1140 REM T(2)=PREDICTED CONE ANGLE
1150 REM
1160 T(2)=ATN(V2/V1)
1170 N(1)=2*R2*V1/S
1180 N(2)=2*R2*P1*V1↑2/S3
1190 N(3)=M/9.81
1200 REM CORRELATION FOR CONE ANGLE
1210 T(1)=3.235*N(1)↑.0271*N(3)↑.2*T(2)↑.8723/N(2)↑.0502
1220 REM
1230 RETURN
1240 REM INTEGRATION SUBROUTINE
1250 REM RUNGE KUTTA 4TH ORDER
1260 REM F=FINAL VALUE OF Z
1270 REM H=STEP LENGTH
1280 REM XO=INITIAL VALUE FOR B/LAYER THICKNESS
1290 T1=1
1300 F=.003175
1310 H=.000001
1320 XO=.000005
1330 ZO=Z1
1340 RETURN
1350 K1=H*D
1360 Z=ZO+H/2
1370 X=XO+K1/2
1380 T1=2
1390 RETURN
1400 K2=H*D
1410 X=XO+K2/2
1420 T1=3
1430 RETURN
1440 K2=H*D
1450 X=XO+K3
1460 Z=ZO+H
1470 T1=4
1480 RETURN
1490 K4=H*D
1500 X=XO+1/6*(K1+2*K2+2*K3+K4)
1510 ZO=ZO+H
1520 XO=X
1530 T1=1
1540 IF Z>F/20 THEN 1560
1550 RETURN
1560 H=.0001
1570 RETURN
1580 STOP
```

Chapter 5

Experimental Work

Experimental Equipment

The main objective of this research study was to examine the atomising characteristics of a particulate slurry. A range of calcium carbonate slurries were selected and atomised at various pressures using four Delavan SDX swirl atomisers, details of which are given in Table 5.1.

Experimental observations were made using a 1.5 m diameter spray tower constructed from perspex to permit photography. The layout of the experimental rig is illustrated in Figure 5.1. Slurry was transferred to the centrally located nozzle by means of a Marshall mono-pump coupled to a variable speed -V- belt drive assembly.

The slurry make-up tank was positioned directly above the pump inlet to ease slurry feeding problems. A suitable screen was positioned at the pump outlet to prevent any debris reaching the nozzle thereby minimising blockages. Atomising pressure was controlled by throttling back the needle valve in the recycle line to the feed tank. Line pressure was monitored on a pressure gauge situated adjacent to the nozzle. A mains water supply was provided to flush out the system and prevent solid deposition when shutting down. Control of slurry formulation was achieved by monitoring specific gravity measurements on samples taken from the recycle stream.

NOZZLE CODE	ORIFICE DIAMETER (m) $x10^3$	AREA OF INLET CHANNEL (m^2) $\times 10^6$	DIAMETER OF CONVERGING PART OF NOZZLE (m) $\times 10^3$
SC	0.96	3.60	4.25
SD	1.42	4.50	4.57
SE	1.78	5.85	5.39
SF	2.26	8.40	7.37

TABLE 5.1. Nozzle Dimensions

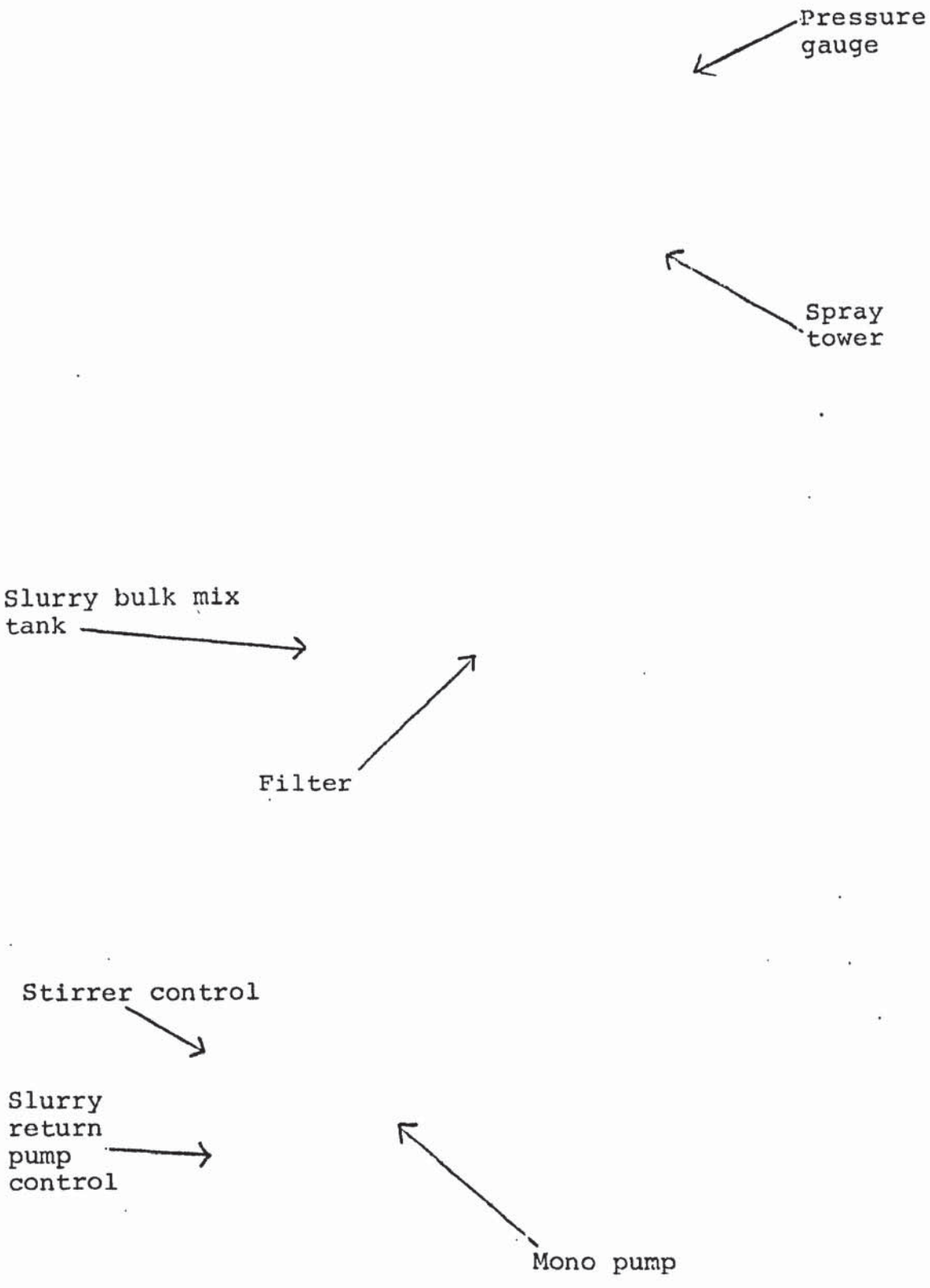

Figure 5.1. Layout of Experimental Rig

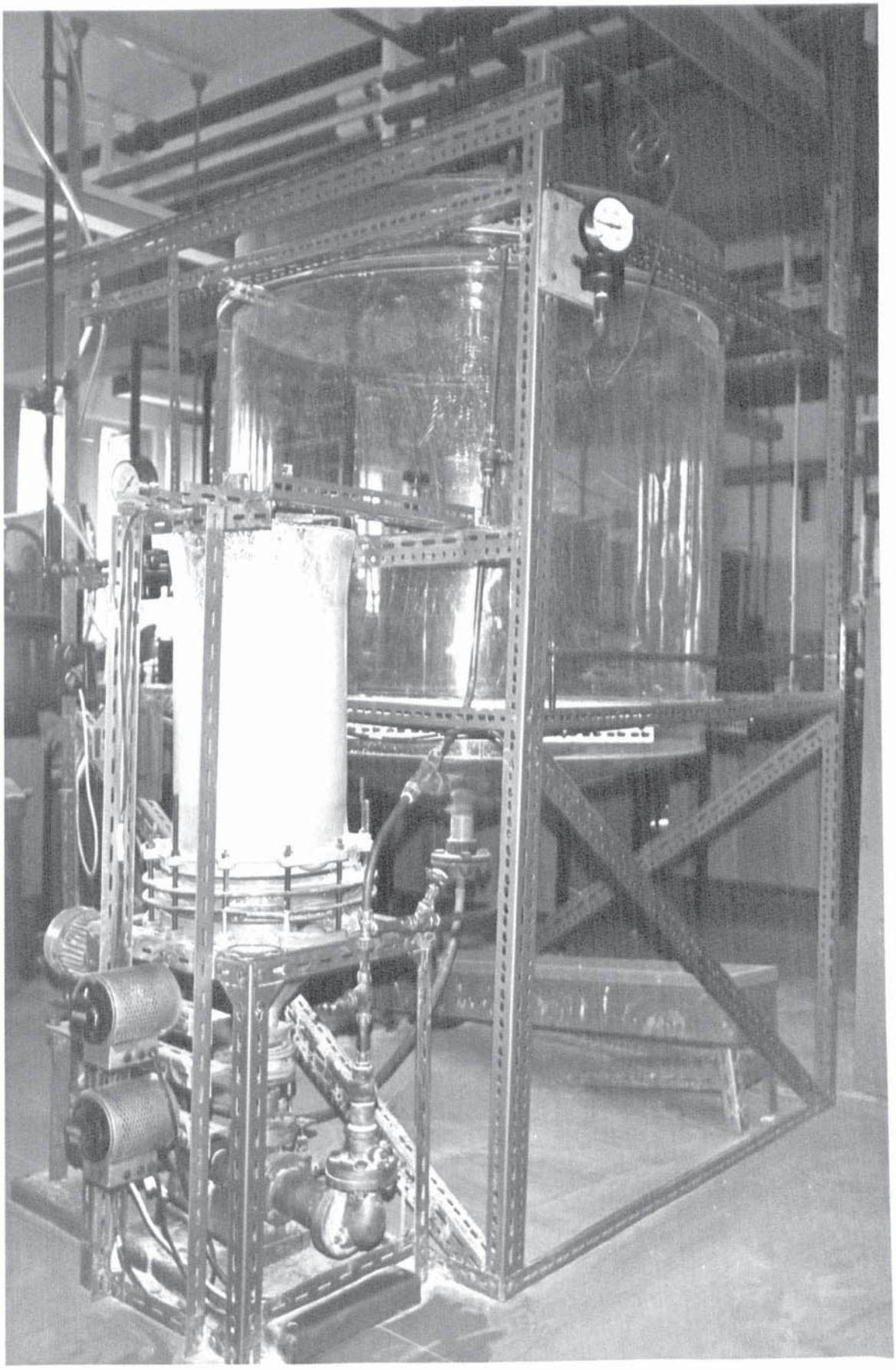

Range of Variables

Table 5.1 lists the nozzles employed. Slurries were sprayed at ejection pressures of 583, 690, 896, 1103 kN m^{-2}. Five slurry formulations were used (see Table 5.2) varying up to 50% w/w. The Rheological properties of each slurry were determined using a concentric cylinder viscometer. Relationships of apparent viscosity versus shear rate are presented in Figures 5.2 and 5.3.

Techniques for Drop Size Measurement

The method used to determine drop sizes is a very important factor in any experimental work and different results can be obtained using several of the accepted techniques. The importance of always considering the measuring technique when comparing experimental work was shown by Hasson and Mizrahi (118) who compared two techniques and showed that the values had approximately 30% consistent differences. Measurements are complicated by the large numbers of drops present travelling at high speeds. The available techniques revealed in a literature search, have been grouped into several broad categories and are discussed below.

Droplet Collection Methods

In these methods part or all of the spray is collected and the size determined. It is usually

Solids Concentration (% w/w)	Slurry Density (kgm^{-3})
23	1165
35	1265
40	1330
45	1380
50	1429

Table 5.2. Chalk Slurry Formulations

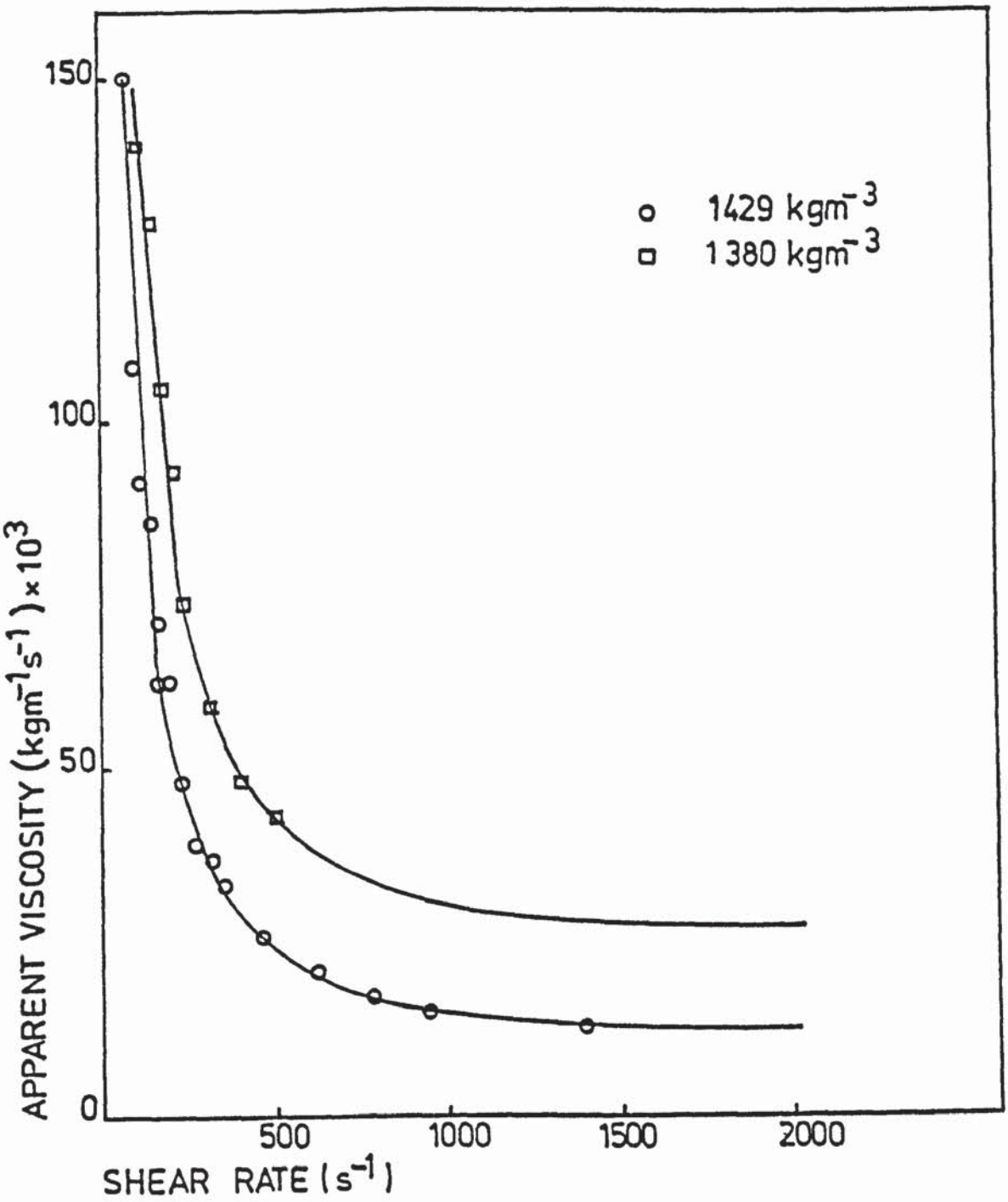

FIGURE 5.2 VARIATION OF APPARENT SLURRY VISCOSITY WITH SHEAR RATE

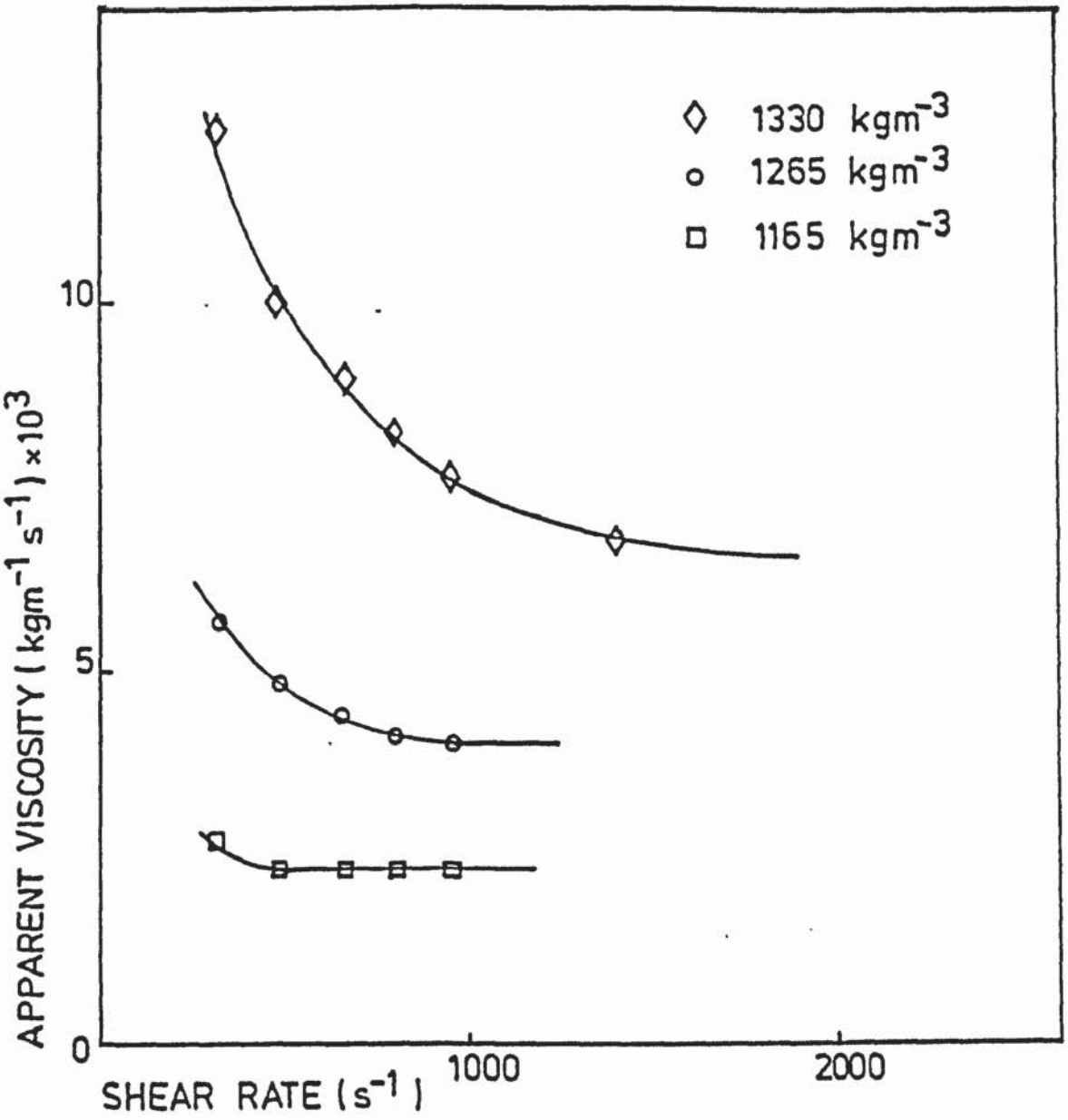

FIGURE 5.3 VARIATION OF APPARENT SLURRY VISCOSITY WITH SHEAR RATE

necessary to carry out the sizing some time after the operation, so it is important that the samples are stable. The main criticism of all of these methods is that the sampling interferes with the spray and introduces the question of whether the sample is representative of the entire drop population.

Many of the earlier techniques utilised glass slides or plates coated with various materials such as soot, oil, grease, soap and magnesium oxide. Droplets which impinge on this coated surface produced an impression or crater which must then be correlated with the true drop diameter after applying certain correction factors. Those slides coated with oil captured and preserved water droplets intact. Another disadvantage with these techniques is the tendency for small drops to follow the streamlines around the edge of the slide instead of impacting onto the slide.

Collection cells were later developed which contained an immersion fluid which was immiscible with the sampled drops. One system (98) used Stoddard solvent for sprayed water drops which contained black nigrosine dye. The solvent of low density permitted the droplets to sink to the bottom of the collection cell and the contrasting field presented ideal conditions for high magnification photography. A definite limitation of this technique is the tendency for large or high velocity droplets to shatter on impact.

Further techniques included the capture of drops on fine wire, thread or treated nylon screen.

All the above techniques require some method of sizing the collected drops. A simpler method is to visually inspect sampling slides or cells with the aid of a microscope and a calibrated eye piece. Various automatic counting aids have been developed. The most widely used is that of Zeiss, in which an adjustable iris is manually aligned with the droplet image and then activated to record a count within a particular size range. An electronic device capable of analysing several thousand droplets was developed in conjunction with the immersion sampling technique described above. A light beam scanning the images at narrow size intervals generated electrical pulses which were sized and counted automatically.

Droplet Freezing or Cooling

In any cell or slide sampling technique only a fraction of the total spray pattern can be covered. Since droplet size varies within the pattern this technique is not representative of the entire spray unless samples are weighted with respect to the sampling position. This problem may be averted by collecting the entire drop population within a certain time interval. To achieve this, a means must be devised for

preventing the droplets from coalescing. This can be achieved by freezing or cooling the drops as they are collected.

In one technique (103), fuel oil drops were introduced into a bath of cold alcohol which froze them into solid spheres. The frozen particles could then be sized by sieve analysis. A later variation of this technique (119) used hexane cooled with dry ice for collection of water drops. The particles collected at the top of the hexane bath were simultaneously released and allowed to sink through the bath into a submerged scale pan which recorded progressive weight increase. The rate of weight increase was correlated according to Stokes Law to yield the percentage of particles within a given size range.

Another method (94) utilises a substitute liquid of molten wax, which is sprayed while hot and the particles allowed to cool and solidify. The solid particles thus have the same size as the initial drops and a sieve analysis yields the drop sizes. Joyce perfected this method in a study where hot paraffin wax was used to represent fuel oil data. Accurate measurement of the wax temperature was necessary in order to determine its viscosity which was thought to greatly influence the degree of atomisation. Tate (120) reports that this technique is widely used in many research programmes.

To provide instantaneous freezing, liquid nitrogen at -200°C has been used as the collection medium. In the work of Choudbury (121) the sample fluids were sprayed directly into the liquid nitrogen and the screening of the frozen particles accomplished in a cold room. Nelson and Stevens (100) modified his technique by screening within an insulated sieve container mounted on a shaker. This method offers the advantage of elimination of sampling errors by collecting the whole spray. However it has the disadvantage of being expensive and makes the experiments more difficult to control, especially with regard to air density.

Gretzinger and Marshall (7) evolved a technique of a solids balance from the droplet to the dried particles. In a study of pneumatic atomisation an aqueous dye solution was sprayed and water evaporated from the droplets. The resultant dye aerosol was collected in mineral oil and the dry particles were counted to find the number distribution. The mass distribution of the original spray was then calculated by using a relationship developed for an individual drop.

They considered a liquid drop of diameter D_L containing C gm/ml of dye, and a dried drop of diameter D_s and density ρ_s. Since the mass of solid remains constant during drying, a solids balance was written thus:

$$D_L^3 . \rho . C = D_s^3 . \rho_s$$

or $$D_L = D_s \left(\frac{\rho_s}{\rho . C}\right)^{1/3}$$

This method suffers from the disadvantage of the unknown behaviour of a liquid droplet which may shrink or expand according to the drying mechanism.

Methods Based on Intertial or Velocity Differences

In this category the cascade impactor is most significant. It consists of a series of plates mounted perpendicular to a gas stream carrying the droplets. Large drops of high momentum collide with a plate whilst smaller drops are swept around it. The percentage of drops of a given diameter which impact on the plate can be calculated from the carrier gas velocity and size and location of the plate. Varying these parameters in successive stages results in the impaction of progressively smaller droplets at each subsequent stage. The quantity of liquid collected at each stage is then measured.

Various impactors have been developed with numbers of stages reaching six or more, thus classifying the droplets into narrower size ranges. The major disadvantage in this technique is that the upper limit of drop size which can be handled is about 170 microns, whilst in many atomisation processes, droplets range up to 400 microns.

Another method is based upon the variation in droplet momentum within a hollow cone spray (122). Large drops were considered to move towards the outside of the cone whilst the smaller drops move inwards. Thus a series of concentric annular collection trays placed beneath the spray were used to correlate the volume of liquid collected in each section with the drop size distribution.

High Speed Photography

The major difficulty with all the preceding methods is that the measuring technique interferes with the spray and may affect or incorrectly interpret the true drop size distribution. This difficulty is overcome by high speed photographic techniques where droplet motion is stopped and images are recorded for subsequent counting or analysis.

The direct measurement of drops from the photographs is complicated by the velocity distribution in the spray. Air drag creates a relative velocity between drops of different sizes, and the spatial distribution from a single photograph may be considerably different from that actually produced.

A technique employed to overcome this phenomena consists in taking double exposure photographs to determine drop velocities. The apparent spatial distribution is converted to the true temporal

distribution by multiplying the number of droplets of any given size by the drop velocity for that size. However this method assumes the drops to be moving in a continuous stream; which is not the case in atomisation. Clark and Dombrowski (123) proposed that since bands of drops are formed periodically it would be incorrect to weight the drop count. A true distribution would only be obtained when the drops are moving at their terminal velocities. While considerable errors may arise from un-weighted distributions taken some distance from the nozzle, very accurate results could be obtained near the region of disintegration where all droplets are substantially moving at the same velocity.

Other problems in photographic techniques are illumination and depth of field. Although depth of field must be reasonably narrow to permit precise determination of image magnification, very few droplets are liable to fall within the field if too narrow. There is the added difficulty of blurring of images outside the field of focus, and the question of whether or not they should be counted. There is a tendency to count large droplets over a greater depth of field than would be covered when counting smaller droplets.

De Corso (120) attacked this problem by observing Fresnel diffraction rings around the droplet images, accented by the use of monochromatic light together

with orthochromatic film. The width of the diffraction ring was correlated with the position of the droplet in the field of focus. Thus from the appearance of the rings, the image could either be rejected or counted.

Electronic scanning methods have been developed which are capable of rapidly calculating the drop size distribution.

Optical Methods

When a beam of light passes through a cloud of droplets it is absorbed and diffracted. Considering the former mechanism, the ratio of volume to surface in a spray can be related to the percentage of light absorbed. Thus an absorption photometer may be used to measure this ratio, which in turn can be translated into the Sauter mean droplet diameter (a hypothetical droplet whose ratio of volume to surface area is equal to that of the entire spray). This technique has recently been used by Dombrowski and Wolfsohn (124) but suffers from the disadvantage that the drop size distribution is unknown.

Recent developments have produced fully automatic particle size analysers, capable of measuring drops in the range 1 to 500 microns. One such device is based upon the scattering of monochromatic light as it falls on a particle. A multi-element detector translates the intensity of diffracted light at various distances from

the optical axis into the actual particle size distribution. Another device utilises a low powered laser to illuminate particles passing through the objective plane of an imaging system. Particle shadows are imaged onto a photo-diode array and are sized as an integral number of occluded elements, there the system is restrictive in that the size of the laser beam limits the maximum particle size recorded.

The technique of laser holography has recently been developed. Basically a divergent filtered laser beam is passed through the droplet spray onto a holographic plate. The resultant hologram contains the three-dimensional spray images in a two-dimensional plate. Image reconstruction is achieved by focusing the hologram at different lengths, to produce a negative containing only those droplets in focus. The images are then sized either manually or automatically.

This technique has been proven in the analysis of low density aerosol sprays, although its application to dense sprays seems doubtful (125). A system developed by Laser Holography Incorporated overcame the problem of laser holography requiring hologram development and image reconstruction. The new system used a continuously pulsing laser coupled with an ultra voilet sensitive vidicon camera and an automatic scanner. The size range capability of this machine is claimed to range

from 0.3 to 10,000 microns and particle count rates of up to 10,000 particles per second. Unfortunately these sophisticated drop size analysers tend to be very expensive and thus prohibitive.

Though most of the techniques evolved for measuring drop sizes fall into the above categories, a few involving other principles have been developed. One such device measures electrical pulses generated when a droplet intercepts a charged wire inserted in the droplet dispersion. In a similar device, charged droplets impinged on a metallic collector and the resulting electrical pulses were amplified and counted.

In selecting a suitable system in conjunction with this work, high speed photography became the obvious choice since it could also provide information regarding sheet velocity, cone angle and sheet length measurements. In addition, the mechanism of sheet disintegration could also be observed.

Measurement of Drop Size

As discussed above, a photographic technique was selected to measure the drop size distributions. Droplet illumination was provided by a high intensity short duration flash, triggered automatically when the camera shutter was opened. To prevent over exposure of the film, photography was performed in a darkened room. In practise this was achieved by enclosing the

spray tower. The photographic equipment comprised an argon jet unit supplied by Pulse Instrumentation Ltd. A 35 mm camera with 200 mm lens and 25 cm extension tube gave a short depth of field thus minimising out of focus droplets. Image magnification was obtained by placing a graticule in the field of view.

Droplet sizes were measured directly from photographic prints with the aid of a Zeiss automatic counter. The droplet image was matched to a circle of light projected from an adjustable iris and a mechanism actuated to record a count within a particular size range. Only those droplets which were in focus were counted. To avoid the aforementioned problems related to spatial drop size distributions, all photographs were taken in the region of drop formation.

This technique for drop size measurement was evaluated by comparison with results obtained using an optical array spectrometer. Results from the same experimental conditions, though not identical, were of similar magnitude. The results from the photographic technique employed in this work can therefore be treated with confidence.

A typical flash photograph illustrating the drop size distribution is presented in Figure 5.4. The drop size distributions are listed in Appendix I. Volume surface mean drop sizes are listed in Table 5.3.

NOZZLE SC

ATOMISING PRESSURE ($KN\ m^{-2}$)	SLURRY DENSITY ($Kg\ m^{-3}$)				
	1165	1265	1330	1380	1429
483	164	175	167	171	175
689	146	152	156	161	158
896	143	142	140	142	150
1103	131	128	139	138	143

NOZZLE SD

ATOMISING PRESSURE ($KN\ m^{-2}$)	SLURRY DENSITY ($Kg\ m^{-3}$)				
	1165	1265	1330	1380	1429
483	234	214	210	222	214
689	198	200	198	206	195
896	189	189	193	193	188
1103	168	177	186	175	184

TABLE 5.3 VOLUME-SURFACE MEAN DROP SIZES (m) x 10^6

NOZZLE SE

ATOMISING PRESSURE (KN m^{-2})	SLURRY DENSITY (Kg m^{-3})				
	1165	1265	1330	1380	1429
483	243	230	234	270	284
689	207	221	218	234	246
896	196	201	194	200	231
1103	175	183	183	191	211

NOZZLE SF

ATOMISING PRESSURE (KN m^{-2})	SLURRY DENSITY (Kg m^{-3})				
	1165	1265	1330	1380	1429
483	24.8	281	262	291	291
689	218	219	246	245	250
896	211	212	227	239	236
1103	194	190	210	222	225

TABLE 5.3 (continued)

Figure 5.4. Typical flash photograph of drop size distribution.

Nozzle SF Slurry

density 45%
atomising pressure 690 kNm^{-2}

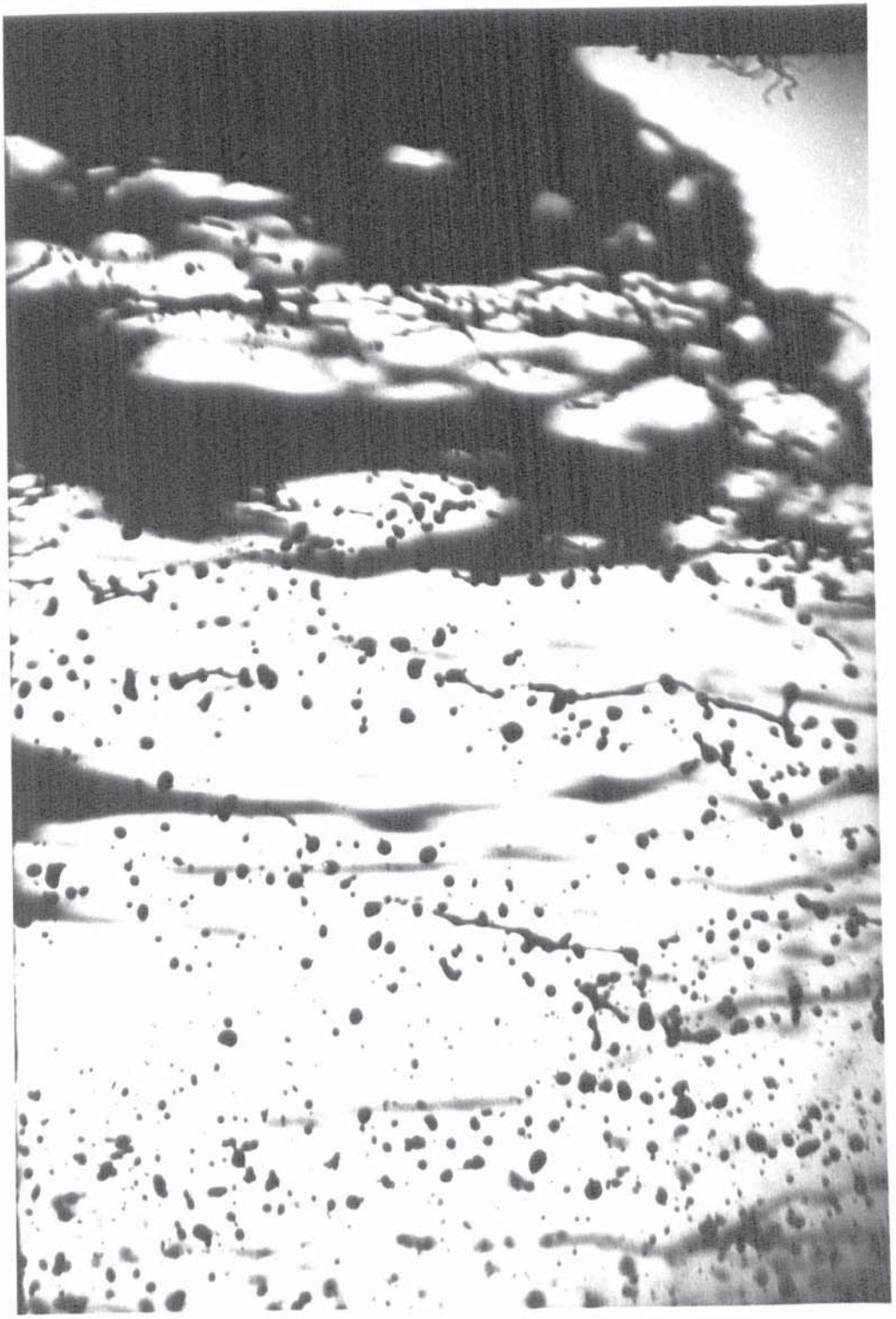

Measurement of Sheet Velocity

Some workers (99) have calculated sheet velocity from measurement of the thrust exerted on the spray nozzle by the liquid stream. For a given thrust T, and mass flowrate M, the velocity is given by:

$$V_s = \frac{T}{M\cos\theta}$$

where θ is half the maximum angle attained by the conical sheet.

Another popular means of measuring sheet velocities is by a photographic technique. A disturbance on the surface of the sheet is captured on a double exposure photograph and from a knowledge of the time interval between the two flashesand the distance travelled by the disturbance, the velocity is calculated. The latter technique was selected since a high speed photographic technique has already been employed for determining the drop size distributions. The equipment was as described above except that two such argon jets were employed. The two flasheswere separated by a time delay generated by a unit which could be varied to give delays ranging from a few nano seconds to several minutes. In practise an optimum time delay of around fifty micro seconds was used. Typical double exposure photographs are presented in Figure 5.5. Experimentally measured sheet velocities are listed in Table 5.4.

NOZZLE SC

ATOMISING PRESSURE (KN m^{-2})	SLURRY DENSITY (Kg m^{-3})				
	1165	1265	1330	1380	1429
483	18.2	18.0	17.6	15.7	14.2
689	22.9	21.6	20.1	19.3	18.6
896	27.6	25.0	24.6	22.9	23.3
1103	30.2	28.3	26.7	26.6	26.1

NOZZLE SD

ATOMISING PRESSURE (KN m^{-2})	SLURRY DENSITY (Kg m^{-3})				
	1165	1265	1330	1380	1429
483	18:1	17.8	15.4	15.1	13.8
689	23.0	22.1	20.5	20.1	18.3
896	26.3	25.6	24.7	23.8	21.6
1103	31.1	28.5	27.9	26.3	25.6

TABLE 5.4 MEASURED SHEET VELOCITIES (ms^{-1})

NOZZLE SE

ATOMISING PRESSURE ($KN\ m^{-2}$)	SLURRY DENSITY ($Kg\ m^{-3}$)				
	1165	1265	1330	1380	1429
483	18.2	17.7	17.8	16.0	15.2
689	23.5	22.7	22.0	21.3	20.8
896	27.9	26.6	26.3	24.6	24.9
1103	31.6	29.7	28.0	27.9	27.7

NOZZLE SF

ATOMISING PRESSURE ($KN\ m^{-2}$)	SLURRY DENSITY ($Kg\ m^{-3}$)				
	1165	1265	1330	1380	1429
483	18.8	18.0	17.7	16.2	16.0
689	24.7	23.5	22.3	20.2	19.9
896	28.2	27.7	25.6	24.2	23.9
1103	32.3	30.4	29.3	28.3	27.9

TABLE 5.4 (continued)

Figure 5.5. Double Exposure Photographs for Measurement of Sheet Velocity.

Nozzle SF Slurry density 45%
top 690 kNm^{-2}
lower 896 knm^{-2}

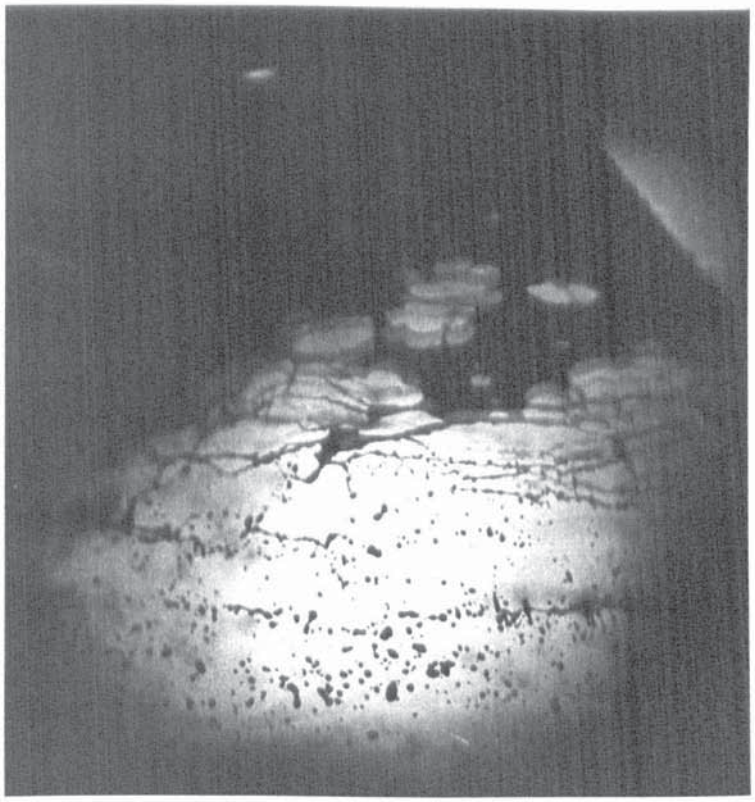

Measurement of Flowrate

In selecting a suitable flowmeter for use with chalk slurry, several different devices were considered, each presenting its own advantages and disadvantages.

Rotameters and integral orifices are widely used but are not recommended for slurry service. In addition it is rather involved to correct their readings for density variations.

Turbine flowmeters measure flowrate by detecting the frequency of pulses which are generated by turbine blades passing a pick up coil. Since the blades are in direct contact with the process fluid, slurries and viscous liquids are not suited to this type of meter.

When monitoring very low flowrates, capillary flowmeters may be considered. A pressure drop is developed in the capillary tubes which is in a linear relationship with flowrate. Since these devices operate in low Reynolds number regions, they are not applicable to rapidly settling slurries that require high flow velocities to remain in suspension.

In the target flowmeter, the flowing liquid impinges upon a flat disc. The impact force is proportional to the square of the flowrate and is detected as a measure of flow. This device operates on a force balance principle without any moving parts or pressure taps; ideal for use with slurries or

suspensions. However the device is limited to moderate viscosity ranges.

A thermal flowmeter incorporates a spool piece within the pipe, a small heater coil and two temperature sensing elements situated upstream and downstream to the coil. The temperature differential is thus a measure of flow. Its principal disadvantage although recommended for slurry service, is that the device is rather complex.

The ultrasonic flowmeter detects the amount of deflection caused by the fluid velocity to an ultrasonic beam. Its use is restricted to those fluids which possess ultrasonic properties.

In a gyroscope flowmeter, the fluid is forced through a circular path which is perpendicular to the main flow. An oscillating vibration at the input produces a torque in proportion to the mass flowrate. This meter can handle slurries in the medium pressure and temperature range but has limited use because of high cost and ability to handle only low mass flows.

Magnetic flowmeters operate on the law of electromagnetic induction, which states that a voltage is induced in a conductor when it is moved through a magnetic field. The generated voltage is proportional to the velocity at which the conductor; in this case the process fluid, moves. This device can handle slurries and viscous liquids providing they are conductive. The variety of available lining materials

makes this unit applicable to corrosive or high temperature services. This device was considered most suitable for use in this work, but its high cost was prohibitive, as indeed was the major drawback with most of the above flowmeters.

Resort was therefore made to manual flow measurement. This was achieved by collecting a volume of fluid in a known time interval and weighing it to obtain the mass flowrate. Several repetitions were made to ensure experimental accuracy, and each slurry was calibrated against measured line pressure for individual nozzles. Variation of flowrate with atomising pressure is illustrated in Table 5.5.

This technique of flow measurement, though inconvenient, proved to be reasonably accurate.

Measurement of Sheet Length and Cone Angle

Figure 5.6 demonstrates the various stages by which a liquid sheet breaks down into drops. The position at which ligament formation is visible defines the break-up length, although tears and perforations in the sheet occur at points closer to the orifice. Observation of several nozzles at a range of pressures indicated that the break-up length was subject to wide variations of the order of $\pm$ 20%. This finding is in agreement with that of Wolfson (117). He initially thought that the wide fluctuations were caused by pump pulsations

NOZZLE SC

ATOMISING PRESSURE (KN m^{-2})	SLURRY DENSITY (Kg m^{-3})				
	1165	1265	1330	1380	1429
483	7.6	8.2	8.7	9.0	9.4
689	9.2	9.9	10.6	11.0	11.5
896	10.5	11.5	12.2	12.6	13.4
1103	11.8	12.7	13.6	14.0	14.9

NOZZLE SD

ATOMISING PRESSURE (KN m^{-2})	SLURRY DENSITY (Kg m^{-3})				
	1165	1265	1330	1380	1429
483	14.6	15.2	16.2	17.5	18.2
689	17.6	18.8	19.9	21.2	21.9
896	20.5	21.7	23.0	24.2	25.1
1103	22.7	24.3	25.6	26.7	27.7

TABLE 5.5 MASS FLOWRATES THROUGH NOZZLE (Kgs^{-1}) x 10^3

NOZZLE SE

ATOMISING PRESSURE (KN m^{-2})	SLURRY DENSITY (Kg m^{-3})				
	1165	1265	1330	1380	1429
483	22.6	24.5	25.7	26.4	27.7
689	27.4	30.2	31.5	32.5	33.9
896	32.8	35.1	36.5	37.7	39.6
1103	36.7	38.9	40.8	42.0	44.2

NOZZLE SF

ATOMISING PRESSURE (KN m^{-2})	SLURRY DENSITY (Kg m^{-3})				
	1165	1265	1330	1380	1429
483	39.2	41.5	42.7	43.0	45.5
689	48.5	50.9	52.5	54.1	56.0
896	56.8	59.3	61.7	62.8	65.0
1103	63.7	67.0	68.9	70.1	73.0

TABLE 5.5 (continued)

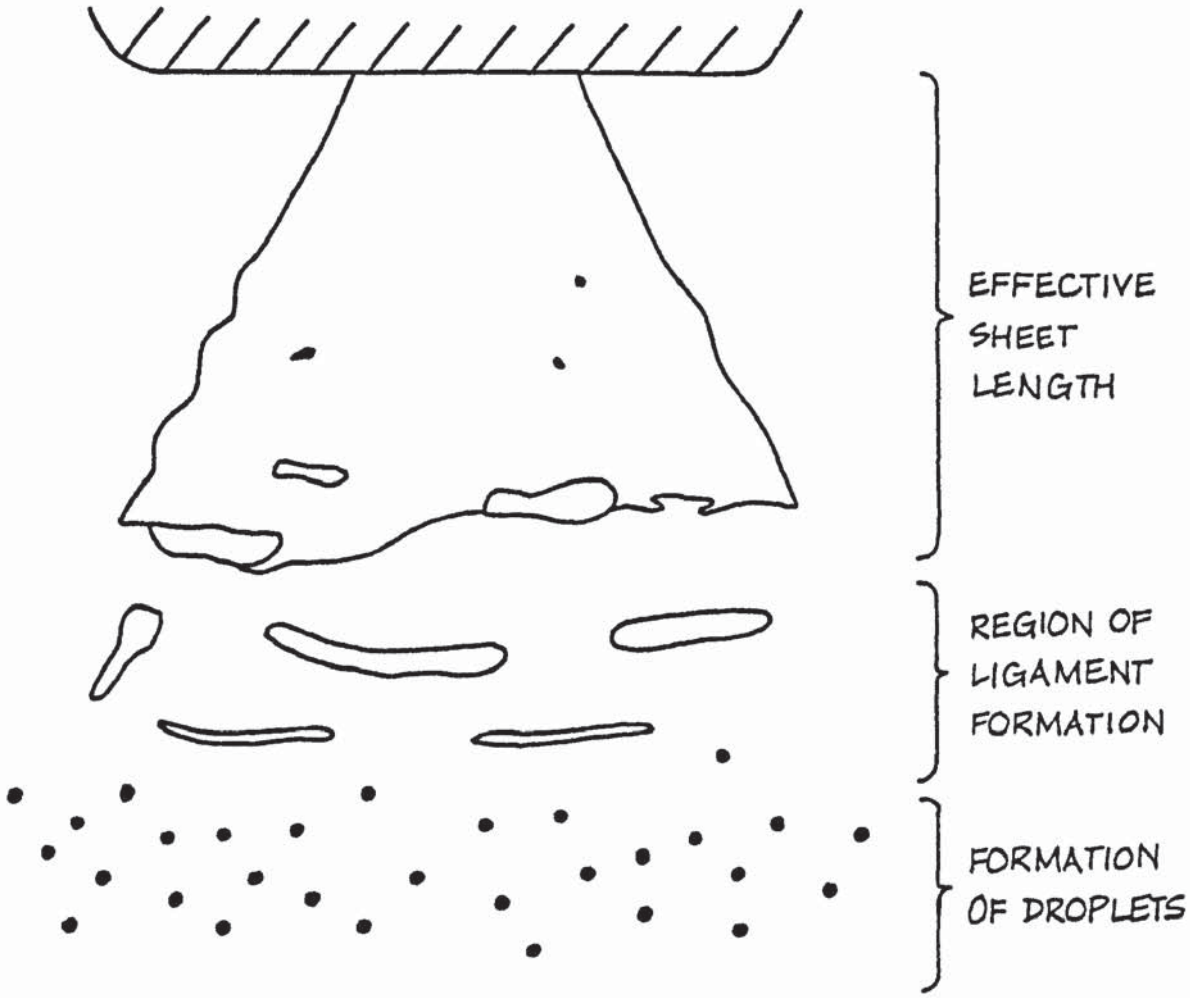

Figure 5.6. Disintegration of a Hollow Cone Spray.

but on replacing the pump with a pressure vessel eliminated this hypothesis and in turn inferred that wave motion in the air core to be the prime cause.

Since wide variations in the sheet length were therefore expected a series of flash photographs were taken and several measurements were obtained for each set of operating conditions. One such photograph is presented in Figure 5.7. The results of the sheet length measurements listed in Table 5.6 thus represent mean values.

Measurements of the cone semi angle were taken from enlargements of the same photographs used above, and the values obtained were found to be relatively consistent over the atomising pressure range. The experimental results for the cone semi angle measurements are listed in Table 5.7.

NOZZLE SC

ATOMISING PRESSURE (KN m^{-2})	SLURRY DENSITY (Kg m^{-3})				
	1165	1265	1330	1380	1429
483	14.1	15.2	16.4	17.1	18.9
689	10.3	13.3	15.4	15.8	17.7
896	10.4	12.5	15.0	13.2	15.8
1103	8.2	11.7	13.2	11.9	16.0

NOZZLE SD

ATOMISING PRESSURE (KN m^{-2})	SLURRY DENSITY (Kg m^{-3})				
	1165	1265	1330	1380	1429
483	15.8	16.3	16.6	17.0	18.1
689	11.4	13.5	15.2	15.0	16.7
896	11.4	13.0	13.7	13.2	15.9
1103	10.5	12.1	12.1	11.9	16.3

TABLE 5.6 MEASURED SHEET LENGTHS (m) x 10^3

NOZZLE SE

ATOMISING PRESSURE ($KN\ m^{-2}$)	SLURRY DENSITY ($Kg\ m^{-3}$)				
	1165	1265	1330	1380	1429
483	19.3	19.6	17.9	19.1	22.3
689	15.7	16.9	16.5	17.1	19.7
896	14.0	15.0	14.8	14.6	19.4
1103	11.5	14.2	15.0	15.5	18.8

NOZZLE SF

ATOMISING PRESSURE ($KN\ m^{-2}$)	SLURRY DENSITY ($Kg\ m^{-3}$)				
	1165	1265	1330	1380	1429
483	21.8	21.5	21.1	23.3	24.5
689	18.2	17.8	21.4	19.2	21.8
896	16.7	16.3	15.7	17.5	19.7
1103	14.3	15.9	15.4	17.6	18.2

TABLE 5.6 (continued)

Figure 5.7. Typical photograph used for sheet length measurement.

Nozzle SF slurry density 45%

690 kNm^{-2}

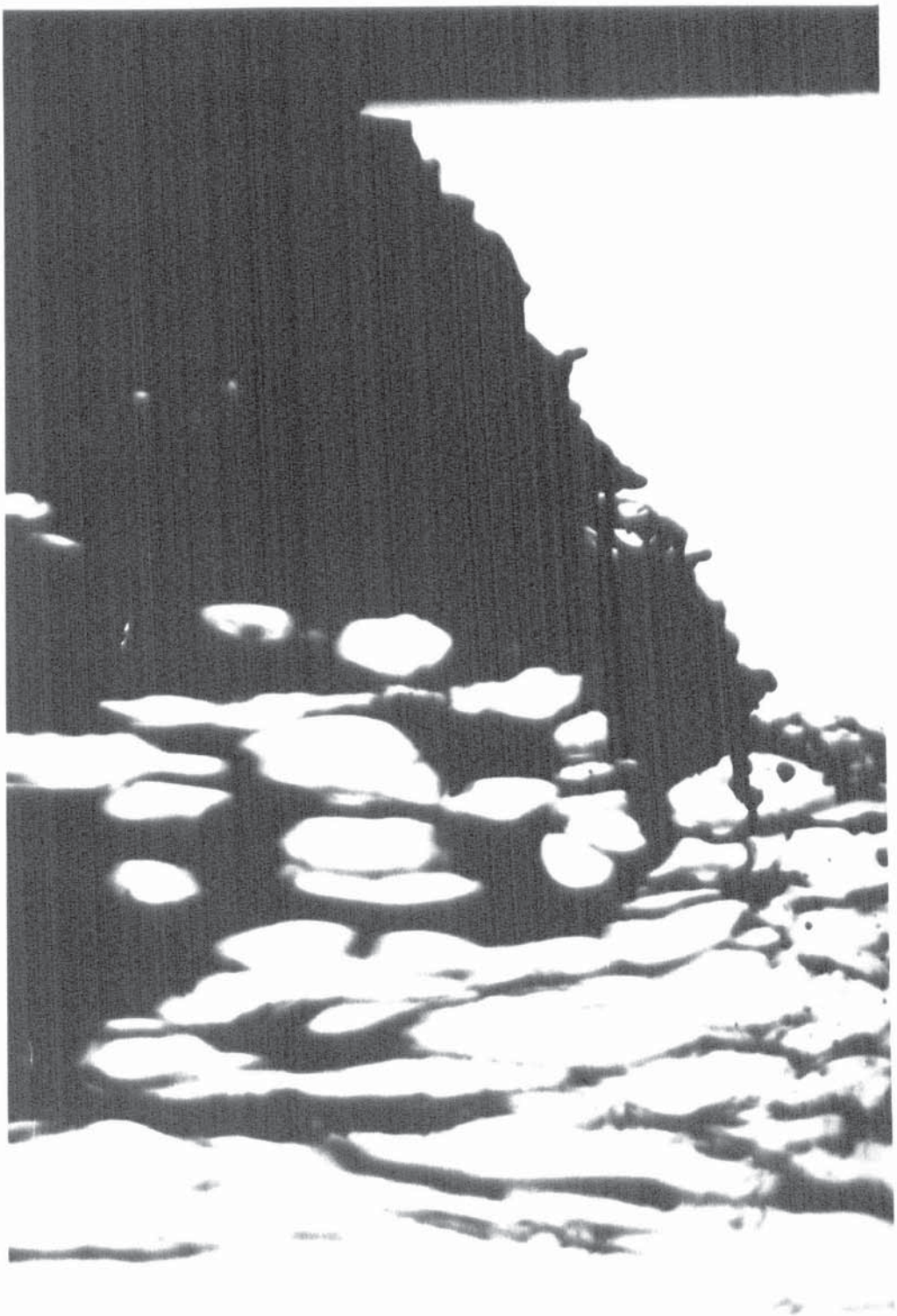

NOZZLE	SLURRY DENSITY (Kg m^{-3})				
	1165	1265	1330	1380	1429
SC	34	32	31	27	25
SD	35	34	33	31	28
SE	39	38	37	36	34
SF	40	39	38	37	36

TABLE 5.7 MEASURED CONE SEMI-ANGLES (DEGREES)

Chapter 6

Discussion

6. Discussion

Previous investigations into atomisation by swirl spray nozzles have covered a wide range of operating conditions and a variety of drop size correlations have been obtained. Water was sprayed in most studies although detergents (111) and oils (112) have been studied more recently. However, there appears to be no published work on the atomisation of slurries even though nearly all the materials which are spray dried industrially are in this form. This work presents a study of the factors that control drop formation when a chalk slurry is atomised by a swirl spray nozzle.

The mathematical model which describes these factors has taken the following structure:

(a) Fundamental boundary layer theory to predict the velocity of the sheet of slurry emitted from the nozzle.

(b) Prediction of cone angle.

(c) Prediction of sheet length.

(d) Formation of droplets.

The boundary layer equations were derived from the basic Navier-Stokes equations which were applied to the case of swirling flow within a nozzle. A first order differential equation was obtained (equation 4.23) which related the boundary layer thickness (δ) to the velocity of the fluid within the nozzle, fluid density and viscosity, and the internal dimensions of the nozzle. Table 6.1

Nozzle SC

Slurry Density kgm^{-3}	1429		1380		1330		1265		1165	
ΔP (kNm^{-2})	$\delta x10^{-4}m$	%F	$\delta x10^{-4}m$	%F	$\delta x10^{-4}m$	%F	$\delta x10^{-4}m$	%F	$\delta x10^{-4}m$	%F
483	1.841	100	1.608	90	1.195	74	1.044	65	0.853	55
690	1.742	100	1.431	87	1.068	71	0.946	62	0.77	51
896	1.651	100	1.336	84	0.989	68	0.865	59	0.722	49
1103	1.641	100	1.269	81	0.934	66	0.828	57	0.682	47
				Nozzle SD						
483	2.372	99	1.689	78	1.335	62	1.171	54	0.912	44
690	2.156	95	1.516	75	1.175	59	1.024	51	0.827	41
896	2.009	92	1.421	72	1.081	56	0.944	48	0.752	39
1103	1.93	89	1.364	69	1.022	54	0.885	47	0.716	38
				Nozzle SE						
483	2.664	85	1.906	66	1.392	52	1.192	45	0.976	37
690	2.364	82	1.677	63	1.232	49	1.048	42	0.838	34
896	2.139	79	1.535	60	1.129	47	0.957	40	0.772	33
1103	2.015	77	1.450	58	1.061	45	0.910	39	0.725	31
				Nozzle SF						
483	2.959	70	2.116	54	1.505	42	1.255	36	0.994	29
690	2.621	67	1.826	51	1.333	39	1.114	33	0.874	27
896	2.406	64	1.675	48	1.204	37	1.018	32	0.793	25
1103	2.251	62	1.580	46	1.134	36	0.944	30	0.743	24

Table 6.1. Values of Boundary Layer Thickness at Orifice.

lists the values of the boundary layer thickness at the exit orifice which was obtained when solving equation 4.23. The area of this boundary layer is also presented as a fraction of the total flow area of the annulus of fluid passing through the orifice. As expected, δ was found to be proportional to both fluid viscosity and orifice diameter and inversely proportional to the atomising pressure. It can be seen that for the smaller nozzles operating with high viscosity fluids, all flow passes through the boundary layer. However, the nozzle with the largest orifice diameter at similar operating conditions has only 70% of the flow through the boundary layer. These trends are in general agreement with Taylor (89) who estimated boundary layer thicknesses in a nozzle with straight converging sides.

Values of the semi-cone angle were calculated from the resultant of the mean axial and swirl velocity components, $\bar{v}_z$ and $\bar{v}_\theta$. The path of a fluid element emerging from the orifice is controlled by a momentum balance across the exit orifice so that the profile of the sheet is not that of a straight cone but curved. A correlation was therefore proposed which related the calculated semi-cone angle with experimental values measured at a point slightly downstream, and with various other parameters obtained from a dimensional analysis (equation 4.40). Cone semi-angles predicted by the model are compared with measured values in

Figure 6.1. Cone semi-angles varied from 25 to 40° and 61% of the predicted values lie within ± 1° of the measured value, and 92.5% within ± 2°. Since the sides of the conical liquid sheet are not straight, a tangent had to be approximated to the curved surface, so that some error may have been introduced into the sheet angle measurements.

Sheet velocities were predicted by resolving $\bar{v}_z$ through the predicted semi-cone angle. Calculated sheet velocities have been compared with measured values in Figure 6.2. Measured velocities were in the range 15 to 35 m/s and 61% of the data points lie within ± 1 m/s of the measured value, 90% within ± 2 m/s, and the remainder within + 2, - 3.3 m/s.

The coherent sheet of fluid thins as it passes through the atmosphere in the vicinity of the nozzle until at some point the waves growing on the surface cause the sheet to break up. The measured values of the sheet length up to the point of breakage were correlated with several dimensionless groups obtained from a dimensional analysis to yield an equation which predicted the sheet length (equation 4.47). The sheet lengths predicted by the model are compared with measured values in Figure 6.3. Measured sheet lengths were in the range 10 to 25 mm and 58% of predicted values lie within ± 1 mm of the measured values, 88% within ± 2 mm and 99% within ± 3 mm.

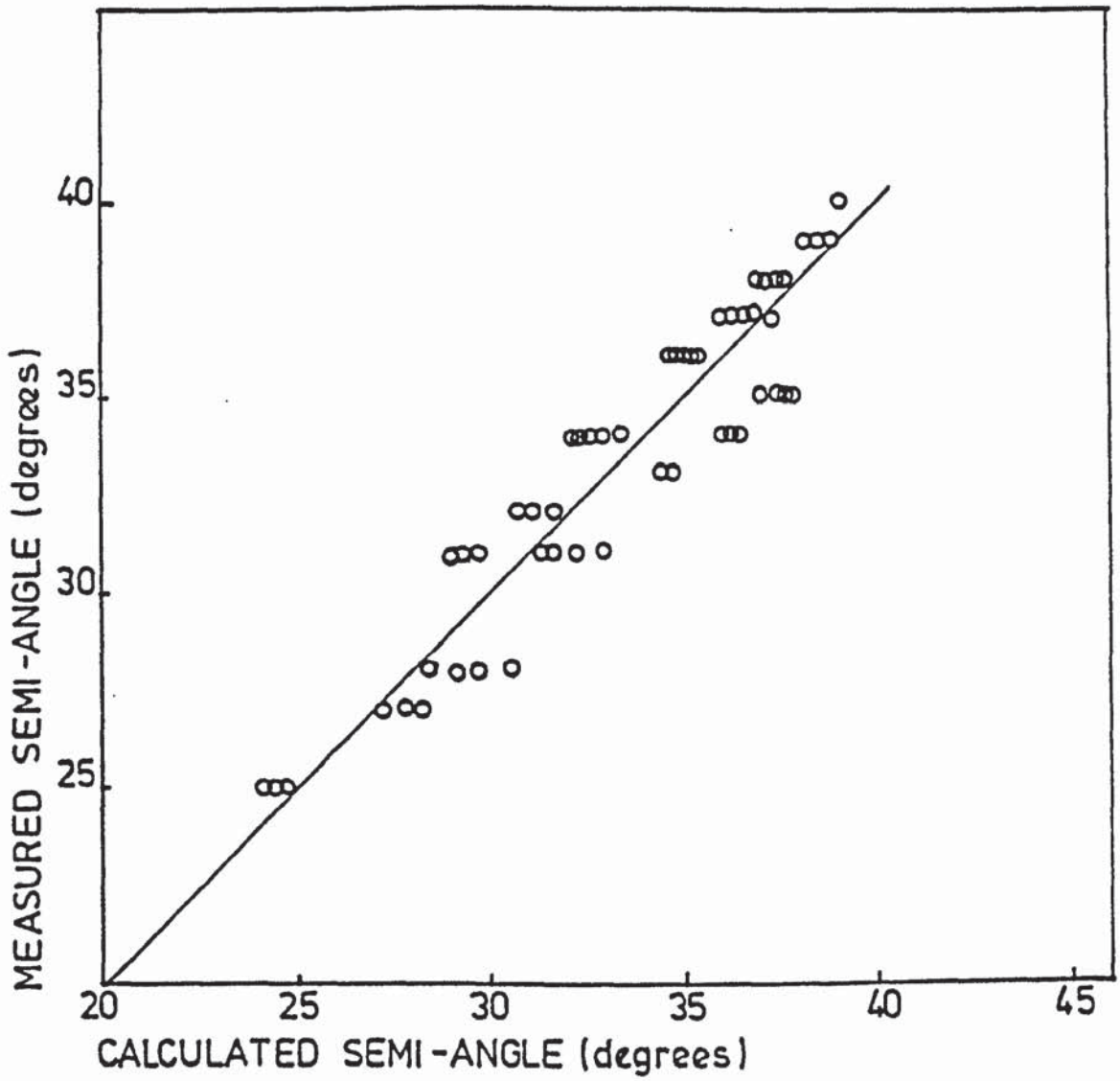

FIGURE 6:1 COMPARISON OF CALCULATED WITH MEASURED VALUES OF CONE SEMI-ANGLE

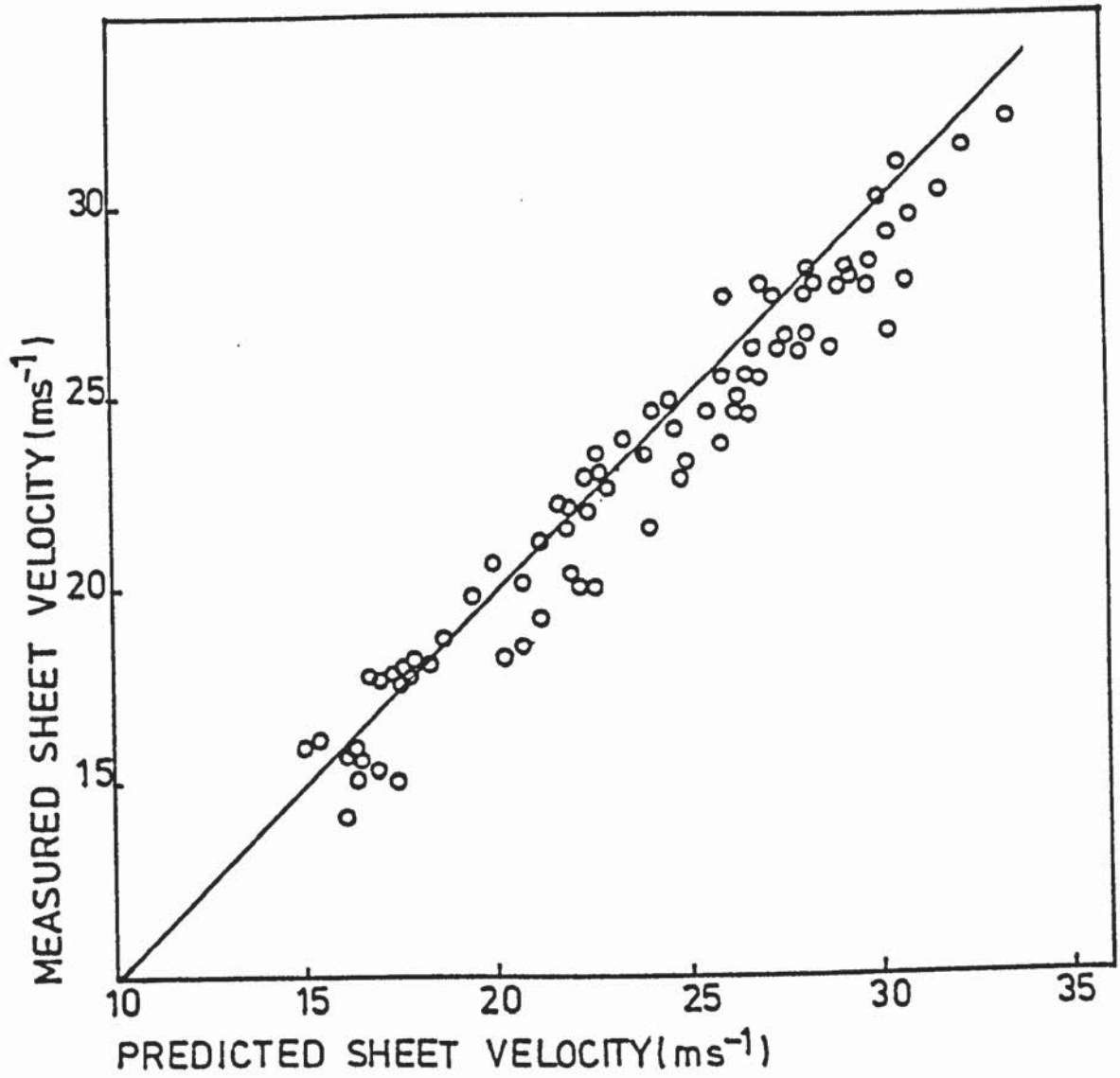

FIGURE 6:2 COMPARISON OF PREDICTED WITH MEASURED SHEET VELOCITIES

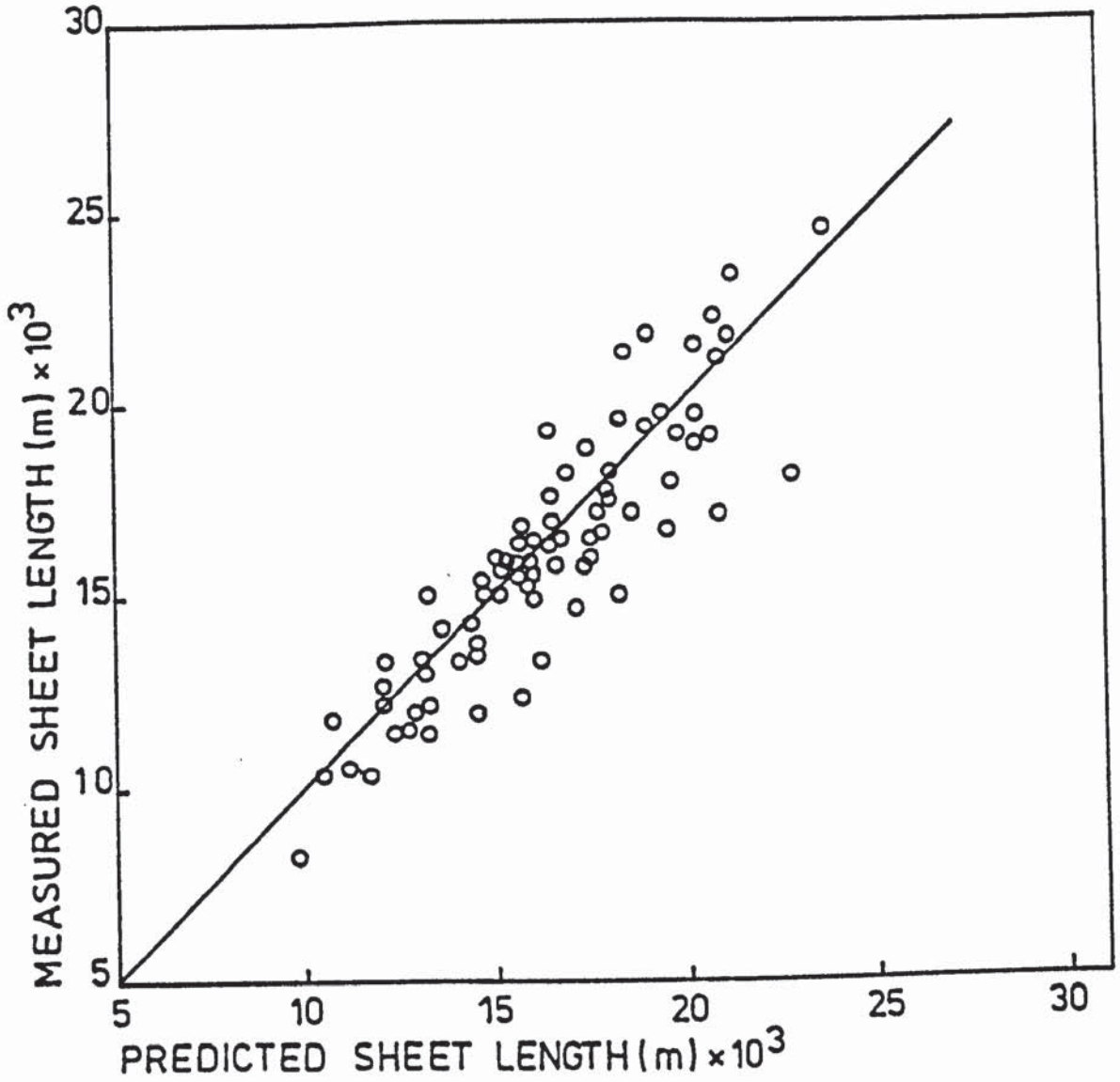

FIGURE 6:3 COMPARISON OF PREDICTED WITH MEASURED SHEET BREAKUP LENGTHS

The formation of droplets from the disintegration of the conical liquid sheet has been captured by flash photography and a typical example is illustrated in Figure 6.4. The formation of ligaments is clearly visible and similarly the formation of droplets from these ligaments, which is similar to the varicose break-up reported by Rayleigh (52). The ligaments were therefore assumed to break up into droplets by the formation of Rayleigh type disturbances, and thus drop size is a simple function of ligament diameter.

Ligaments have been assumed to form from the detachment of fragments of liquid sheet, of length one-half the wavelength of the most rapidly growing disturbance. The size of the ligament was calculated from a mass balance which required knowledge of both the sheet thickness at the point of break-up and the wavelength of the disturbance. Sheet thickness was calculated from equation 4.45 and the disintegrating wavelength, in the absence of more reliable information, was predicted from the model of Squire (equation 4.43).

The complete mathematical model predicts drop size from the simplified expression;

$$D = 0.524 \left(\frac{Q}{V_s^3 L \sin\theta}\right)^{0.5} \qquad (6.1)$$

where Q = volumetric flowrate

V_s = sheet velocity

L = sheet length

θ = semi-cone angle

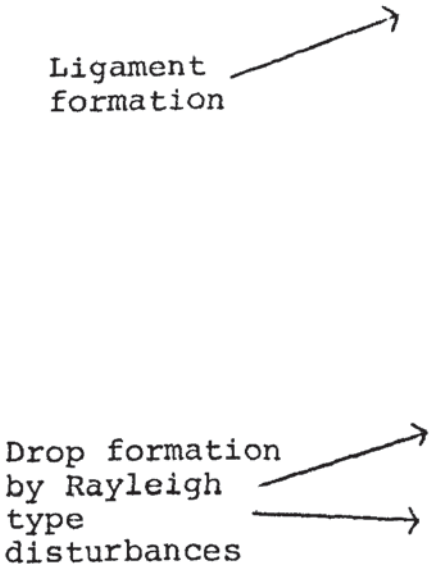

Figure 6.4. Disintegration of a sheet of slurry.

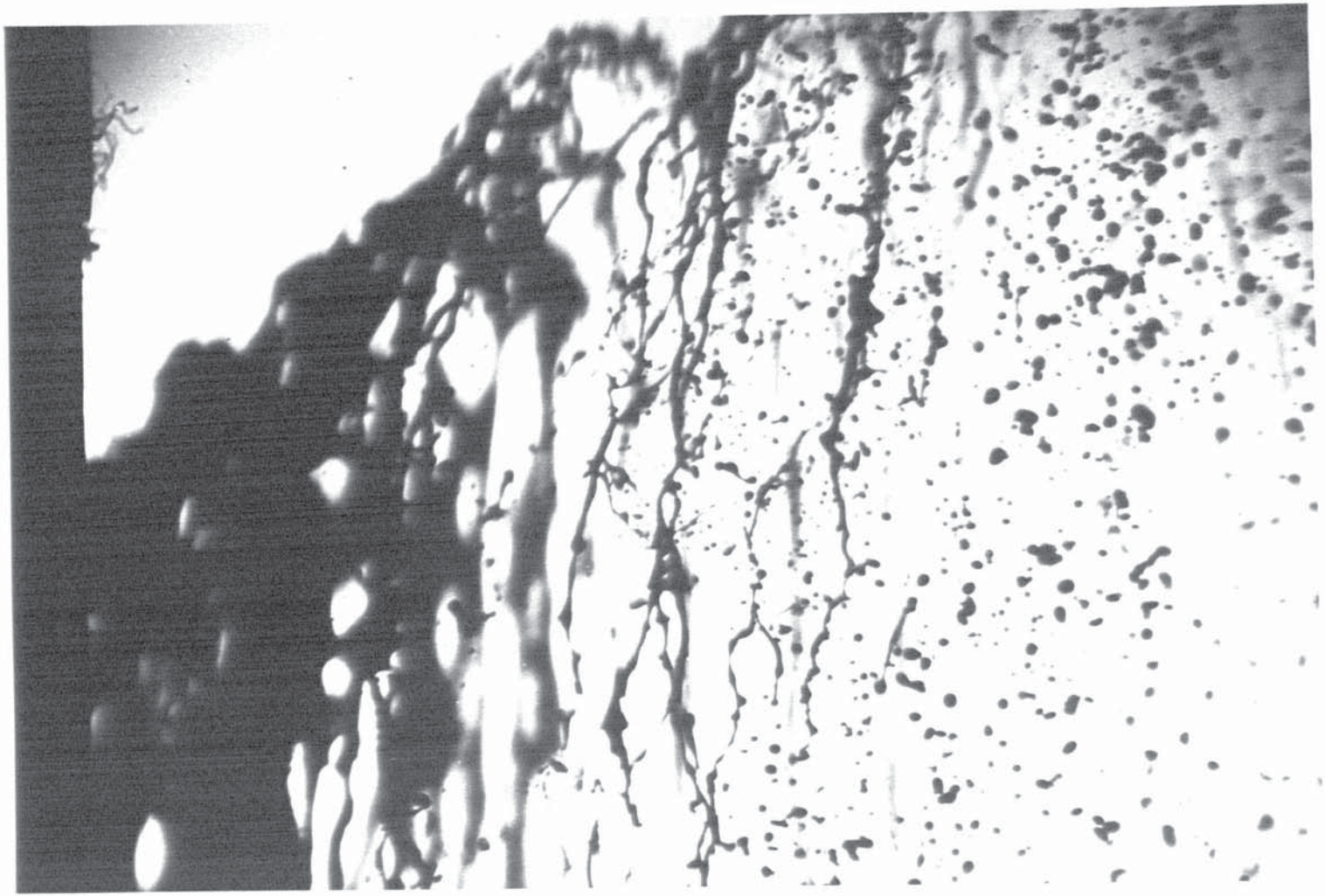

Values of predicted drop size have been compared with the measured volume surface mean diameter in Figure 6.5. The best fit of the data is about the straight line

$$D_{32} = 0.875\ D \qquad (6.2)$$

so that 61% of the data points lie within ± 20 microns of the measured value, 80% within ± 30 microns, 92.5% within ± 40 microns. Points 1 and 2 on Figure 6.5 lie well outside the measured value, but upon examination of the data represent low values of predicted sheet velocity. As the predicted drop sizes are inversely proportional to the 1.5 power of sheet velocity, a small error in estimation of the latter will magnify the error in the predicted drop size. For example, point 1 represents a predicted drop size of 433 microns, and a predicted velocity of 15 m/s. The measured velocity was 16 m/s and if this value is used in equation 6.1, the predicted drop size is reduced by approximately 10% to 390 microns, corresponding to point 1' on Figure 6.5. The data points are thus brought more into line and reduces the maximum error to 50 microns, an error of 15% at that predicted value.

Equation 6.2 thus modifies the constant in the equation for prediction of drop sizes to 0.459. This is considered justified since earlier assumptions have been made which equate the disintegration of sheets and jets

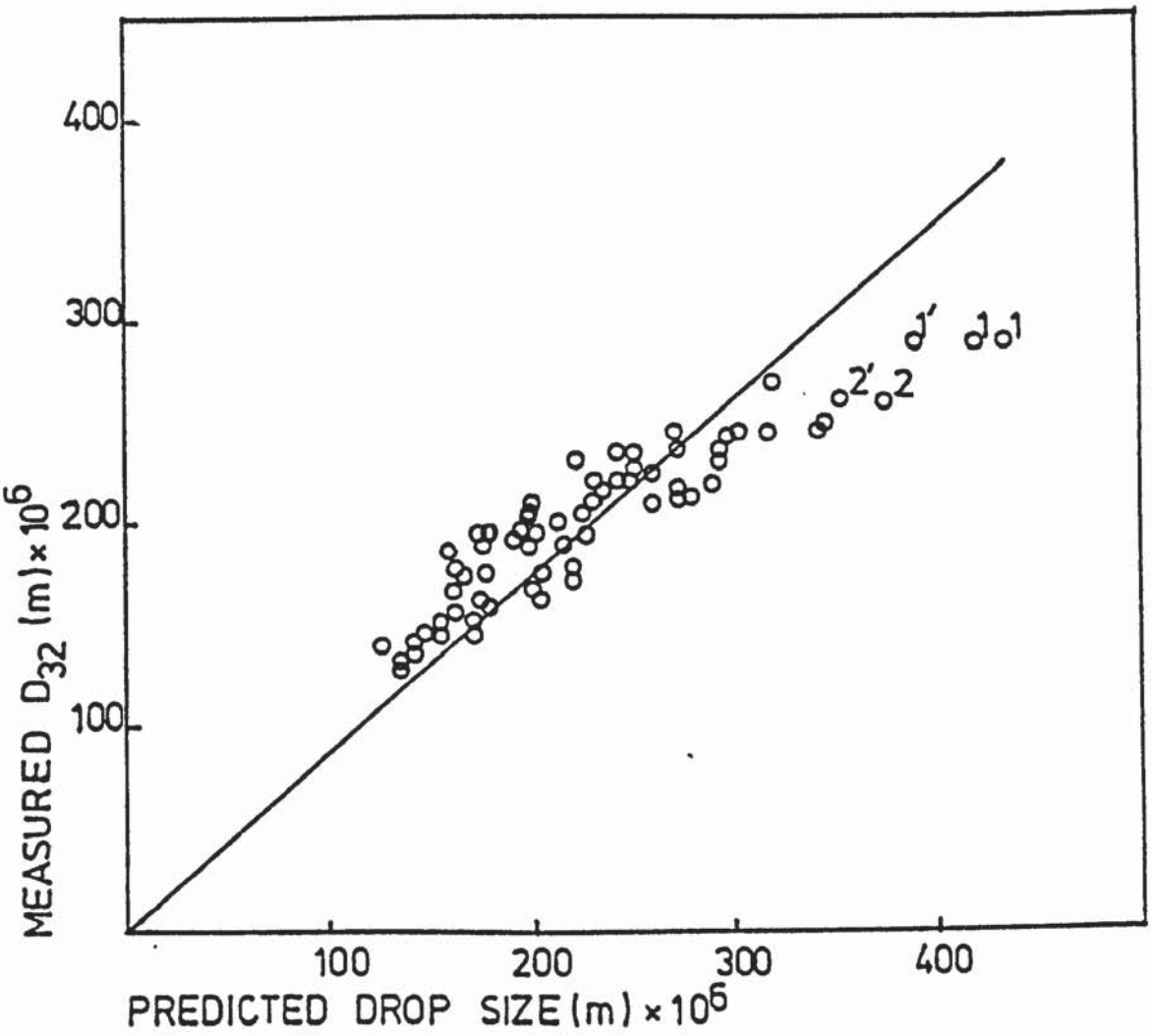

FIGURE 6:5 COMPARISON OF PREDICTED DROP SIZE WITH MEASURED VOLUME - SURFACE MEAN DIAMETER

of slurry to that of an inviscid liquid. If the theory of Rayleigh is still assumed to hold; which is supported by experimental observations (see Figure 6.4), then the analysis of Squire must be amended. This is achieved by reducing the magnitude of the constant in equation (4.43) so that:

$$\lambda = \frac{3.06\pi\sigma}{\rho_a V_s^2} \qquad (6.3)$$

This relation is similar to that derived by Dombrowski and Hooper in an analysis of attenuating liquid sheets for the conditions nh > 1.5 when dilational waves predominate.

Referring again to Figure 6.5, the trend of the data suggests that a linear regression analysis would be more representative. Thus the data is more accurately represented by the straight line:

$$D_{32} = 0.547D + 76.8 \qquad (6.4)$$

A correlation coefficient of 0.93 was obtained which suggests a good fit. 81% of the data points lie within ± 20 microns of the measured value and 99% within ± 30 microns (see Figure 6.6). However, in assuming this type of relationship no simple correlation factor can be included in the model as in the previous case.

Thus although a much better fit of measured and predicted values is obtained, the relationship is

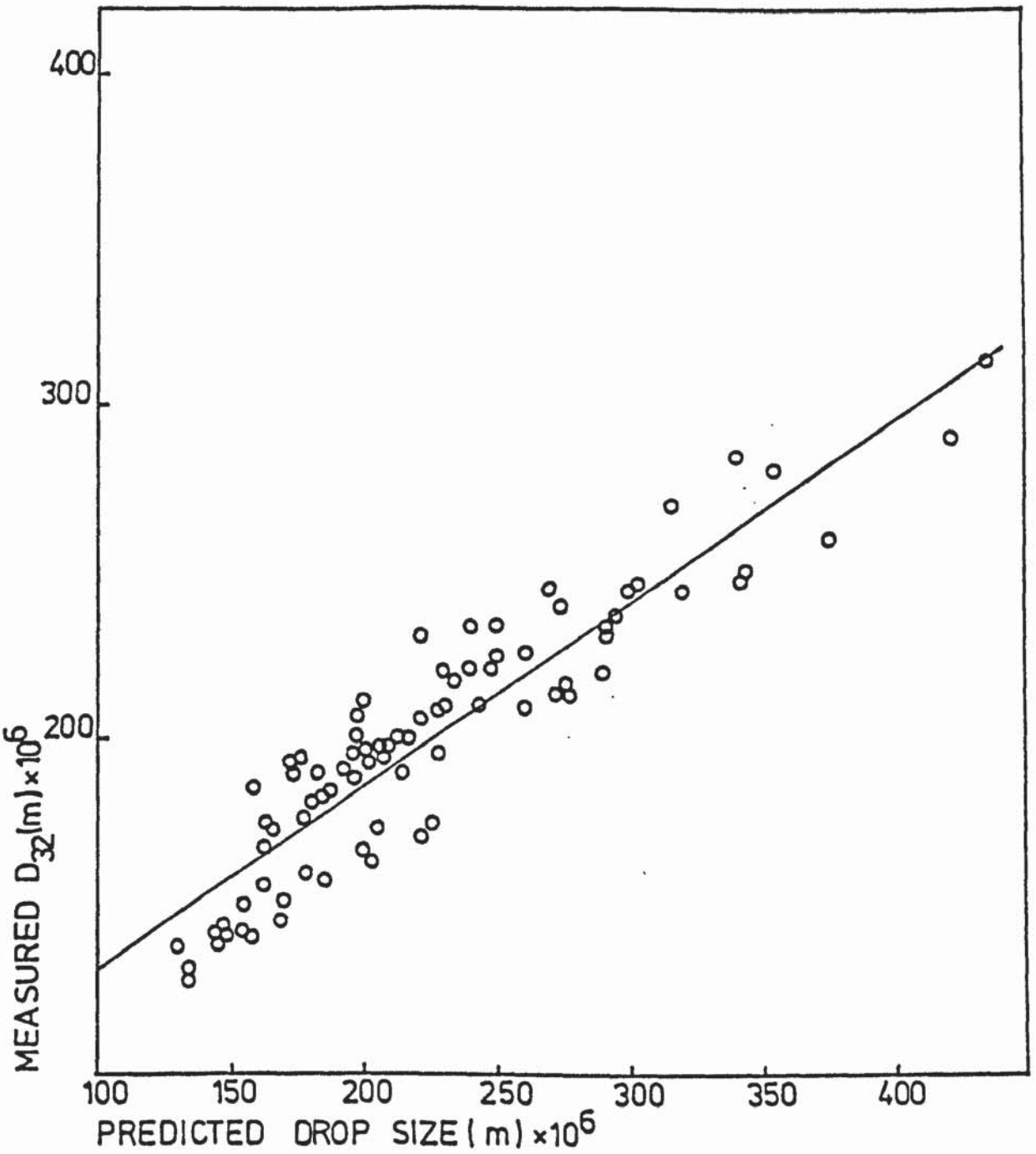

FIGURE 6:6 COMPARISON OF PREDICTED DROP SIZE WITH MEASURED VOLUME-SURFACE MEAN DIAMETER

empirical and of course does not pass through the origin. The mean drop sizes measured in this study are greater than those measured by some other workers. The high speed photographic method of drop size measurement was compared with the results obtained using a Knollenburg automatic drop size analyser (126). Results were obtained when atomising water, which compare favourably. For example, swirl nozzle SE gave the following results:

Pressure (kN/m^2)	Drop Size (D_{32})	
	Knollenburg	Photographic
690	234	215
896	164	178

The Knollenburg drop analyser eliminates the need for tedious drop counting exercises but introduces practical difficulties in its actual usage. The machine had to be placed directly in the path of the spray, which in this case was inside a spray tower. This proved rather cumbersome since firstly the machine was approximately 1 metre in length, and secondly it was not waterproof. Thus the photographic method appeared to be far more attractive, particularly in its versatility and its capability of capturing on film the mechanism of drop formation.

To illustrate the difference in the mean drop sizes obtained in this study and those from other workers,

reference is made to Figure 6.7 where the results of correlations proposed by Knight (109) and Dombrowski (112) are compared with the data from this study. Predicted values from Knight are approximately 42% smaller, and those from Dombrowski approximately 26% smaller.

Volume surface mean diameter is compared with sheet velocity for each nozzle in Figures 6.8 to 6.11. These graphs demonstrate that for a given sheet velocity drop size is independent of liquid viscosity, whereas many workers have arbitrarily assumed drop size to be directly related to viscosity. However, this finding is in agreement with Dombrowski (112) on the atomisation of oils by swirl spray nozzles. Figure 6.12 compares drop size with flowrate at two sheet velocities. This analysis would normally distinguish the effect of surface tension and these results confirm earlier experimentation that surface tension did not vary with slurry density. The data points were arbitrarily extracted and represent slurries of various densities.

Some workers have characterised the overall energy loss in a nozzle by the velocity coefficient which is the ratio of the actual sheet velocity to that corresponding to the atomising pressure, i.e.

$$k_v = \frac{V_s}{V} \qquad \text{where } V = \left(\frac{2P}{\rho}\right)^{0.5}$$

k_v in this study was found to vary in the range 0.6 to 0.8 and is similar in magnitude to values reported

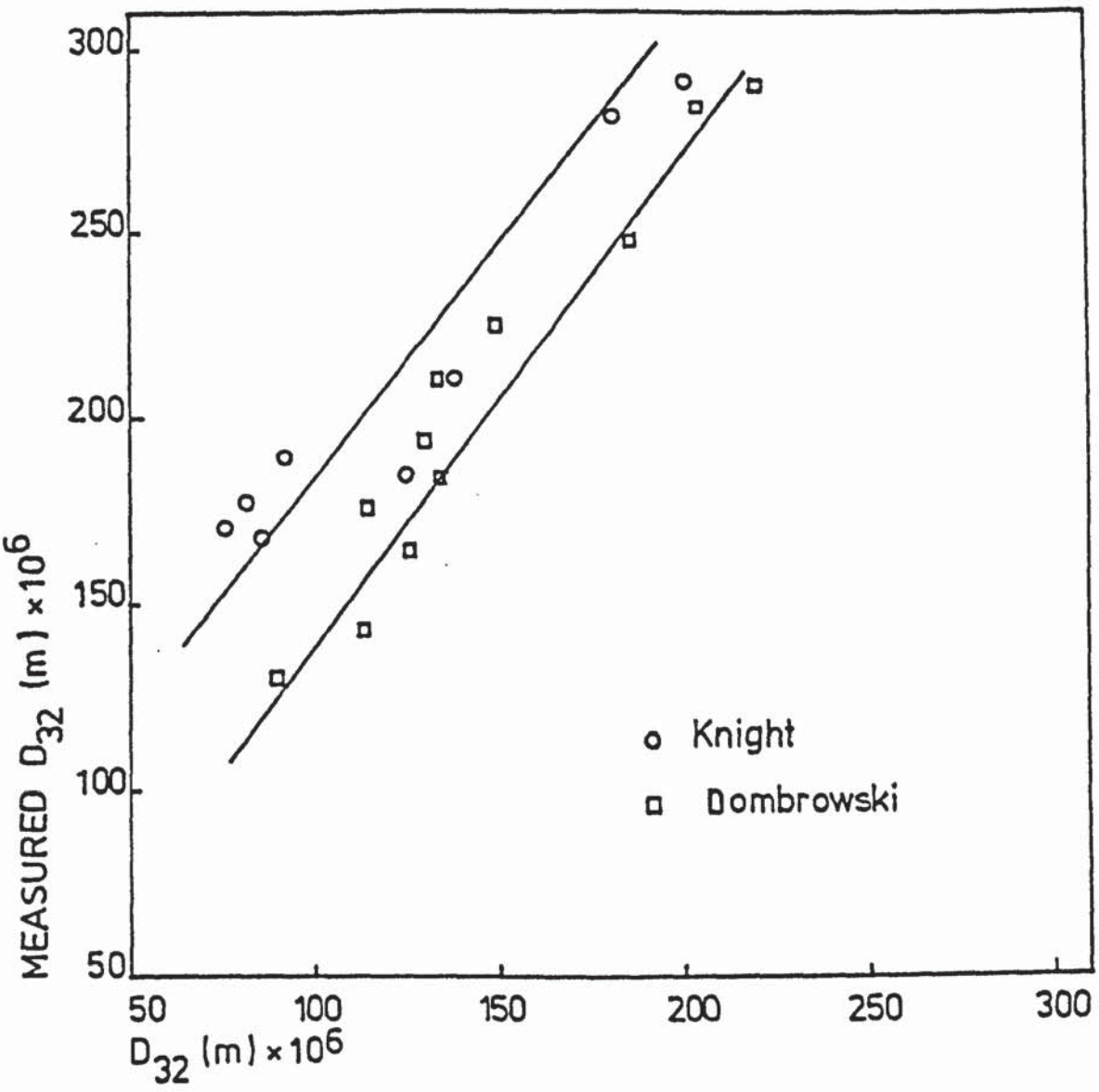

FIGURE 6:7 COMPARISON OF MEASURED MEAN DROP SIZES WITH CORRELATIONS OF OTHER WORKERS

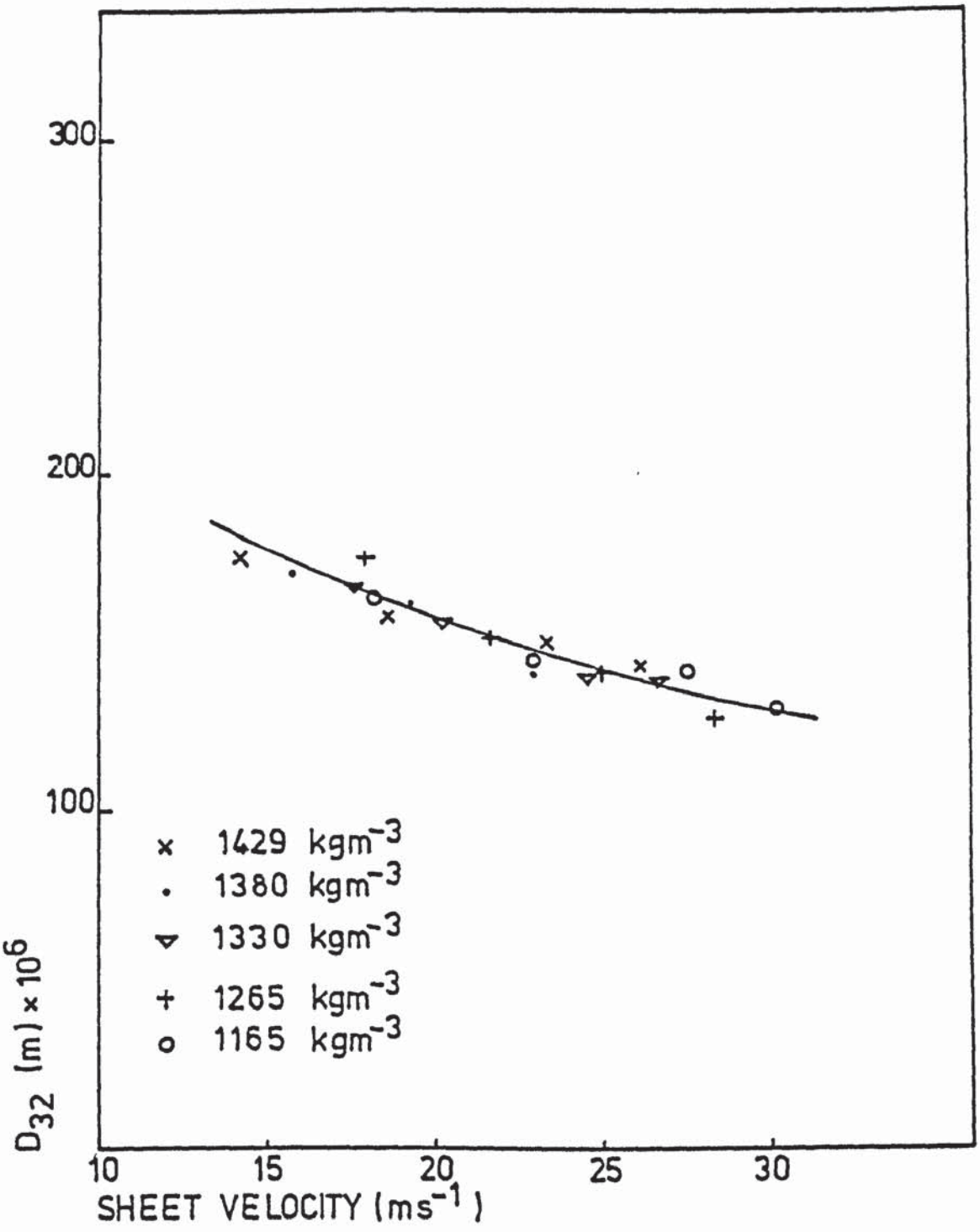

FIGURE 6:8 VARIATION OF MEAN DROP SIZE WITH SHEET VELOCITY AND SLURRY DENSITY (NOZZLE SC)

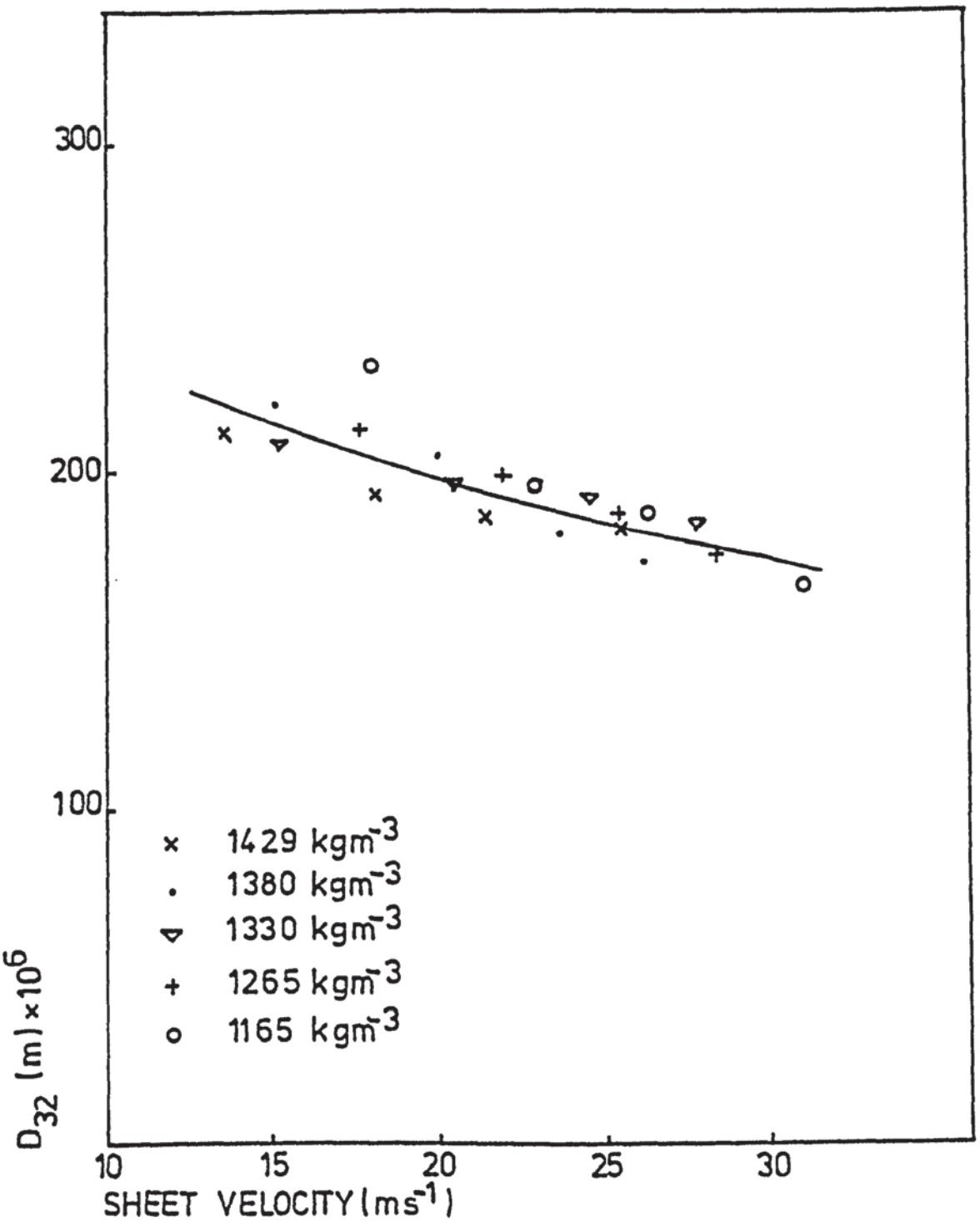

FIGURE 6:9 VARIATION OF MEAN DROP SIZE WITH SHEET VELOCITY AND SLURRY DENSITY(NOZZLE SD)

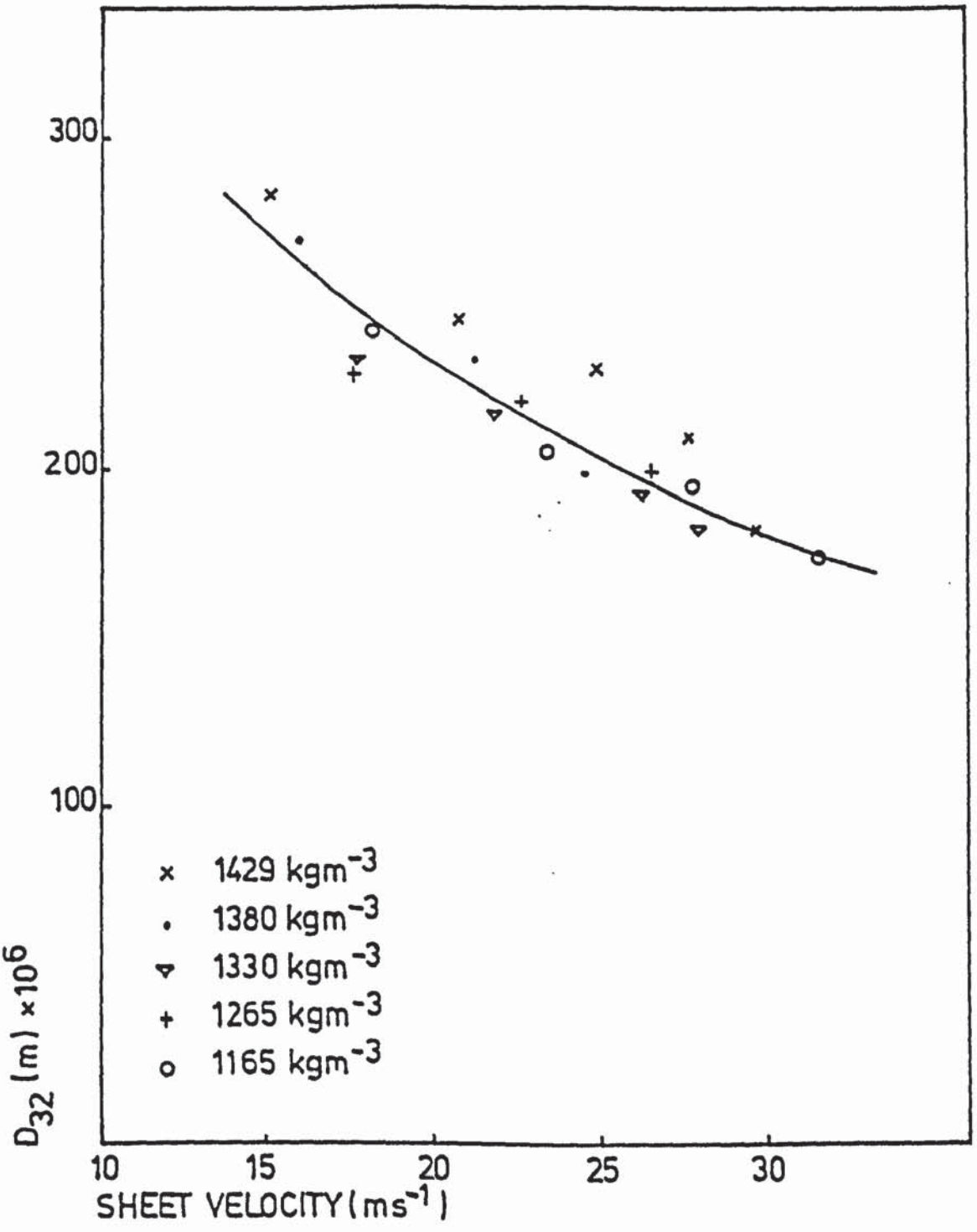

FIGURE 6:10 VARIATION OF MEAN DROP SIZE WITH SHEET VELOCITY AND SLURRY DENSITY (NOZZLE SE)

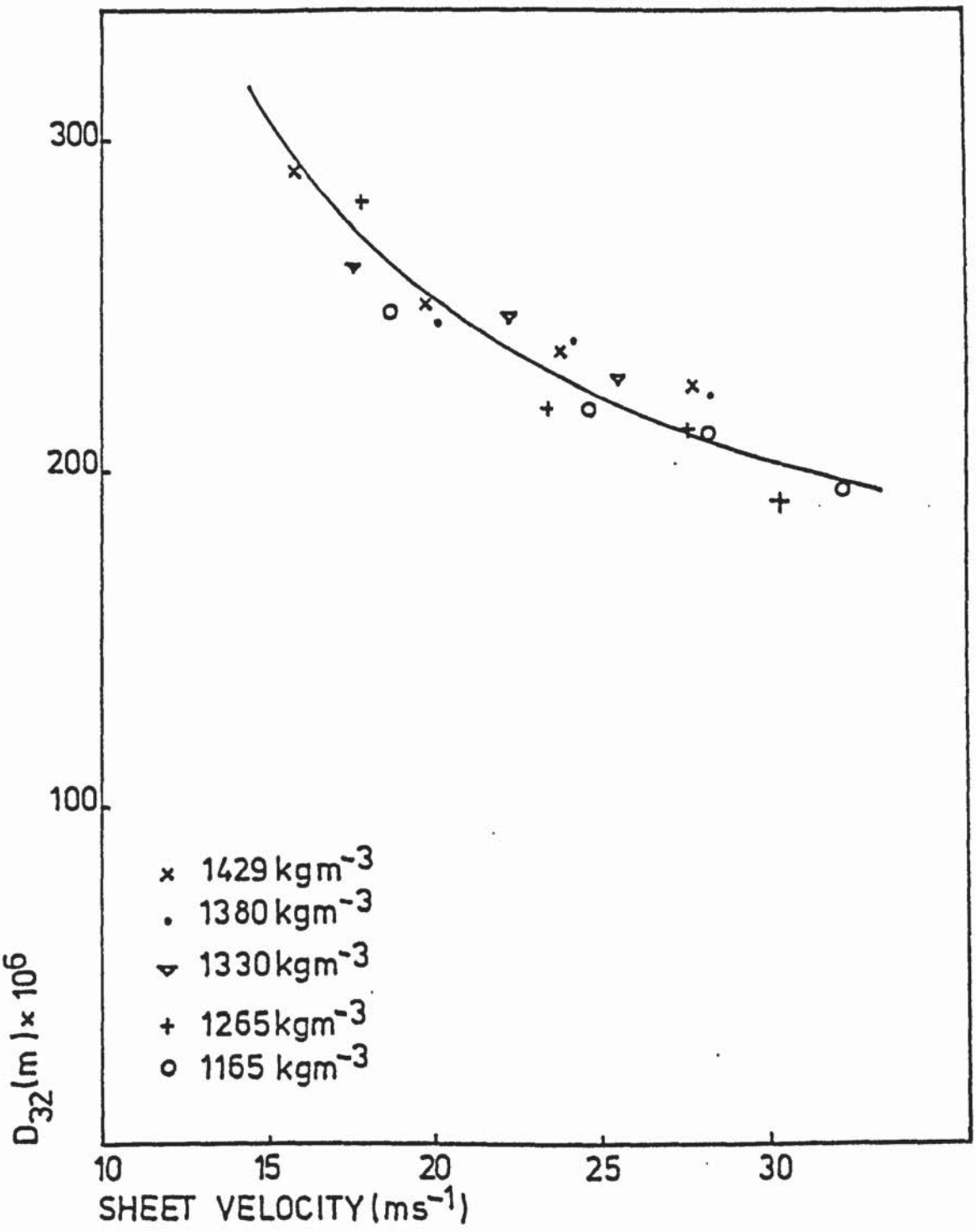

FIGURE 6:11 VARIATION OF MEAN DROP SIZE WITH SHEET VELOCITY AND SLURRY DENSITY (NOZZLE SF)

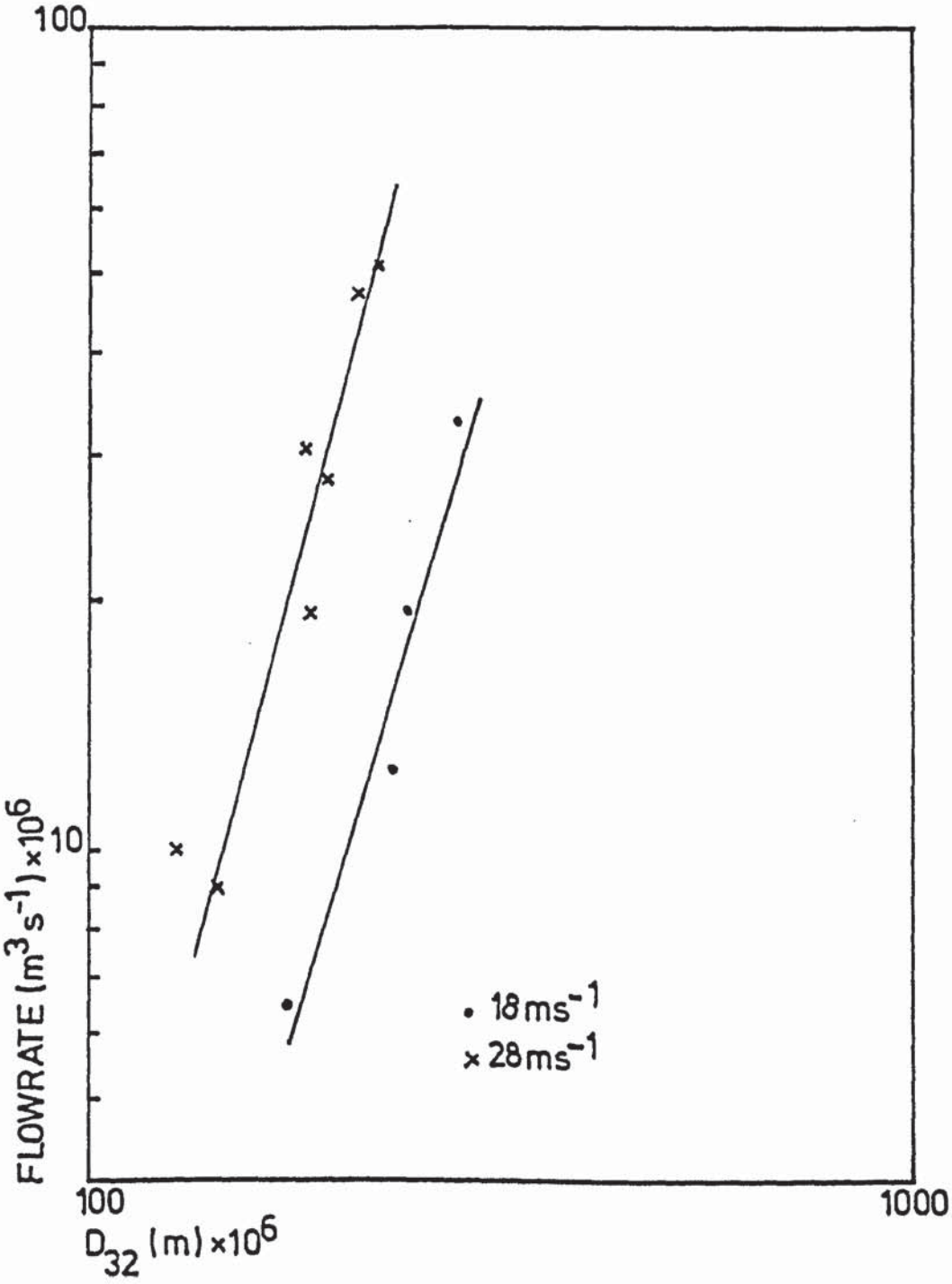

FIGURE 6:12 COMPARISON OF MEAN DROP SIZE WITH FLOWRATE AT CONSTANT SHEET VELOCITIES

elsewhere (112). Figure 6.13 shows the variation of slurry viscosity with velocity coefficient and k_v is shown to decrease with viscosity in agreement with Dombrowski. Figure 6.14 shows the variation of sheet angle (2θ) with velocity coefficient and in contrast to Dombrowski the angle is found to increase with velocity coefficient. This is believed to be due to the fact that in this work sheet angle was found to decrease with increasing slurry viscosity whereas in the previous work the two parameters were found to be independent of each other.

Table 6.2 lists the values of sheet angle and velocity coefficient measured in this study. In general, sheet angle is independent of atomising pressure but dependent on both viscosity and nozzle size. Similar trends were found for the behaviour of the velocity coefficient.

Figure 6.15 compares different viscosity slurries at constant pressure and demonstrates that the lower viscosity slurry produces finer drop sizes as a result of the increased velocity coefficient. This is because, for higher values of k_v the sheet velocity is increased and as shown earlier (equation 6.1) drop size is inversely proportional to sheet velocity.

The discharge through a swirl nozzle may be represented in terms of a discharge coefficient (C_d) so that

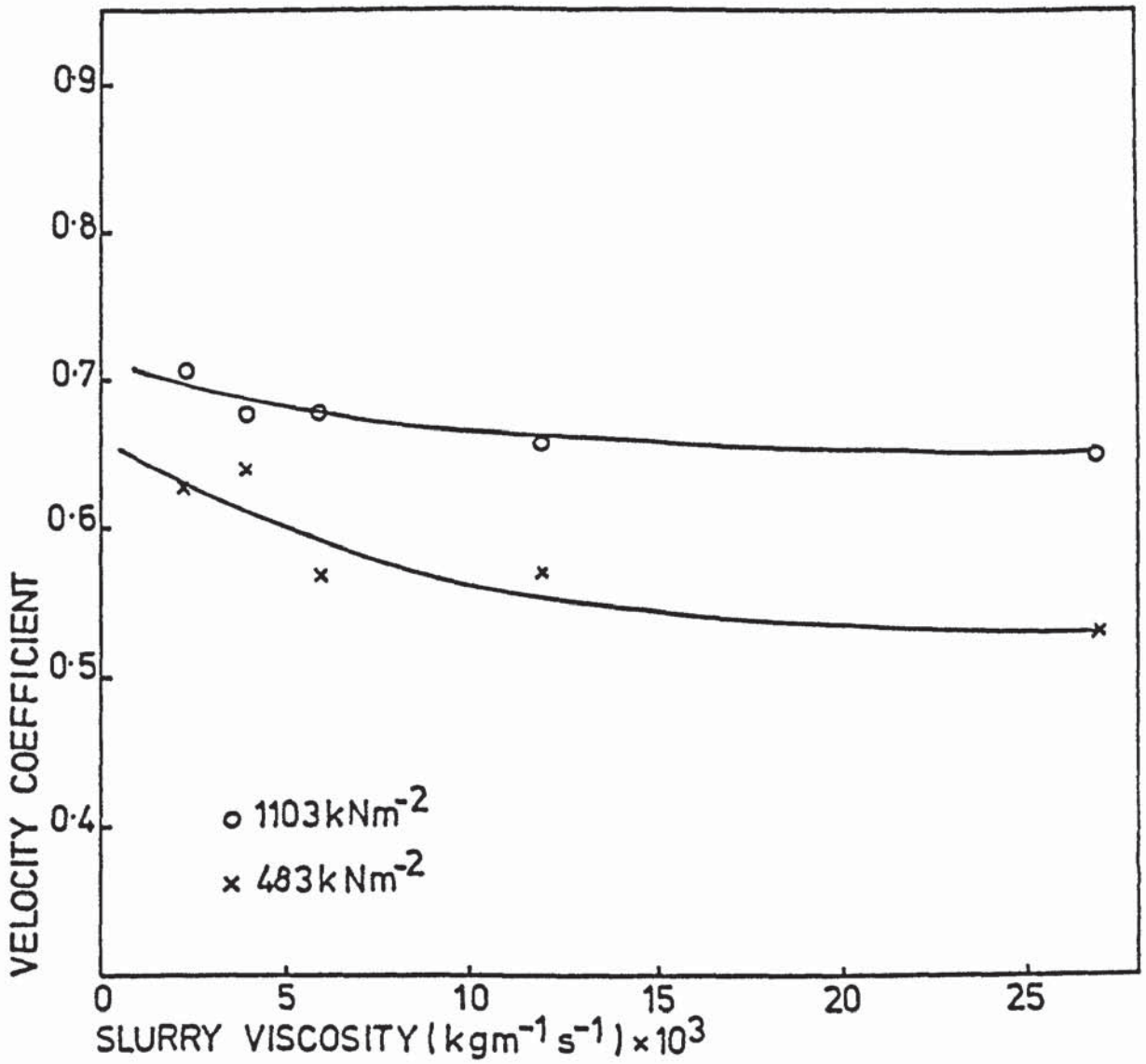

FIGURE 6:13 VARIATION OF SLURRY VISCOSITY WITH VELOCITY COEFFICIENT (NOZZLE SD)

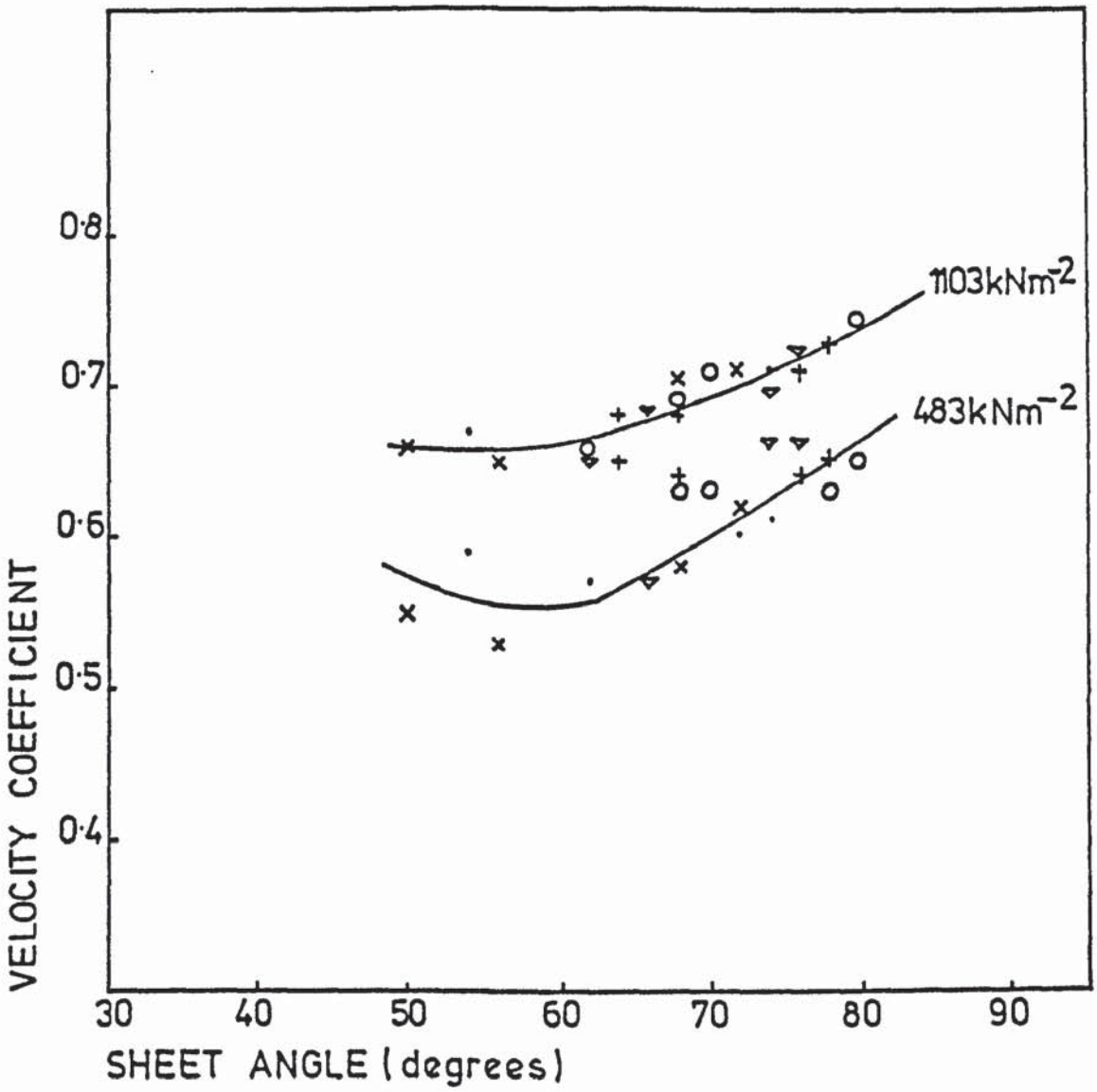

FIGURE 6:14 VARIATION OF VELOCITY COEFFICIENT WITH SHEET ANGLE AT CONSTANT PRESSURE

Slurry Density ($Kg\ m^{-3}$)	1429		1380		1330		1265		1165	
ΔP ($kN\ m^{-2}$)	K_v	θ	K_v	θ	K_v	θ	K_v	θ	K_v	θ
				Nozzle SC						
483	.55		.59		.65		.65		.63	
490	.60	50°	.61	54°	.62	62°	.65	64°	.67	68°
896	.66		.64		.67		.66		.70	
1103	.66		.67		.66		.68		.69	
				Nozzle SD						
483	.53		.57		.57		.64		.63	
690	.59	56°	.64	62°	.64	66°	.67	68°	.67	70°
896	.61		.66		.67		.68		.67	
1103	.65		.66		.68		.68		.71	
				Nozzle SE						
483	.58		.60		.66		.64		.63	
690	.67	68°	.67	72°	.68	74°	.69	76°	.68	78°
896	.70		.68		.72		.71		.71	
1103	.71		.70		.69		.71		.73	
				Nozzle SF						
483	.62		.61		.66		.65		.65	
690	.64	72°	.64	74°	.69	76°	.71	78°	.72	80°
896	.68		.67		.70		.74		.72	
1103	.71		.71		.72		.73		.74	

Table 6.2. Table of Velocity Coefficient (K_v) and Cone Angle (2θ)

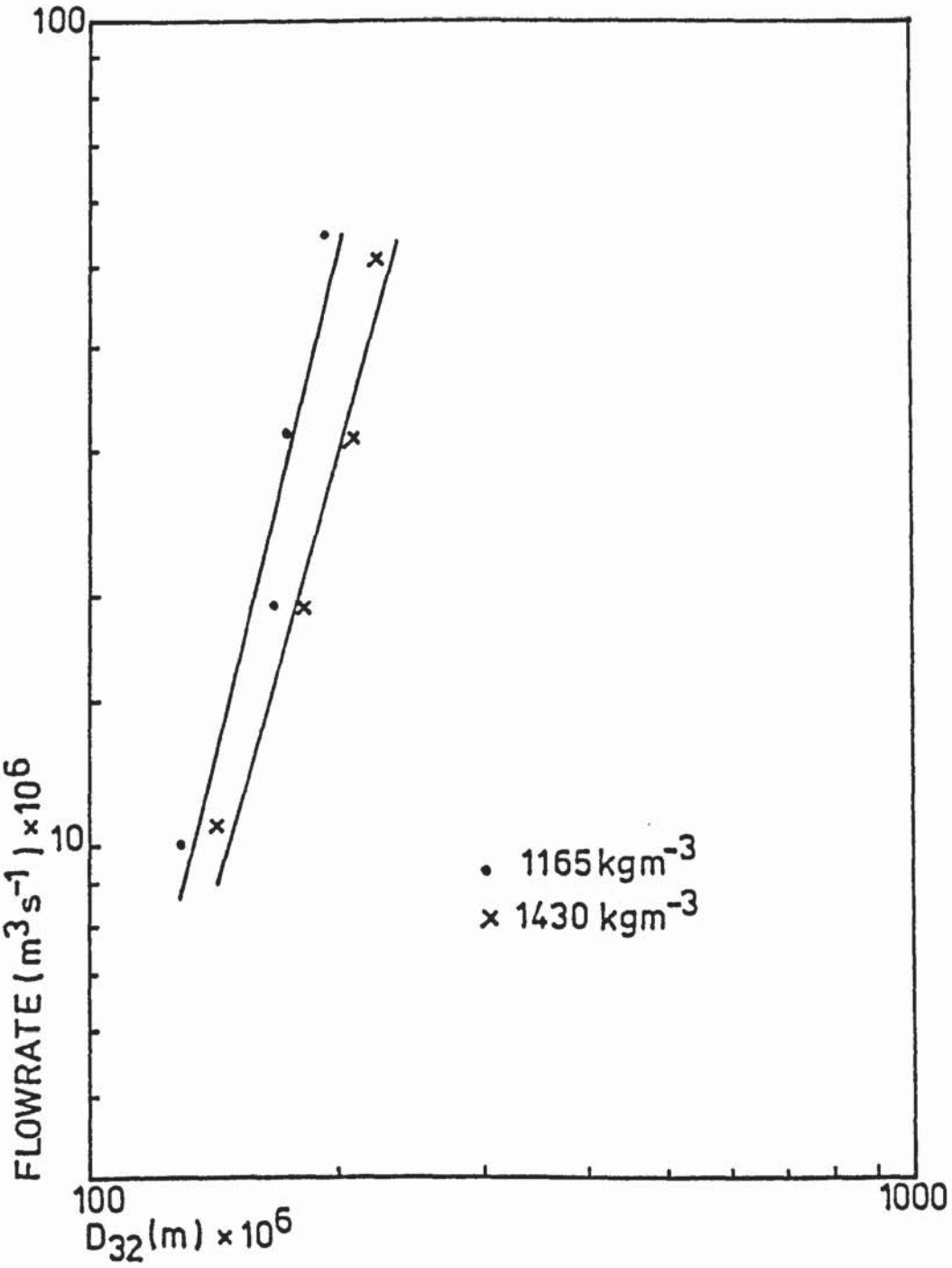

FIGURE 6:15 COMPARISON OF MEAN DROP SIZE WITH FLOWRATE AT CONSTANT PRESSURE (1103 kN m^{-2})

$$Q = C_d A \left(\frac{2P}{\rho}\right)^{0.5} \qquad (6.5)$$

where C_d represents the ratio of the actual discharge rate to that obtained when the total orifice area is effective to flow and the pressure energy is converted to kinetic energy without loss. It follows from equation 6.5 that a plot of mass flowrate against the square root of the pressure drop through the nozzle results in a straight line, the gradient being a measure of

$$C_d A \, (2\rho)^{0.5}$$

This is illustrated in Figures 6.16 to 6.19 when straight line relationships were obtained. In swirl spray nozzles most of the energy losses are frictional, the effectual area of the orifice is reduced by the air core and thus lower discharge coefficients are obtained. From an analysis of inviscid liquids C_d has been found independent of the pressure drop and has been related to a parameter relating the dimensions of the atomiser. As liquid viscosity is reduced the value of C_d is increased due to the increased axial and tangential velocity components. However on further reduction of viscosity the tangential velocity component increases more than the axial velocity component, which leads to a larger air core and lower discharge coefficients. Discharge coefficient is thus a complex function of the nozzle parameter relation.

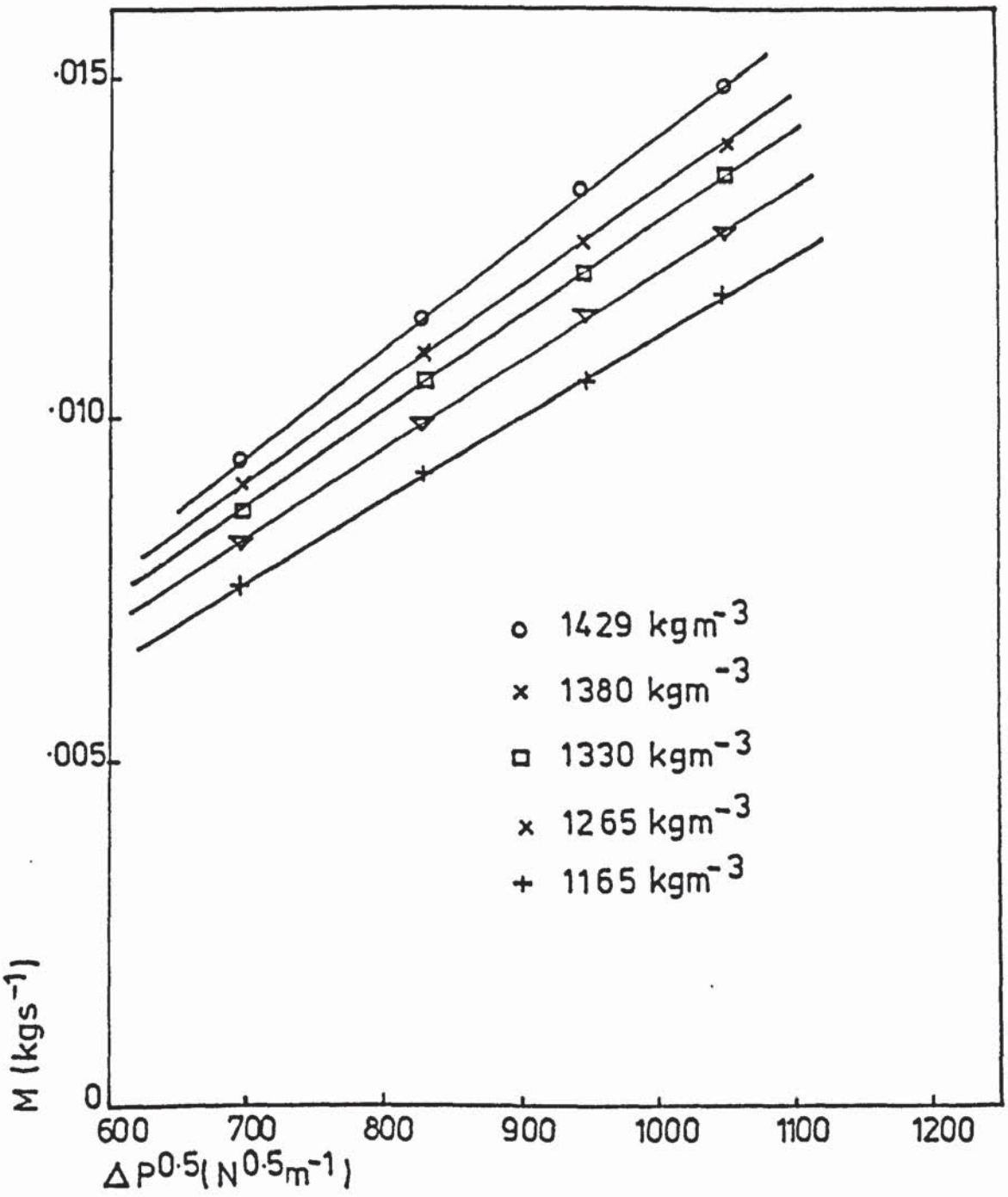

FIGURE 6.16 VARIATION OF SLURRY FLOWRATE WITH SQUARE ROOT OF NOZZLE PRESSURE (NOZZLE SC)

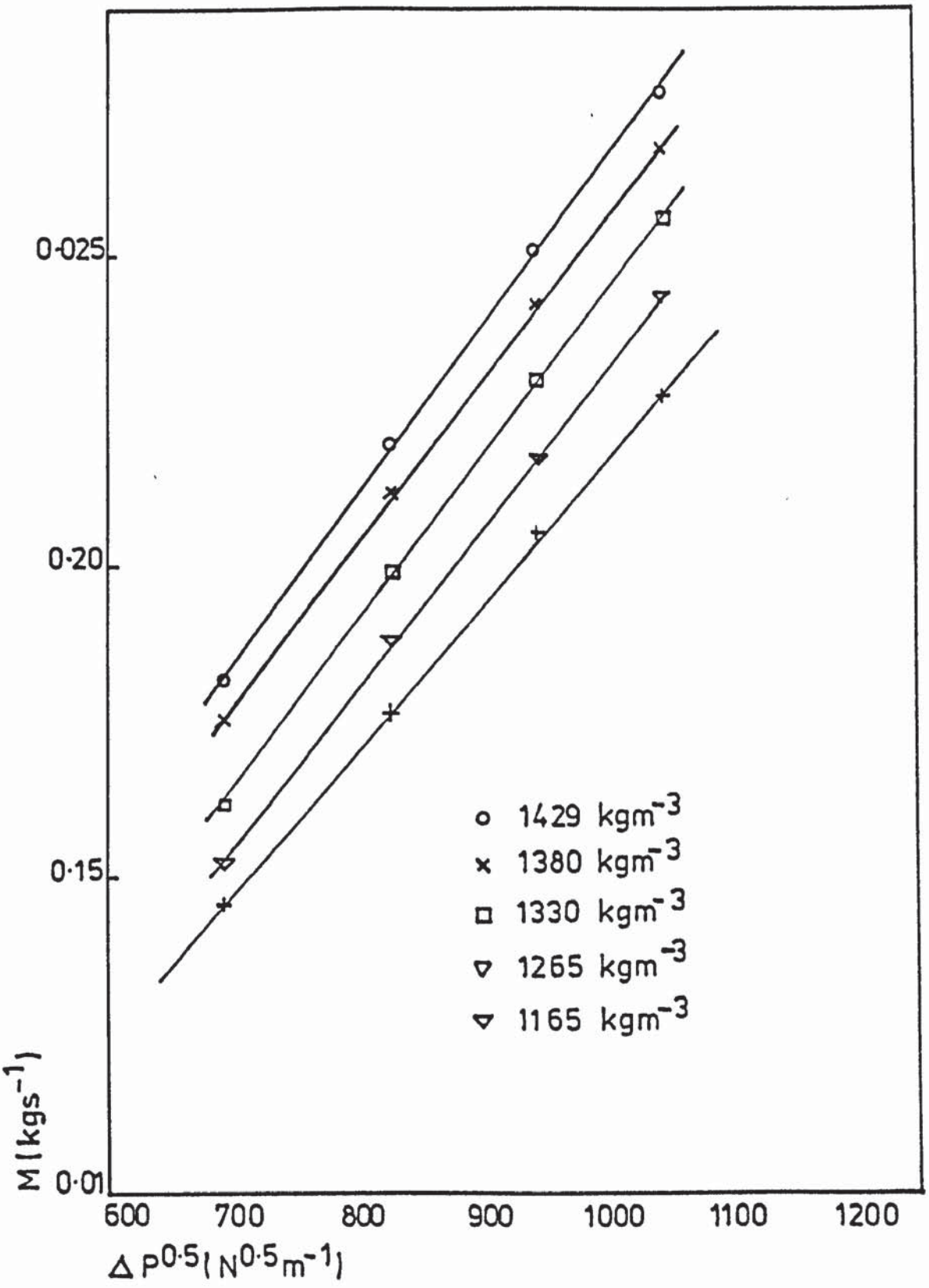

FIGURE 6.17 VARIATION OF SLURRY FLOWRATE WITH SQUARE ROOT OF NOZZLE PRESSURE (NOZZLE SD)

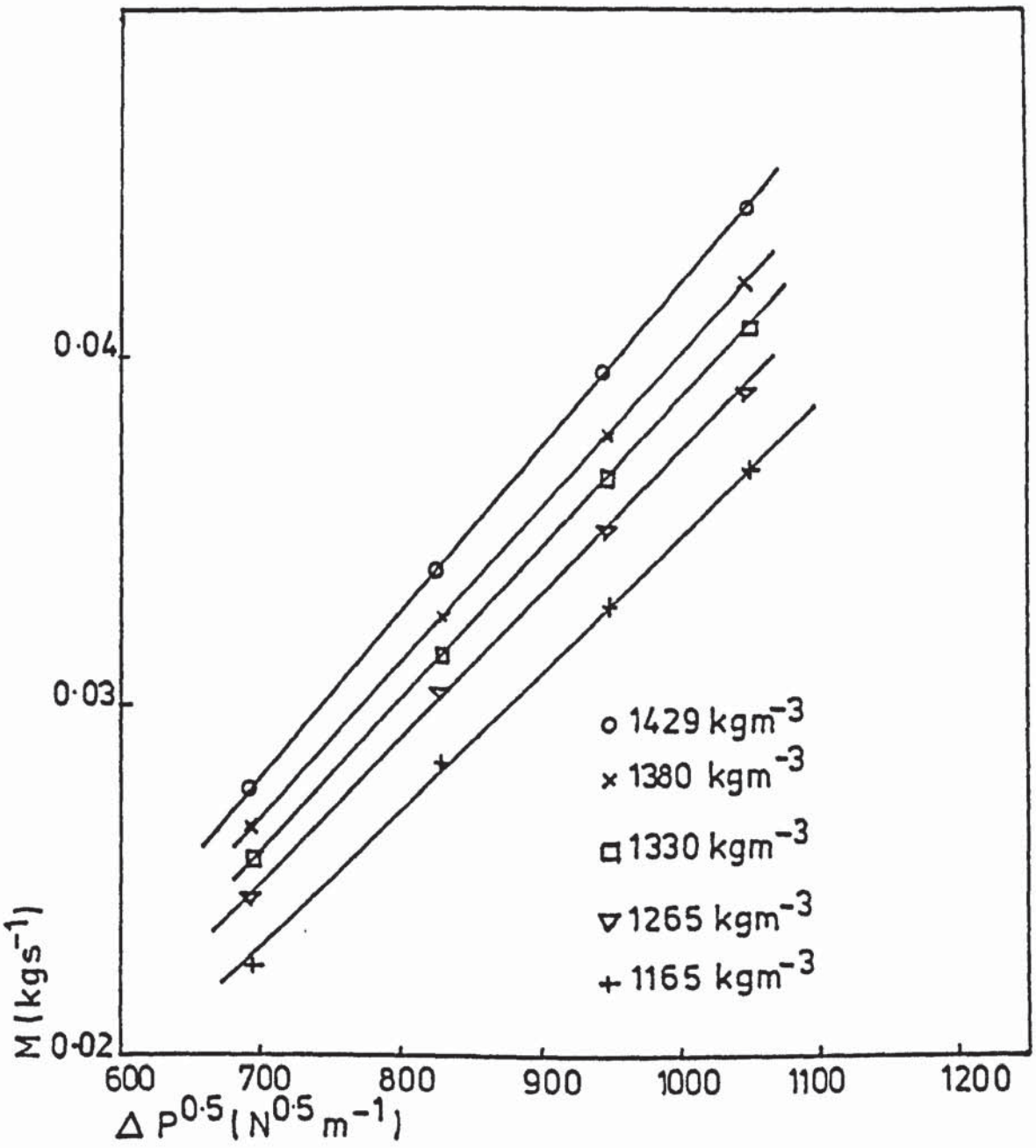

FIGURE 6.18 VARIATION OF SLURRY FLOWRATE WITH SQUARE ROOT OF NOZZLE PRESSURE (NOZZLE SE)

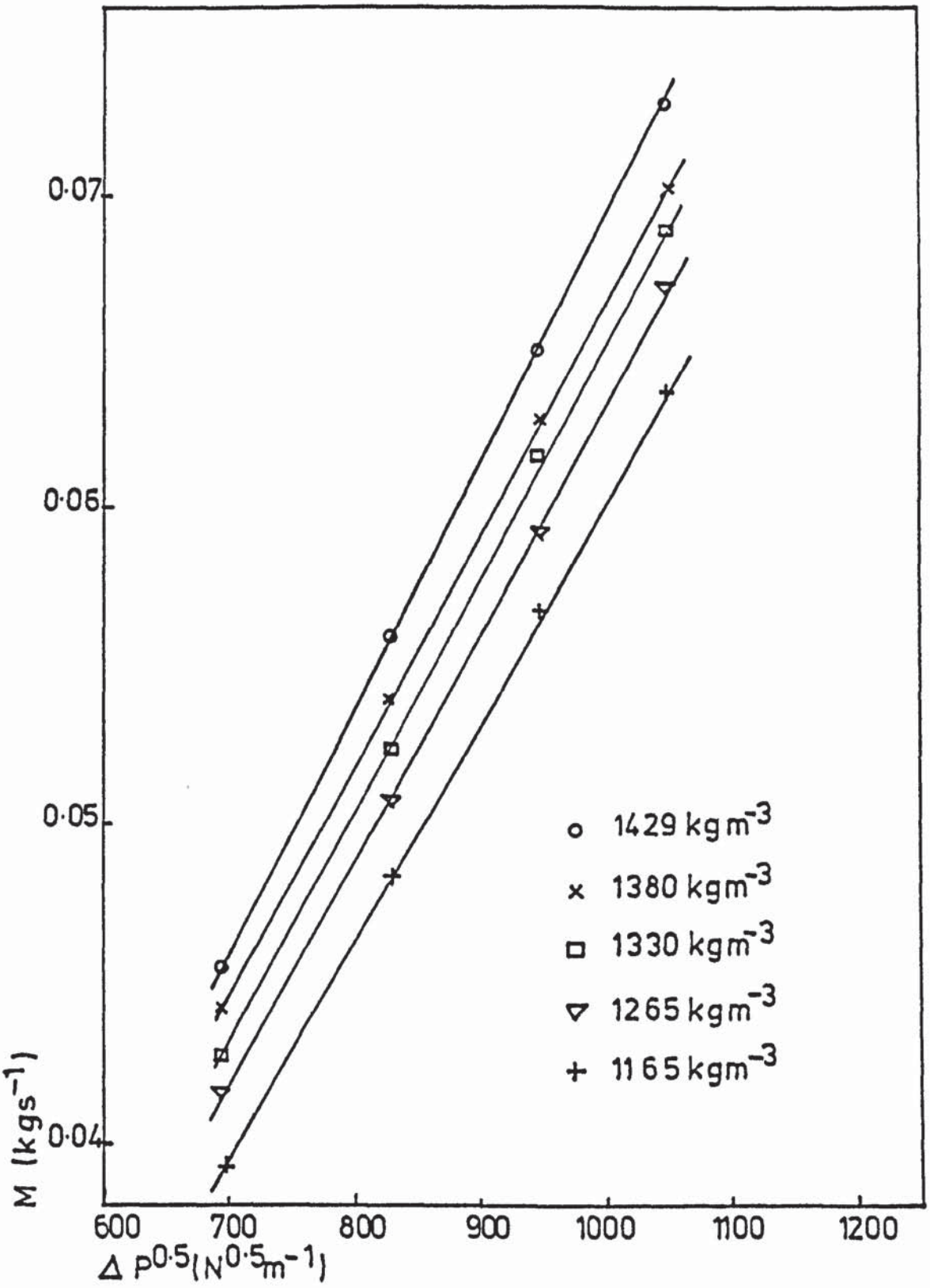

FIGURE 6:19 VARIATION OF SLURRY FLOWRATE WITH SQUARE ROOT OF NOZZLE PRESSURE (NOZZLE SF)

Values of C_d calculated from Figures 6.16 to 6.19 varied within the range 0.3 to 0.4 and were fairly constant for each nozzle irrespective of operating variables. These values are of similar magnitude to those reported by Fraser et al. (102) for plug type swirl nozzles.

The main objective of the mathematical model was to predict values of mean drop size and no reference has been made to the actual drop size distribution. Typical distributions are presented in Figures 6.20 and 6.21 and represents data obtained from extremes of operating conditions. Thus the smallest and largest nozzles operating with the high and low density slurries at 483 and 1103 kN/m^2 are compared. No attempt has been made to correlate the data with any distribution law but the curves indicate a trend to the square root normal distribution. This is in agreement with various other workers who have found swirl nozzles to produce this type of drop size distribution. Figure 6.22 further illustrates the fit to the square root normal distribution with a plot of the square root of the drop diameter against cumulative volume percentage undersize or normal probability paper. However closer agreement is found with nozzle SC which produces a finer spray, an observation which has been similarly reported elsewhere (99).

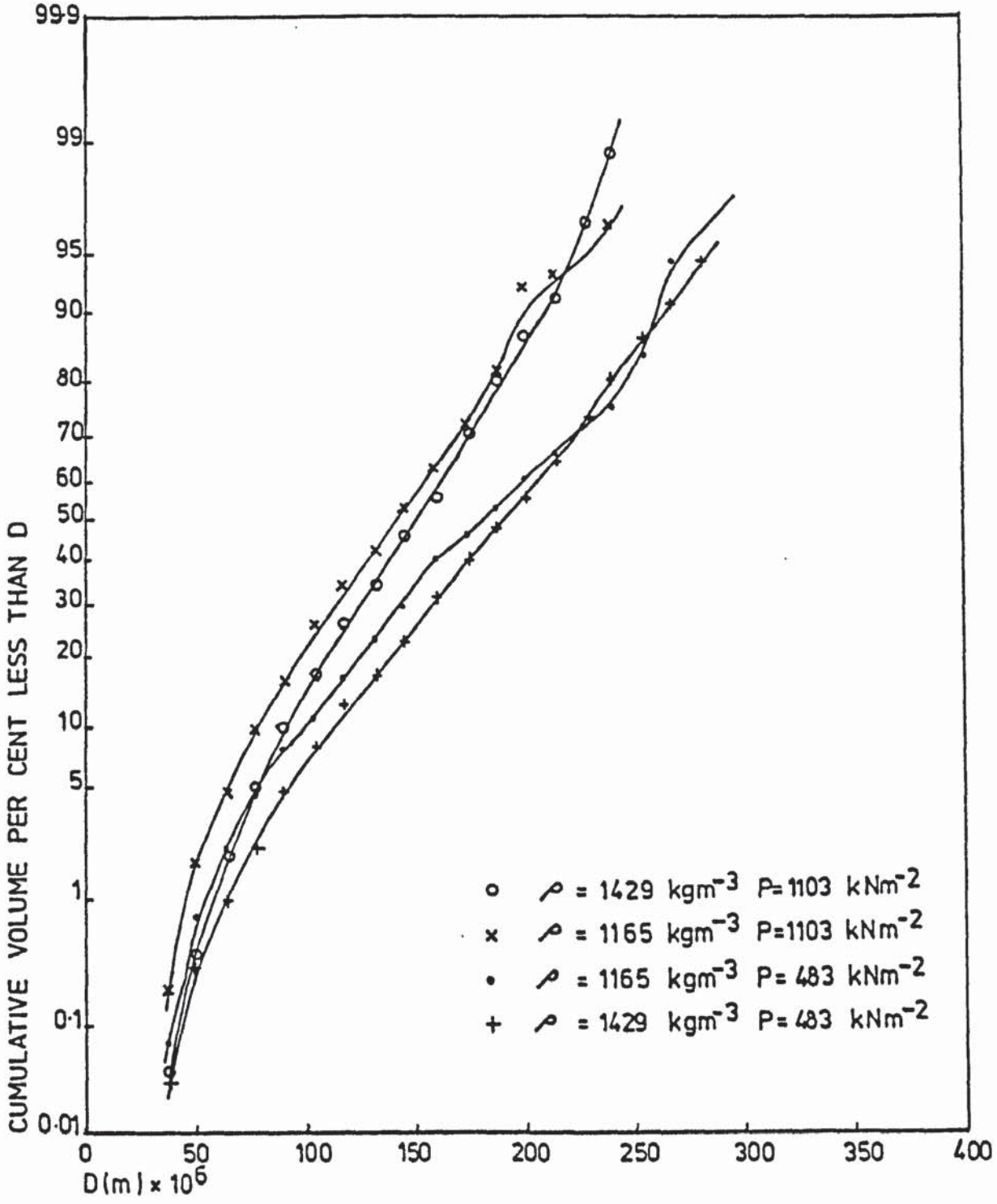

FIGURE 6:20 DROP SIZE DISTRIBUTION (NOZZLE SC)

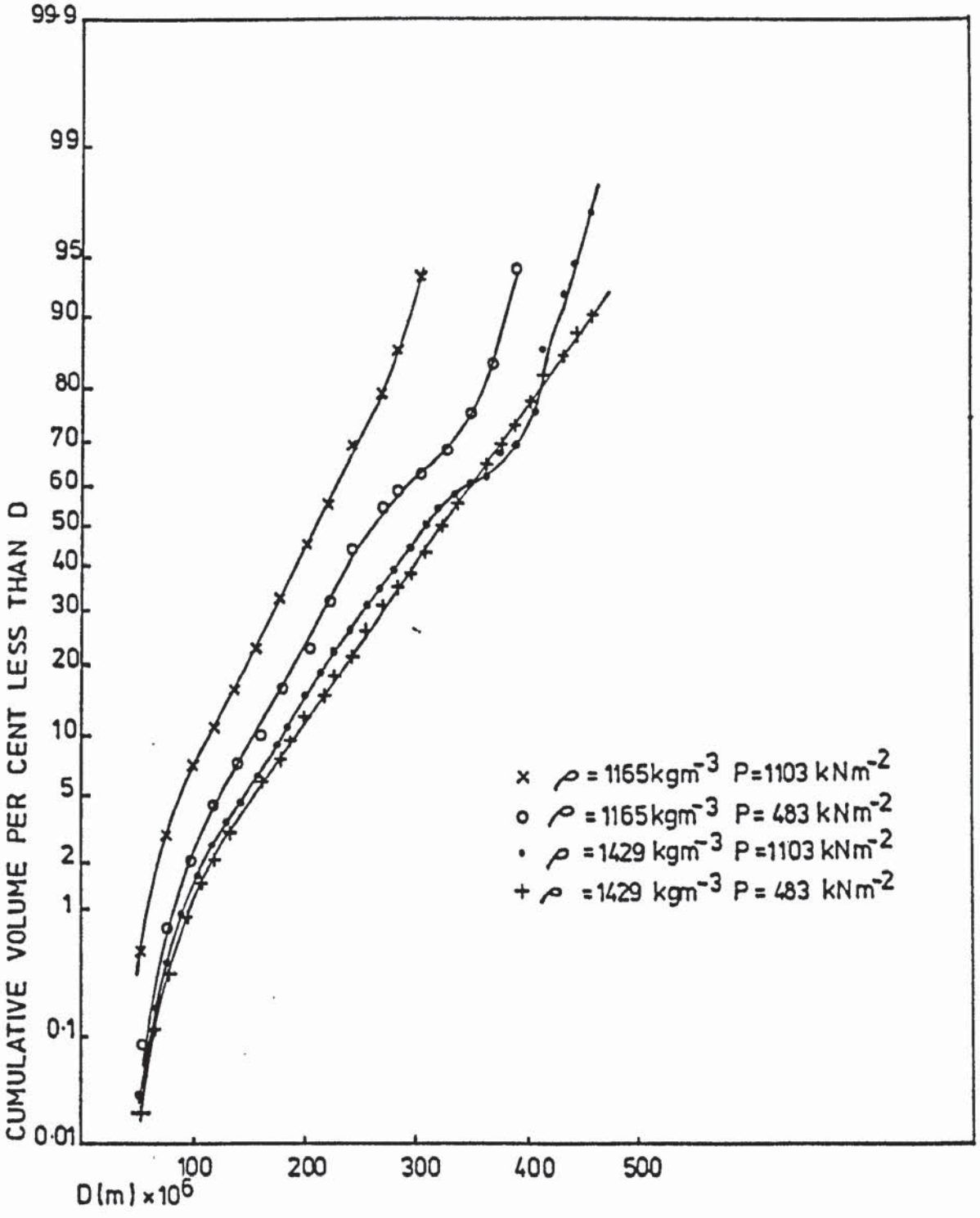

FIGURE 6.21 DROP SIZE DISTRIBUTION (NOZZLE SF)

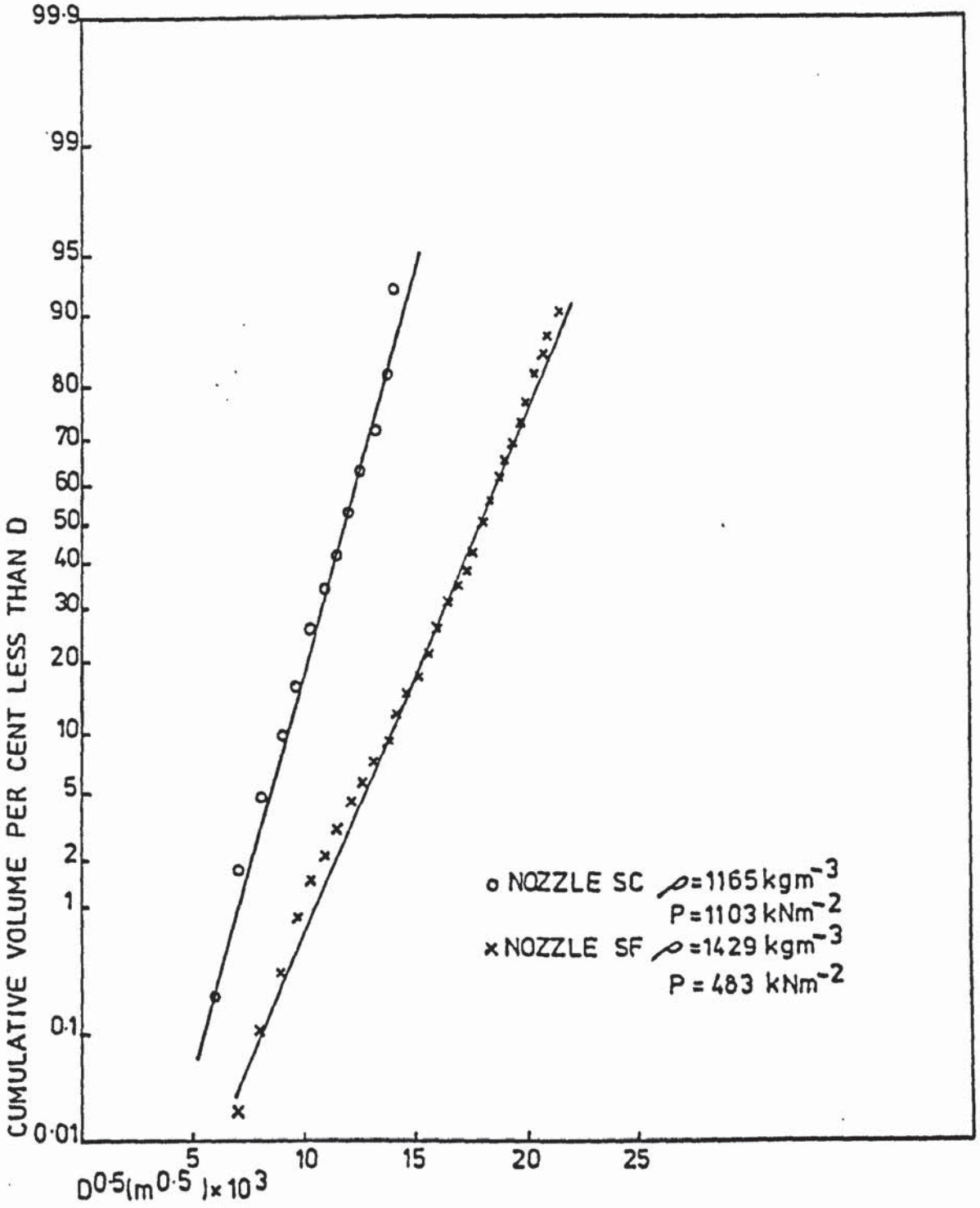

FIGURE 6.22 SQUARE ROOT NORMAL DISTRIBUTIONS

CONCLUSIONS

1) This work is an initial investigation into the spraying of slurries and appears to be unique.

2) The experimental procedure appears to be sound and the high speed photographic technique for drop measurement was confirmed by the Knollenburg apparatus with good agreement.

3) High speed photographs of sheet break-up and drop formation indicate that drops are formed through the formation of ligaments which subsequently break down to form drops through Rayleigh type disturbances.

4) The model to predict flow through the nozzle is an extension of Taylor's derivation which specifically applies to conical swirl chambers. The model presented here is applicable to any nozzle irrespective of shape of the swirl chamber. This has necessitated expressing the model in terms of Cartesian co-ordinates, but the final equation can be solved numerically.

5) The model predicted that when the viscosity of the fluid exceeded about 0.03 Nsm^{-2} all of the fluid passed through the boundary layer and the boundary layer can be predicted. This enabled the sheet velocities to be evaluated accurately and with further analysis obtained a realistic estimate of the drop size.

RECOMMENDATIONS FOR FURTHER WORK

1) Higher atomising pressures.

2) Extend the work to different materials exhibiting more pronounced non-Newtonian properties.

3) To embrace non-Newtonian behaviour into the modelling.

4) In an actual spray drying operation, very high rates of mass transfer accompany the formation of drops and to date no work has embraced this process.

NOMENCLATURE

a	radius of jet
A	dimensionless parameter = $1 - \alpha/(\alpha^{3/2})^{0.5}$
	parameter in equation (3.56) = A_s/A_o
A_o	area of orifice
A_s	area of inlet swirl channel
A_T	total flow area at orifice
C	parameter in Rosin-Rammler equation
	dimensionless parameter = $\frac{C_{do}C_h}{C_{d_I}}$
C_D	discharge coefficient
C_{do}	discharge coefficient at outlet orifice
C_{d_I}	discharge coefficient at inlet orifice
C_h	discharge coefficient of hollow cone
C_p	specific heat capacity
C_T	crust thickness
d	diameter of jet
D	droplet diameter
D_{vso}	volume median diameter
d_I	inlet orifice diameter
d_o	outlet orifice diameter
d_m	mean diameter of inlet vortex in swirl chamber
D_G	dimensionless group = $P/(\rho V_s^2)$
D_V	molecular diffusivity
d_L	ligament diameter
F'	correction factor
g	gravity

h	sheet thickness
h^*	sheet thickness at break-up
h_c	heat transfer coefficient
H	total pressure head
h'	pressure head
k	thermal conductivity
K_T	sheet thickness parameter
K_G	mass transfer coefficient
K_c	crust mass transfer coefficient
K_o	constant
L	break-up length
L_o	orifice length
m	mass
Nu	Nusselt number (hcD/k)
n	dimensionless length = $(R-r)/\delta$
N	number of droplets in size group
OL	Ohnesorge number ($\mu/(\rho d\sigma)^{0.5}$)
P	pressure
P_o	porosity
Pr	Prandtl number ($Cp\mu/k$)
q	amplitude
q^*	amplitude at break-up
q_o	initial amplitude
Q	flowrate
r	distance
r_1	radius of curvature
R	distance of nozzle wall from axis r = 0
R_3	length of side of conical swirl chamber

R_e Reynolds number ($DV\rho/\mu$)

r_m mean swirl radius at inlet

R_s radius swirl chamber

R_o orifice radius

r_{AC} radius of air core

R_I radius of inlet channel to swirl chamber

R_D dimensionless distance = r/R_3

S_w width of swirl chamber inlet

S_D depth of inlet swirl channel

S_N number standard deviation

S_h Sherwood number (KgD/D_v)

S_c Schmidt number ($\mu/D_v\rho_a$)

S_G geometric standard deviation

t time

T_a air temperature

T_p droplet temperature

T thrust exerted

U relative velocity

U_T velocity equivalent to total pressure head

V velocity

V_s sheet velocity

V_I inlet velocity to swirl chamber

v tangential velocity component

v_r radial velocity component

v_z axial velocity component

V_A axial velocity at orifice = $\dfrac{\int_{r_{ac}}^{R_o} 2v_z r dr}{(R_o^2 - r_{ac}^2)}$

V_{RA} resultant velocity based on V_A and V_T

V_T tangential velocity at orifice = $\int_{r_{ac}}^{R_o} \frac{2v_\theta r dr}{(R_o^2 - r_{ac}^2)}$

W streaming velocity

z axial distance

Greek Letters

α Dimensionless parameter = $(1-r_{ac}^2/R_o^2)$

angle of conical swirl chamber

β growth rate

γ dimensionless variable = $(\mu\rho a^3/\sigma)$

δ boundary layer thickness

Δ' nozzle parameter $(A_s/d_o d_m)$

ε temporal amplification factor

η wavenumber $(2\pi/\lambda)$

θ semi-cone angle

λ wavelength

λ_{opt} wavelength of disintegrating disturbance

μ viscosity

ν kinematic viscosity

π constant = 3.141

ρ density

σ surface tension

τ relaxation time

ψ coefficient in Froessling equation

χ dimensionless parameter (equation 3.62)

Ω circulation constant

Subscripts

L	liquid
a	gas
S	solid

REFERENCES

1. Masters, K. Spray Drying, Leonard Hill (1972).
2. Kim, K.Y., Marshall, W.R. A.I.Ch.E.J. (1971), 17, (N3), 575.
3. Nukiyama, S., Tanasawa, Y. Trans. Soc. Mech. Engrs. Japan (1937), 4, (N14), 86.
4. Dombrowski, N., Hasson, D., Ward, D.E. Ch.E. Sci. (1960) 12, 35.
5. Lapple, C.E., Shepherd, C.B. Ind. Eng. Chem. (1940), 32, (N5), 605.
6. Masters, K., Brit. Chem. Eng. (1968), 13, (N1), 88, 242.
7. Gretzinger, J., Marshall, W.R. A.I.Ch.E.J. (1961) 7, 312.
8. Friedman, S.J., Gluckert, F.A., Marshall, W.R. Chem. Eng. Prog. (1952), 48, 181.
9. Bailey, G.H., Slater, I.W., Eisenklam, F. Brit. Chem. Eng. (1970) 15, (N7), 912.
10. Gluckert, F.A. A.I.Ch.E.J. (1962), 8, (N3), 460.
11. Katta, S., Gauvin, W.H. A.I.Ch.E.J. (1975), 21, 143.
12. Chaloud, J.H., Martin, J.B., Baker, J.S. Chem. Eng. Prog. (1957), 53, 593.
13. Paris, J.R., Ross, P.N., Dastur, S.P., Morris, R.L. Ind. Eng. Chem. Proc. Des. Dev. (1971), 10, (N2), 157.
14. Gauvin, W.H. Int. J. of Multi-phase Flow (1975), 1, 793.

15. Ade-John, A.O., Jeffreys, G.V. Trans. I.Chem.E., (1978), 56, 36.

16. Benatt, F.G.S., Eisenklam, P., J. Inst. Fuel (1969), 42, 309.

17. Frossling, N., Beitr. Geophys., (1938), 52, 170.

18. Ranz, W.E., Marshall, W.R., Chem. Eng. Prog (1952), 48, 141.

19. Bose, A.K., Pei, D.C.T., Can. J. Chem. Eng. (1964), 42, (N6), 259.

20. Dickinson, D.R., Marshall, W.R., A.I.Ch.E.J. (1960), 14, (N4), 541.

21. Pham, Q.T., Keey, R.B. Trans. I.Chem.E. (1977), 55, (N2), 114.

22. Charlesworth, D.M., Marshall, W.R., A.I.Ch.E.J. (1960), 6, (N1), 9.

23. Duffie, J.A., Marshall, W.R., Chem. Eng. Prog. (1953), 49, 417 and 480.

24. Audu, T.O.K., Jeffreys, G.V., Trans. I.Chem.E. (1975), 53, 165.

25. Dlouhy, J., Gauvin, W.H., A.I.Ch.E.J. (1960), 6, 29.

26. Baltas, L., Gauvin, W.H., Pulp and Paper RI of Canada Tech. Report 518, 519 (1967).

27. Crosby, E.J., Marshall, W.R. Chem. Eng. Prog (1958), 54, (N7), 56.

28. Dombrowski, N., Fraser, R.P. Phil. Trans. R. Soc (1953), 247A, 101.

29. Fraser, R.P., Dombrowski, N., Eisenklam, P. Nature (1954), 173, 145.

30. Dombrowski, N., Hooper, P.C. Chem. Eng. Sci. (1962), 17, 291.

31. Colbourn, A.J., Heath, H.H. NGTE Memo No. M86 (1950).

32. Taylor, G.I. Proc. R. Soc. (1959) A253, 259.

33. Clark, C.J., Dombrowski, N. J. Fluid Mech (1974), 64, (N1), 167.

34. Weber, C. Z. Angew Math. Mech. (1931), 11, 136.

35. Fraser., R.P. Eisenklam, P., Dombrowski, N., Hasson, D. A.I.Ch.E.J. (1962), 8, 672.

36. Briffa, F., Dombrowski, N. A.I.Ch.E.J. (1966), 12, 708.

37. Squire, H.B. Br.J. App. Phys. (1953), 4, 167.

38. Lamb, H., Hydrodynamics, 5th ed, Chapter 9, Cambridge University Press (1932).

39. Hagerty, W.W., Shea, J.F., J. Appl. Mech. (1955), 22, 509.

40. Dombrowski, N., Johns, W.R. Chem. Eng. Sci (1963), 18, 203.

41. Gordon, G.D., J. Appl. Phys. (1959), 30, 1759.

42. Clark, C.J., Dombrowski, N. Proc. Royal Soc. (1972), A329, 467.

43. Crapper, G.D., Dombrowski, N., Jepson, W.P., Pyott, G.A.D. J. Fluid Mech. (1973), 57, 671.

44. Crapper, G.D., Dombrowski, N., Pyott, G.A.D. Proc. Royal Soc. (1975), A342, 209.

45. Crapper, G.D., Dombrowski, N., Jepson, W.P. Proc. Royal Soc. (1975), A342, 225.

46. Weihs, D., J. Fluid Mech. (1978), 87, (N2), 289.

47. Dombrowski, N., Munday, G. Biochemical and Biological Engineering Sci., Academic Press, (1968), 2, Chapter 16.

48. Garner, F.H., Nissan, A.H., Woods, G.F., Phil. Trans. Royal Soc. (1950), 243A, 37.

49. Dombrowski, N., Eisenklam, P., Fraser, R.P. J. Inst. Fuel (1957), 30, 399, 413.

50. Courshee, R.J., Valentine, R.W. J. Agric. Eng. Res. (1959), 4, 62.

51. Savart, F. Ann. Chem. (1833), 53, 337.

52. Rayleigh, Lond. Proc. Land. Math. Soc. (1878), 10, 4.

53. Castleman, R.A. U.S. Bureau Stds. J. Res. (1931), 6, 369.

54. Rayleigh, Lord. Phil. Mag. (1892), 34, 145.

55. Smith, S.W.J., Moss, H. Proc. Royal Soc. A. (1916), 93, 373.

56. Haenlein, A. NACA, Tech. Memo No. 659 (1932).

57. Tyler, E., Richardson, E.G. Proc. Phys. Soc. (1925), 37, 279.

58. Grant, R.P., Middleman, S. A.I.Ch.E.J. (1966), 12, 669.

59. Phinney, R.E. A.I.Ch.E.J. (1972), 18, (N2), 432.

60. Levich, V., Physicochemical Hydrodynamics, Prentice-Hall, NJ (1962).

61. Chen, T.F., Davis, J.R., Proc. ASCE. Hyd. Div. (1964), 90, 175.

62. Phinney, R.E., Physics of Fluids (1973), 16, (N2), 193.

63. Fenn, R.W., Middleman, S. A.I.Ch.E.J. (1969), 15, 379.

64. Rupe, J.H. Jet Prpulsion Lab, Pasadena, California Tech. Report No. 52.207, Jan (1962).

65. Eisenklam, P., Hooper, P.C. Min of Supply DGGW Report EMR/58/JRL/42 (1958).

66. Phinney, R.E., J. Fluid Mech. (1973), 60, (N4), 689.

67. Tanasawa, Y., Tojoda, S. Trans. Jap. Soc. Mech. Eng. (1954), 20, 306.

68. Ivanov, V.A. J. Appl. Mech. Tech. Phys. USSR, (1966), 7, 19.

69. Lee, D.W., Spencer, R.C., NACA Tech Report 454 (1933).

70. Ohnesorge, W. Z. Angew Math. Mech (1936), 16, 355.

71. Miesse, C.C. Ind. Eng. Chem. (1955), 47, 1690.

72. McCarthy, M.J., Molloy, N.A. Chem. Eng. J. (1974), 7, 1.

73. Sakai, T., Kito, M., Sato, M., Saito, M. J. Inst. Fuel (1976), 49, 398, 25.

74. Wang, D.P., J. Fluid Mech. (1968), 34, 299.

75. Donnelly, R.J., Glaberson, W. Proc. Royal Soc. A. (1966), 290, 547.

76. Yuen, M. J. Fluid Mech. (1968), 33, 181.

77. Rutland, D.F., Jameson, G.J. J. Fluid Mech. (1971), 46, 267.

78. Roth, L.O., Porterfield, J.G. Trans. A.S.A.E. (1970), 13, 16, 779.

79. Goldin, M., Yerushalmi, J., Pfeffer, R., Shinnar, R. J. Fluid Mech. (1969), 38, 689.

80. Goldin, M., Pfeffer, R., Shinnar, R. Chem. Eng. J. (1972), 4, 8.

81. Kroesser, F.W., Middleman, S. A.I.Ch.E.J. (1969), 15, 383.

82. Gordon, M., Yerushalmi, J., Shinnar, R. Trans. Soc. Rheology, (1973), 17, (N2), 303.

83. Tanasawa, Y., Kobayasi, K. Technology Rep. Tohoku Univ. (1955), 20, 27.

84. Marshall, W.R., A.I.Ch.E.J. Monograph Series No.2, NY (1954).

85. Novikov, I.I. J. Tech. Phys. (1948), 3, 345.

86. Ambrovitch, G.N. Industrial Aerodynamics TSAG (1944), 18.

87. Doumas, M., Laster, R. Chem. Eng. Prog (1953), 49, 518.

88. Harvey, J.F., Hermandorfer, H.W. Trans. Soc. Naval Architects and Marine Engrs. (1943), 51, 61.

89. Taylor, G.I., Quart J. Mech. and Appl. Math. (1950), 3, 129.

90. Hodgkinson, T.G. Porton Tech. Rep. No.191 (1950).

91. McIrvine, J.D. Ph.D. Thesis, Univ. of Wisconsin, (1957).

92. Dombrowski, N., Hasson, D. A.I.Ch.E.J. (1969), 15, (N4), 604.

93. Taylor, G.I. Proc. 7th Int. Cong. Appl. Mech. (1948), 2, 280.

94. Joyce, J.R., J. Inst. Fuel (1949), 22, 150.

95. Rosin, P., Rammler, E. J. Inst. Fuel. (1933), 7, 29.

96. Mugele, R.A., Evans, H.D. Ind. Eng. Chem. (1951), 43, 1317.

97. Kottler, E. J. Franklin Inst. (1950), 250, 339, 419.

98. Tate, R.W., Marshall, W.R. Chem. Eng. Prog. (1953), 49, 169, 226.

99. Dombrowski, N., Wolfsohn, D.L. Trans. Inst. Chem. Eng. (1972), 50, 259.

100. Nelson, P.A., Stevens, W.F. A.I.Ch.E.J. (1961), 7, 80.

101. Goering, C.E., Smith, D.M. Am. Soc. Agric. Eng. (1976), Winter Meeting.

102. Fraser, R.P., Eisenklam, P., Dombrowski, N. Brit. Chem. Eng. (1957), 2, (414), and 536.

103. Longwell, J.P. DSc Thesis, Mass. Inst. Tech. (1943).

104. Lewis, H.C., Edwards, D.G., Goglia, M.H., Rice, R.I., Smith, L.W. Ind. Eng. Chem. (1948), 40, 67.

105. Straus, R. Ph.D. Thesis, Univ. of London (1949).

106. Weinburg, S. Proc. Inst. Mech. Eng. (1952), 18, 240.

107. Darnell, W.H. Ph.D. Thesis, Univ. of Wisconsin (1953).

108. Turner, G.M., Moulton, R.W. Chem. Eng. Prog. (1953), 49, 185.

109. Radcliffe, A. Proc. Inst. Mech. Engrs. (1955), 169, 93.

110. Encyclopedia Chem. Technol. 2nd ed. Kirk-Othma (1969), 18, 634.

111. Wang, K., Tien, C. Ind. Eng. Chem. Proc. Des. Dev. (1972), 11, (N2), 169.

112. Dombrowski, N., Tahir, M.A. J. Inst. Fuel (1977), 50, 403, 59.

113. El-Awady, M.N. Trans. Am. Soc. Agric. Eng. (1978), 21, (N1), 70.

114. Mani, J.V.S. Indian J. Technol. (1969), 7, (N10), 333.

115. Simmons, H.C. J. Eng. Power Trans ASME (1977), July, 309.

116. Binnie, A.M., Hookings, G.A. Proc. Royal Soc. A. (1948), 194, 398.

117. Wolfsohn, D.L. Ph.D. Thesis, Univ. of Leeds (1970).

118. Hasson, D., Mizrahi, J. Trans. Inst. Chem. Eng. (1961), 39, 415.

119. Taylor, E.H., Harmon, D.B. Ind. Eng. Chem. (1954), 46, 1455.

120. Tate, R.W., Olson, E.O. Techniques for measuring drop sizes in sprays, Delavan Manuf. Co. Ltd. (1964).

121. Choudhury, A.P.R. Ph.D. Thesis, North Western Univ. Evanston 16 (1955).

122. Binark, H., Ranz, W.E. Ind. Eng. Chem. (1959), 51, 701.

123. Clark, C.J., Dombrowski, N. J. Aerosol Sci. (1973), 4, 27.

124. Dombrowski, N., Wolfsohn, D.L. J. Aerosol Sci. (1971), 2, 405.

125. Davies, C., Paper presented at High Speed Photography Conference (1977).

126. Private communication with Unilever Research, Port Sunlight (1977).

Appendix I

Drop Size Distribution Data

SLURRY 23% NOZZLE SC

ΔP	(kNm^{-2})	483	690	896	1103
ΔD	D_m	N	N	N	N
43.5	36.8	15	14	11	37
57.3	50.4	53	72	74	107
70.9	64.0	55	84	90	108
84.4	77.5	50	92	88	93
98.0	91.4	48	83	82	80
111.6	105.0	29	73	56	78
125.4	118.5	35	48	59	48
139.0	132.1	30	46	43	31
152.6	145.7	21	39	29	34
166.2	159.5	27	34	31	22
179.8	174.6	11	18	23	15
193.6	186.7	12	20	26	15
207.2	200.2	9	19	9	12
220.7	213.8	7	5	6	1
234.3	227.7	5	4	5	1
247.9	241.2	2	3	3	1
261.7	254.8	6	5	1	2
275.3	268.4	5	1	1	
288.9	282.0	0			
302.7	295.8	1			
316.0	309.4	1			
329.5	322.9				
343.5	336.5				
357.0	350.1				
$\frac{\Sigma ND^3}{\Sigma ND^2}$		164	146	143	131

SLURRY 35% NOZZLE SC

ΔP	(kNm^{-2})	483	690	896	1103
ΔD	D_m	N	N	N	N
43.5	36.8	21	22	20	14
57.3	50.4	23	49	42	61
70.9	64.0	33	60	62	65
84.4	77.5	37	51	62	77
98.0	91.4	37	54	71	107
111.6	105.0	32	48	49	71
125.4	118.5	27	46	34	67
139.0	132.1	26	32	38	36
152.6	145.7	20	23	30	35
166.2	159.5	28	16	29	22
179.8	174.6	19	17	17	10
193.6	186.7	12	14	12	12
207.2	200.2	10	8	7	4
220.7	213.8	8	7	4	3
234.3	227.7	12	6	4	1
247.9	241.2	2	5	1	1
261.7	254.8	6	2	1	1
275.3	268.4	0	0	0	
288.9	282.0	2	2	0	
302.7	295.8	1		1	
316.0	309.4	0			
329.5	322.9	1			
343.5	336.5	1			
357.0	350.1				
$\frac{\Sigma ND^3}{\Sigma ND^2}$		175	152	142	128

SLURRY 40% NOZZLE SC

ΔP	(kNm^{-2})	483	690	896	1103
ΔD	D_m	N	N	N	N
43.5	36.8	21	18	28	24
57.3	50.4	44	54	79	73
70.9	64.0	55	57	82	92
84.4	77.5	55	50	95	98
98.0	91.4	61	71	77	68
111.6	105.0	58	58	89	67
125.4	118.5	54	50	70	59
139.0	132.1	34	33	42	38
152.6	145.7	30	46	36	31
166.2	159.5	37	17	36	46
179.8	174.6	24	13	22	20
193.6	186.7	20	19	16	11
207.2	200.2	15	15	14	11
220.7	213.8	12	10	7	5
234.3	227.7	11	7	5	2
247.9	241.2	9	7	4	1
261.7	254.8	3	2		0
275.3	268.4	2	2		1
288.9	282.0	2	0		2
302.7	295.8	1	1		
316.0	309.4	1			
329.5	322.9	1			
343.5	336.5				
357.0	350.1				
$\frac{\Sigma ND^3}{\Sigma ND^2}$		167	156	140	139

SLURRY 45% NOZZLE SC

ΔP	(kNm^{-2})	483	690	896	1103
ΔD	D_m	N	N	N	N
43.5	36.8	3	4	7	11
57.3	50.4	26	22	46	55
70.9	64.0	47	38	71	68
84.4	77.5	49	52	85	96
98.0	91.4	41	58	87	62
111.6	105.0	53	75	85	100
125.4	118.5	45	51	74	80
139.0	132.1	46	49	51	49
152.6	145.7	33	42	39	49
166.2	159.5	31	24	38	39
179.8	174.6	27	32	18	15
193.6	186.7	28	29	9	12
207.2	200.2	25	21	10	14
220.7	213.8	24	18	6	3
234.3	227.7	9	9	4	4
247.9	241.2	8	3	0	3
261.7	254.8	2	2	2	1
275.3	268.4	1	1	0	
288.9	282.0	1	0	1	
302.7	295.8	2	0	1	
316.0	309.4	2	1	1	
329.5	322.9				
343.5	336.5				
357.0	350.1				
$\frac{\Sigma ND^3}{\Sigma ND^2}$		171	161	142	138

SLURRY 50% NOZZLE SC

ΔP	(kNm^{-2})	483	690	896	1103
ΔD	D_m	N	N	N	N
43.5	36.8	12	7	11	10
57.3	50.4	43	18	31	37
70.9	64.0	47	52	64	77
84.4	77.5	51	46	74	86
98.0	91.4	64	58	90	93
111.6	105.0	57	66	92	84
125.4	118.5	53	38	51	71
139.0	132.1	37	41	53	50
152.6	145.7	36	30	44	53
166.2	159.5	44	36	30	32
179.8	174.6	29	19	21	39
193.6	186.7	23	12	22	21
207.2	200.2	20	16	15	10
220.7	213.8	18	8	8	6
234.3	227.7	15	6	12	6
247.9	241.2	9	3	2	2
261.7	254.8	7	3	0	1
275.3	268.4	4	1	1	
288.9	282.0	3	2	0	
302.7	295.8	3	1	1	
316.0	309.4	1		1	
329.5	322.9				
343.5	336.5				
357.0	350.1				
$\frac{\Sigma ND^3}{\Sigma ND^2}$		175	158	150	143

SLURRY 23% NOZZLE SD

$\Delta P\ (kNm^{-2})$		483	690	896	1103
ΔD	D_M	N	N	N	N
66.7	56.5	29	34	40	33
87.9	77.3	73	90	70	82
108.8	98.2	82	88	87	78
129.5	118.9	73	77	71	80
150.3	140.2	71	75	51	68
171.2	161.1	75	61	54	69
192.4	181.8	52	32	35	39
213.2	202.7	44	25	28	20
234.1	223.5	28	30	12	20
255.0	244.7	25	16	7	15
275.8	267.9	30	13	11	3
297.0	286.4	16	8	5	2
317.9	307.1	8	9	6	0
338.6	328.0	10	4	2	2
359.4	349.3	8	1	0	
380.3	370.0	5	0	2	
401.5	390.9	6	0		
422.3	411.8	3	1		
443.2	432.6	0			
464.4	453.8	0			
484.8	474.6	0			
505.5	495.4	1			
527.0	516.2				
547.7	537.1				
$\frac{\Sigma ND^3}{\Sigma ND^2}$		234	198	189	168

SLURRY 35% NOZZLE SD

$\Delta P\ (kNm^{-2})$		483	690	896	1103
ΔD	D_M	N	N	N	N
66.7	56.5	0	1	7	20
87.9	77.3	12	30	26	56
108.8	98.2	42	56	47	79
129.5	118.9	53	66	66	74
150.3	140.2	59	73	72	60
171.2	161.1	66	59	45	46
192.4	181.8	51	46	37	44
213.2	202.7	45	30	18	23
234.1	223.5	32	36	16	9
255.0	244.7	14	16	15	9
275.8	267.9	16	7	10	7
297.0	286.4	14	5	4	3
317.9	307.1	5	10	4	1
338.6	328.0	4	2	1	3
359.4	349.3	3	1		
380.3	370.0	0	1		
401.5	390.9	2			
422.3	411.8				
443.2	432.6				
464.4	453.8				
484.8	474.6				
505.5	495.4				
527.0	516.2				
547.7	537.1				
$\frac{\Sigma ND^3}{\Sigma ND^2}$		214	200	189	177

SLURRY 40% NOZZLE SD

$\Delta P\ (kNm^{-2})$		483	690	896	1103
ΔD	D_M	N	N	N	N
66.7	56.5	0	0	0	1
87.9	77.3	8	3	12	7
108.8	98.2	44	27	27	49
129.5	118.9	76	44	54	91
150.3	140.2	49	68	71	74
171.2	161.1	56	58	64	88
192.4	181.8	33	45	55	66
213.2	202.7	29	31	32	41
234.1	223.5	24	22	21	29
255.0	244.7	19	13	12	12
275.8	267.9	9	13	14	11
297.0	286.4	9	4	4	6
317.9	307.1	7	5	2	1
338.6	328.0	7	0	2	1
359.4	349.3	0	1		
380.3	370.0	1			
401.5	390.9				
422.3	411.8				
443.2	432.6				
464.4	453.8				
484.8	474.6				
505.5	495.4				
527.0	516.2				
547.7	537.1				
$\frac{\Sigma ND^3}{\Sigma ND^2}$		210	198	193	186

SLURRY 45% NOZZLE SD

$\Delta P\ (kNm^{-2})$		483	690	896	1103
ΔD	D_M	N	N	N	N
66.7	56.5	5	3	2	3
87.9	77.3	32	46	31	68
108.8	98.2	47	57	65	96
129.5	118.9	56	66	84	104
150.3	140.2	61	65	84	109
171.2	161.1	50	50	64	67
192.4	181.8	51	38	33	41
213.2	202.7	29	27	30	32
234.1	223.5	19	19	33	18
255.0	244.7	14	19	14	18
275.8	267.9	17	19	10	7
297.0	286.4	15	4	7	3
317.9	307.1	5	8	5	3
338.6	328.0	4	1	1	1
359.4	349.3	4	3	1	
380.3	370.0	2	0	1	
401.5	390.9	1	0		
422.3	411.8	1	1		
443.2	432.6	1			
464.4	453.8				
484.8	474.6				
505.5	495.4				
527.0	516.2				
547.7	537.1				
$\frac{\Sigma ND^3}{\Sigma ND^2}$		222	206	193	175

SLURRY 50% NOZZLE SD

ΔP (kNm^{-2})		483	690	896	1103
ΔD	D_m	N	N	N	N
43.5	36.8	8	14	21	17
57.3	50.4	27	26	25	36
70.9	64.0	40	37	43	43
84.4	77.5	47	52	48	73
98.0	91.4	36	49	48	61
111.6	105.0	30	41	43	72
125.4	118.5	32	40	39	50
139.0	132.1	33	43	45	57
152.6	145.7	33	38	49	34
166.2	159.5	31	40	47	40
179.8	174.6	31	36	30	45
193.6	186.7	14	29	37	28
207.2	200.2	15	13	21	25
220.7	213.8	14	13	19	14
234.3	227.7	13	21	20	15
247.9	241.2	10	15	9	3
261.7	254.8	8	11	7	11
275.3	268.4	12	8	7	6
288.9	282.0	3	2	4	7
302.7	295.8	4	1	3	6
316.0	309.4	4	5	5	1
329.5	322.9	2	3	1	3
343.5	336.5	3	1	1	0
357.0	350.1	3	1		1
370.6	364.0	2	0		
384.2	377.5	1	1		
398.0	391.1	0			
411.6	404.7	1			
425.2	418.3				
439.0	432.1				
452.3	445.7				
466.2	459.3				
479.8	472.8				
493.3	486.4				
506.9	500.2				
$\frac{\Sigma ND^3}{\Sigma ND^2}$		214	195	188	184

SLURRY 23% NOZZLE SE

$\Delta P\ (kNm^{-2})$		483	690	896	1103
ΔD	D_M	N	N	N	N
66.7	56.5	5	12	10	10
87.9	77.3	19	48	55	51
108.8	98.2	42	62	83	82
129.5	118.9	40	46	68	71
150.3	140.2	39	48	62	76
171.2	161.1	37	39	52	41
192.4	181.8	41	32	32	41
213.2	202.7	27	24	42	29
234.1	223.5	17	14	22	20
255.0	244.7	23	11	21	10
275.8	267.9	19	12	6	4
297.0	286.4	10	8	10	3
317.9	307.1	5	6	4	1
338.6	328.0	9	1	4	0
359.4	349.3	4	6	1	1
380.3	370.0	6			
401.5	390.9	3			
422.3	411.8	0			
443.2	432.6	0			
464.4	453.8	1			
484.8	474.6				
505.5	495.4				
527.0	516.2				
547.7	537.1				
$\frac{\Sigma ND^3}{\Sigma ND^2}$		243	207	196	175

SLURRY 35% NOZZLE SE

ΔP (kNm^{-2})		483	690	896	1103
ΔD	D_M	N	N	N	N
66.7	56.5	1	8	12	9
87.9	77.3	37	26	69	87
108.8	98.2	57	42	72	105
129.5	118.9	54	35	75	91
150.3	140.2	38	48	73	90
171.2	161.1	30	36	55	63
192.4	181.8	28	25	43	41
213.2	202.7	29	20	27	32
234.1	223.5	20	27	24	27
255.0	244.7	10	11	14	12
275.8	267.9	5	9	7	9
297.0	286.4	5	6	7	6
317.9	307.1	4	6	4	1
338.6	328.0	3	4	1	0
359.4	349.3	4	3	5	0
380.3	370.0	1	0	1	1
401.5	390.9	1	0	1	1
422.3	411.8	2	1	0	1
443.2	432.6	2	0	1	
464.4	453.8	1	1		
484.8	474.6				
505.5	495.4				
527.0	516.2				
547.7	537.1				
$\frac{\Sigma ND^3}{\Sigma ND^2}$		230	221	201	183

SLURRY 40% NOZZLE SE

$\Delta P\ (kNm^{-2})$		483	690	896	1103
ΔD	D_M	N	N	N	N
66.7	56.5	1	1	0	4
87.9	77.3	16	19	24	24
108.8	98.2	33	38	37	36
129.5	118.9	42	41	51	52
150.3	140.2	34	50	43	48
171.2	161.1	41	32	35	39
192.4	181.8	38	40	25	38
213.2	202.7	18	29	23	21
234.1	223.5	21	25	16	15
255.0	244.7	14	14	10	8
275.8	267.9	13	17	2	2
297.0	286.4	17	12	5	1
317.9	307.1	11	4	4	2
338.6	328.0	4	2	1	1
359.4	349.3	2	3	1	1
380.3	370.0	1	2		
401.5	390.9	1			
422.3	411.8	2			
443.2	432.6				
464.4	453.8				
484.8	474.6				
505.5	495.4				
527.0	516.2				
547.7	537.1				
$\frac{\Sigma ND^3}{\Sigma ND^2}$		234	218	194	183

SLURRY 45% NOZZLE SE

ΔP (kNm^{-2})		483	690	896	1103
ΔD	D_m	N	N	N	N
69.9	59.1	2	3	12	11
92.1	81.0	16	25	39	35
113.9	102.9	9	43	51	52
135.6	124.6	22	34	47	49
157.5	146.9	26	37	54	69
179.4	168.8	23	34	53	55
201.5	190.4	30	44	44	36
223.4	212.3	21	30	27	31
245.3	234.2	20	18	20	10
267.1	256.3	12	12	15	9
289.0	286.6	10	6	10	5
311.1	300.0	6	7	4	5
333.0	321.8	6	6	1	2
354.7	343.6	3	8	0	0
376.6	365.9	2	0	1	0
398.4	387.6	4	3	1	1
420.6	409.5	0	1		
442.4	431.4	0	1		
464.3	453.2	2			
486.5	475.4	1			
507.9	497.3	2			
$\frac{\Sigma ND^3}{\Sigma ND^2}$		270	234	200	191

SLURRY 50% NOZZLE SE

ΔP (kNm^{-2})		483	690	896	1103
ΔD	D_m	N	N	N	N
43.5	36.8	2	3	3	3
57.3	50.4	21	14	20	18
70.9	64.0	42	36	33	44
84.4	77.5	43	42	53	61
98.0	91.4	48	46	61	57
111.6	105.0	33	36	58	67
125.4	118.5	35	37	34	54
139.0	132.1	21	33	35	31
152.6	145.7	21	29	30	31
166.2	159.5	29	43	30	47
179.8	174.6	20	37	32	51
193.6	186.7	23	35	23	41
207.2	200.2	20	25	26	27
220.7	213.8	22	32	18	30
234.3	227.7	30	25	20	17
247.9	241.2	18	25	14	20
261.7	254.8	4	16	14	7
275.3	268.4	9	13	14	10
288.9	282.0	7	9	17	11
302.7	295.8	9	10	9	11
316.0	309.4	5	7	6	4
329.5	322.9	11	6	4	3
343.5	336.5	4	6	4	4
357.0	350.1	6	6	2	1
370.6	364.0		3	2	0
384.2	377.5		4	2	0
398.0	391.1		3	0	2
411.6	404.7		1	3	1
425.2	418.3		0	0	0
439.0	432.1		1	1	1
452.3	445.7		2	1	
466.2	459.3		0		
479.8	472.8		2		
493.3	486.4				
506.9	500.2				
$\frac{\Sigma ND^3}{\Sigma ND^2}$		284	246	231	211

SLURRY 23% NOZZLE SF

ΔP (kNm^{-2})		483	690	896	1103
ΔD	D_M	N	N	N	N
66.7	56.5	10	12	19	45
87.9	77.3	30	36	53	86
108.8	98.2	33	48	49	70
129.5	118.9	33	36	48	35
150.3	140.2	23	30	36	30
171.2	161.1	15	36	25	29
192.4	181.8	23	33	21	24
213.2	202.7	21	21	18	25
234.1	223.5	19	17	11	15
255.0	244.7	18	12	9	16
275.8	267.9	10	6	4	8
297.0	286.4	7	3	7	5
317.9	307.1	3	9	4	4
338.6	328.0	3	1	3	3
359.4	349.3	4	4	3	
380.3	370.0	4	0	2	
401.5	390.9	4	0	1	
422.3	411.8	2	1		
443.2	432.6		0		
464.4	453.8		1		
484.8	474.6				
505.5	495.4				
527.0	516.2				
547.7	537.1				
$\frac{\Sigma ND^3}{\Sigma ND^2}$		248	218	211	194

SLURRY 35% NOZZLE SF

$\Delta P\ (kNm^{-2})$		483	690	896	1103
ΔD	D_M	N	N	N	N
66.7	56.5	4	1	16	19
87.9	77.3	20	49	63	50
108.8	98.2	40	62	66	86
129.5	118.9	32	57	54	54
150.3	140.2	36	40	55	56
171.2	161.1	33	45	40	41
192.4	181.8	15	32	36	36
213.2	202.7	16	38	22	25
234.1	223.5	20	20	32	25
255.0	244.7	13	15	20	11
275.8	267.9	11	14	18	9
297.0	286.4	8	11	9	6
317.9	307.1	11	4	7	3
338.6	328.0	2	3	4	2
359.4	349.3	14	1	3	1
380.3	370.0	10	0	0	
401.5	390.9	3	1	1	
422.3	411.8	3	1		
443.2	432.6	0	1		
464.4	453.8	2	0		
484.8	474.6	1	0		
505.5	495.4	1	1		
527.0	516.2				
547.7	537.1				
$\frac{\Sigma ND^3}{\Sigma ND^2}$		281	219	212	190

SLURRY 40% NOZZLE SF

$\Delta P\ (kNm^{-2})$		483	690	896	1103
ΔD	D_M	N	N	N	N
66.7	56.5	1	0	4	9
87.9	77.3	31	23	34	47
108.8	98.2	33	28	58	55
129.5	118.9	27	45	50	55
150.3	140.2	21	37	51	54
171.2	161.1	29	30	31	43
192.4	181.8	13	22	35	35
213.2	202.7	12	16	29	14
234.1	223.5	18	22	10	21
255.0	244.7	14	14	16	11
275.8	267.9	18	16	15	14
297.0	286.4	6	11	7	21
317.9	307.1	5	9	6	6
338.6	328.0	8	4	7	3
359.4	349.3	4	8	5	1
380.3	370.0	3	4	3	
401.5	390.9	1	3	2	
422.3	411.8	1			
443.2	432.6	0			
464.4	453.8	2			
484.8	474.6	0			
505.5	495.4	0			
527.0	516.2	1			
547.7	537.1				
$\frac{\Sigma ND^3}{\Sigma ND^2}$		262	246	227	210

SLURRY 45% NOZZLE SF

$\Delta P\ (kNm^{-2})$		483	690	896	1103
ΔD	D_M	N	N	N	N
66.7	56.5	0	0	1	3
87.9	77.3	14	21	32	36
108.8	98.2	30	55	48	55
129.5	118.9	36	67	44	58
150.3	140.2	34	46	59	47
171.2	161.1	24	38	61	50
192.4	181.8	32	46	56	37
213.2	202.7	19	37	49	30
234.1	223.5	9	28	24	19
255.0	244.7	17	37	30	17
275.8	267.9	15	24	26	18
297.0	286.4	11	16	14	10
317.9	307.1	11	16	18	13
338.6	328.0	11	6	12	4
359.4	349.3	6	9	9	3
380.3	370.0	4	2	1	4
401.5	390.9	3	4	2	
422.3	411.8	5	1	1	
443.2	432.6	1	2	1	
464.4	453.8	4			
484.8	474.6	1			
505.5	495.4	0			
527.0	516.2	1			
547.7	537.1	1			
$\frac{\Sigma ND^3}{\Sigma ND^2}$		291	245	239	222

SLURRY 50% NOZZLE SF

ΔP (kNm^{-2})		483	690	896	1103
ΔD	D_m	N	N	N	N
43.5	36.8	3	4	13	2
57.3	50.4	14	7	27	9
70.9	64.0	25	26	49	20
84.4	77.5	31	31	62	20
98.0	91.4	47	30	45	23
111.6	105.0	38	28	44	25
125.4	118.5	28	24	43	20
139.0	132.1	33	25	43	11
152.6	145.7	33	14	36	14
166.2	159.5	22	31	35	17
179.8	174.6	23	15	41	19
193.6	186.7	22	19	26	12
207.2	200.2	26	18	24	18
220.7	213.8	20	9	27	16
234.3	227.7	17	20	27	12
247.9	241.2	19	11	21	10
261.7	254.8	20	11	27	11
275.3	268.4	21	6	16	8
288.9	282.0	11	7	10	7
302.7	295.8	10	9	11	7
316.0	309.4	12	3	9	8
329.5	322.9	15	6	10	5
343.5	336.5	12	1	3	3
357.0	350.1	9	5	5	3
370.6	364.0	6	5	4	1
384.2	377.5	5	2	2	4
398.0	391.1	5	1	0	1
411.6	404.7	4	1	1	4
425.2	418.3	5	1	0	5
439.0	432.1	3	2	1	3
452.3	445.7	2		0	1
466.2	459.3	2		1	1
479.8	472.8	1		0	1
493.3	486.4	2		1	
506.9	500.2	3			
$\frac{\Sigma ND^3}{\Sigma ND^2}$		291	250	236	225

Appendix II

Derivation of Equation 4.23

Evaluation of Equation 4.12

Equation 4.12 is

$$\{v_r.v_\theta\} + 2\int \frac{v_r v_\theta}{r}\,dr + \int \frac{\partial}{\partial z}\,(v_\theta.v_z)\,dr = \nu\left(\{\frac{\partial v_\theta}{\partial r}\} + \{\frac{v_\theta}{r}\}\right)$$

in terms of n 4.12 becomes

$$\{v_r.v_\theta\}_o^1 + 2\int_o^1 \frac{v_r v_\theta(-\delta\ d_n)}{R-n\delta} + \int_o^1 \frac{\partial}{\partial z}\,(v_\theta.v_z)(-\delta\ d_n)$$

$$= \nu\left(\{\frac{d_{v\theta}}{dn}\cdot\frac{d_n}{d_r}\}_o^1 + \{\frac{v_\theta}{R-n\delta}\}_o^1\right) \qquad -(4.1.1)$$

Dealing with the first term only

substitute in vr from equation 4.22 and v_θ from 4.15,

$\{v_r v_\theta\}_o^1$ becomes:

$$\left[\left(\frac{\Omega}{R}\,(2n-n^2)\,\frac{\delta}{R-n\delta}\right)\left(\frac{W}{\delta}\,\frac{dR}{dz}\left(2Rn-n^2(R+\delta)+\frac{2n^3\delta}{3}\right)\right.\right.$$

$$\left.\left. - \frac{W}{\delta}\,\frac{d\delta}{dz}\left(Rn^2-\frac{2n^3}{3}\,(R+\delta)+\frac{n^4\delta}{2}\right)+\frac{dw}{dz}\left(Rn^2-\frac{n^3}{3}\,(R+2\delta)+\frac{n^4\delta}{4}\right)\right]_{n=o}^{n=1}$$

$$-(4.1.2)$$

Evaluating (4.1.2) and simplifying:

$$\frac{dR}{dz}\left(\frac{W(R-\delta/3)}{R(R-\delta)}\right)+\frac{d\delta}{dz}\left(\frac{-W(R/3-\delta/6)}{R(R-\delta)}\right)+\frac{dw}{dz}\left(\frac{\delta(2R/3-5\delta/12)}{R(R-\delta)}\right)$$

$$-(4.1.3)$$

The second term becomes upon substitution of 4.95 and 4.22

$$\frac{-2\delta^2}{R} \int_o^1 \frac{2n-n^2}{(R-n\delta)^2} \left[\frac{W}{\delta} \frac{dR}{dz} \left(2Rn-n^2(R+\delta)+\frac{2n^3\delta}{3} \right) \right.$$

$$\left. - \frac{W}{\delta} \frac{d\delta}{dz} \left(Rn^2-\frac{2n^3}{3}(R+\delta)+\frac{n^4\delta}{2} \right) + \frac{dw}{dz} \left(Rn^2-\frac{n^3}{3}(R+2\delta) + \frac{n^4\delta}{4} \right) \right] dn$$

- (4.1.4)

Inspection of (4.1.4) reveals that a log term will appear upon integration. If this log term is itself expanded in series form, the integral of (4.1.4) becomes:

$$-\frac{dR}{dz} \left(\frac{16W\delta}{15R(R-\delta)} \right) + \frac{d\delta}{dz} \left(\frac{13W\delta}{45R(R-\delta)} \right) - \frac{dw}{dz} \left(\frac{4\delta^2}{9R(R-\delta)} \right) - \quad (4.1.5)$$

The third term of 4.1.1 is

$$-\delta \int_o^1 \frac{\partial}{\partial z} (v_\theta v_z)\, dn \qquad - (4.1.6)$$

From 4.15, 4.19, and 4.20 $\frac{\partial}{\partial z} (v_\theta . v_z)$ becomes

$$\frac{\Omega}{R} (2n-n^2) \left[W(2-2n) \left(\frac{1}{\delta} \frac{dR}{dz} - \frac{n}{\delta} \frac{d\delta}{dz} \right) + \frac{dw}{dz} (2n-n^2) \right]$$

$$+ W(2n-n^2) \frac{\Omega}{R^2} \left[2R(1-n) \left(\frac{1}{\delta} \frac{dR}{dz} - \frac{n}{\delta} \frac{d\delta}{dz} \right) - (2n-n^2) \frac{dR}{dz} \right]$$

- (4.1.7)

Evaluating (4.1.6):

$$\frac{dR}{dz} \left(\frac{8W\delta}{15R^2} - \frac{W}{R} \right) + \frac{d\delta}{dz} \left(\frac{7W}{15R} \right) + \frac{dw}{dz} \left(\frac{-8\delta}{15R} \right) \quad - (4.1.8)$$

The term on the R.H.S. of 4.1.1 upon evaluation becomes:

$$\nu\left(\frac{2R-\delta}{R\delta(R-\delta)}\right) \qquad - (4.1.9)$$

collecting the coefficients of $\frac{dR}{dz}$, $\frac{d\delta}{dz}$ and $\frac{dw}{dz}$ together the L.H.S. of 4.1.1. becomes:

$$\frac{d\delta}{dz}\left[\frac{2W(R-\delta/12)}{15R(R-\delta)}\right] + \frac{dR}{dz}\left[\frac{2w\delta}{15R(R-\delta)}\right] + \frac{dw}{dz}\left[\frac{2\delta}{15}\right] - (4.1.10)$$

Combining with (4.1.9)

$$\frac{d\delta}{dz} = \frac{15R(R-\delta)}{2W(R-\delta/12)}\left[\nu\left(\frac{2R-\delta}{R\delta(R-\delta)}\right) - \frac{dR}{dz}\left[\frac{2w\delta}{15R(R-\delta)}\right] - \frac{dw}{dz}\left(\frac{2\delta}{15}\right)\right]$$

$$\text{or} \quad \frac{d\delta}{dz} = \frac{1}{R-\delta/12}\left[\frac{15\nu}{w}\left(\frac{R}{\delta} - \frac{1}{2}\right) - \frac{\delta dR}{dz} - \frac{\delta R}{w}\frac{dw}{dz}\right] - (4.1.11)$$

which is the same as (4.23).